Why do we need Sirius? (Scientific examples)

Tuesday 23 Nov 2010 at 11:00 (01h00')

Primary authors : Prof. PETROFF, Yves (LNLS)

Co-authors :

Presenter : Prof. PETROFF, Yves (LNLS)

WHY DO WE NEED SIRIUS?

Yves Petroff
yves.petroff@gmail.com
LNLS-CAMPINAS-BRAZIL

WHY DO WE NEED SIRIUS?

Yves Petroff
yves.petroff@gmail.com
LNLS-CAMPINAS-BRAZIL

1. Introduction

WHY DO WE NEED SIRIUS?

Yves Petroff
yves.petroff@gmail.com
LNLS-CAMPINAS-BRAZIL

1. Introduction

For me the the most important achievements at 3rd generation sources, ouside of str.bio, have been 3 D imaging, inelastic scattering at meV resolution, HP science and in the soft X-Ray, ARPES+RIXS. A facility is not judged on the emittance or the number of undulators but on the scientific production.

WHY DO WE NEED SIRIUS?

Yves Petroff
yves.petroff@gmail.com
LNLS-CAMPINAS-BRAZIL

1. Introduction
   For me the the most important achievements at 3rd generation sources, ouside of str.bio, have been 3 D imaging, inelastic scattering at meV resolution, HP science and in the soft X-Ray, ARPES+RIXS. A facility is not judged on the emittance or the number of undulators but on the scientific production.
2. Exploitation of the phase contrast: 3D Imaging at µm level

WHY DO WE NEED SIRIUS?

Yves Petroff
yves.petroff@gmail.com
LNLS-CAMPINAS-BRAZIL

1. Introduction
   For me the the most important achievements at 3rd generation sources, ouside of str.bio, have been 3 D imaging, inelastic scattering at meV resolution, HP science and in the soft X-Ray, ARPES+RIXS. A facility is not judged on the emittance or the number of undulators but on the scientific production.
2. Exploitation of the phase contrast: 3D Imaging at µm level
3. Exploitation of the coherence: 3D Imaging at the nm level

WHY DO WE NEED SIRIUS?

Yves Petroff
yves.petroff@gmail.com
LNLS-CAMPINAS-BRAZIL

1. Introduction
   For me the the most important achievements at 3rd generation sources, ouside of str.bio, have been 3 D imaging, inelastic scattering at meV resolution, HP science and in the soft X-Ray, ARPES+RIXS. A facility is not judged on the emittance or the number of undulators but on the scientific production.
2. Exploitation of the phase contrast: 3D Imaging at µm level
3. Exploitation of the coherence: 3D Imaging at the nm level
4. fs magnetism

WHY DO WE NEED SIRIUS?

Yves Petroff
yves.petroff@gmail.com
LNLS-CAMPINAS-BRAZIL

1. Introduction
   For me the the most important achievements at 3rd generation sources, ouside of str.bio, have been 3 D imaging, inelastic scattering at meV resolution, HP science and in the soft X-Ray, ARPES+RIXS. A facility is not judged on the emittance or the number of undulators but on the scientific production.
2. Exploitation of the phase contrast: 3D Imaging at µm level
3. Exploitation of the coherence: 3D Imaging at the nm level
4. fs magnetism
5. IR:gap of graphene

WHY DO WE NEED SIRIUS?

Yves Petroff
yves.petroff@gmail.com
LNLS-CAMPINAS-BRAZIL

1. Introduction
   For me the the most important achievements at 3rd generation sources, ouside of str.bio, have been 3 D imaging, inelastic scattering at meV resolution, HP science and in the soft X-Ray, ARPES+RIXS. A facility is not judged on the emittance or the number of undulators but on the scientific production.
2. Exploitation of the phase contrast: 3D Imaging at µm level
3. Exploitation of the coherence: 3D Imaging at the nm level
4. fs magnetism
5. IR:gap of graphene
6. X-Ray under extremes conditions of pressure and temperature (377 GPa and 5700 K)

WHY DO WE NEED SIRIUS?

Yves Petroff
yves.petroff@gmail.com
LNLS-CAMPINAS-BRAZIL

1. Introduction
   For me the the most important achievements at 3rd generation sources, ouside of str.bio, have been 3 D imaging, inelastic scattering at meV resolution, HP science and in the soft X-Ray, ARPES+RIXS. A facility is not judged on the emittance or the number of undulators but on the scientific production.
2. Exploitation of the phase contrast: 3D Imaging at µm level
3. Exploitation of the coherence: 3D Imaging at the nm level
4. fs magnetism
5. IR:gap of graphene
6. X-Ray under extremes conditions of pressure and temperature (377 GPa and 5700 K)
7. Melting

WHY DO WE NEED SIRIUS?

Yves Petroff
yves.petroff@gmail.com
LNLS-CAMPINAS-BRAZIL

1. Introduction
   For me the the most important achievements at 3rd generation sources, ouside of str.bio, have been 3 D imaging, inelastic scattering at meV resolution, HP science and in the soft X-Ray, ARPES+RIXS. A facility is not judged on the emittance or the number of undulators but on the scientific production.
2. Exploitation of the phase contrast: 3D Imaging at µm level
3. Exploitation of the coherence: 3D Imaging at the nm level
4. fs magnetism
5. IR:gap of graphene
6. X-Ray under extremes conditions of pressure and temperature (377 GPa and 5700 K)
7. Melting
8. Conclusions

WHY DO WE NEED SIRIUS?

Yves Petroff
yves.petroff@gmail.com
LNLS-CAMPINAS-BRAZIL

1. Introduction
   For me the the most important achievements at 3rd generation sources, ouside of str.bio, have been 3 D imaging, inelastic scattering at meV resolution, HP science and in the soft X-Ray, ARPES+RIXS. A facility is not judged on the emittance or the number of undulators but on the scientific production.
2. Exploitation of the phase contrast: 3D Imaging at µm level
3. Exploitation of the coherence: 3D Imaging at the nm level
4. fs magnetism
5. IR:gap of graphene
6. X-Ray under extremes conditions of pressure and temperature (377 GPa and 5700 K)
7. Melting
8. Conclusions

WHY DO WE NEED SIRIUS?

Yves Petroff
yves.petroff@gmail.com
LNLS-CAMPINAS-BRAZIL

1. Introduction
   For me the the most important achievements at 3rd generation sources, ouside of str.bio, have been 3 D imaging, inelastic scattering at meV resolution, HP science and in the soft X-Ray, ARPES+RIXS. A facility is not judged on the emittance or the number of undulators but on the scientific production.
2. Exploitation of the phase contrast: 3D Imaging at µm level
3. Exploitation of the coherence: 3D Imaging at the nm level
4. fs magnetism
5. IR:gap of graphene
6. X-Ray under extremes conditions of pressure and temperature (377 GPa and 5700 K)
7. Melting
8. Conclusions

WHY DO WE NEED SIRIUS?

Yves Petroff
yves.petroff@gmail.com
LNLS-CAMPINAS-BRAZIL

1. Introduction
   For me the the most important achievements at 3rd generation sources, ouside of str.bio, have been 3 D imaging, inelastic scattering at meV resolution, HP science and in the soft X-Ray, ARPES+RIXS. A facility is not judged on the emittance or the number of undulators but on the scientific production.
2. Exploitation of the phase contrast: 3D Imaging at µm level
3. Exploitation of the coherence: 3D Imaging at the nm level
4. fs magnetism
5. IR:gap of graphene
6. X-Ray under extremes conditions of pressure and temperature (377 GPa and 5700 K)
7. Melting
8. Conclusions

Production of synchrotron radiation

2 Generation

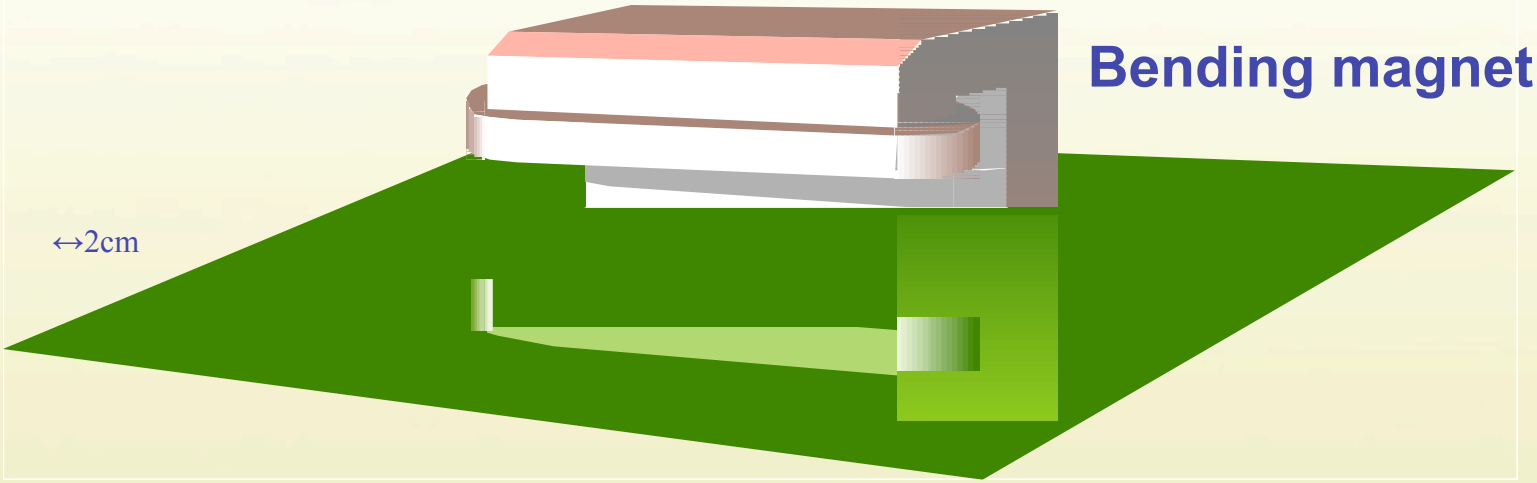

Production of synchrotron radiation

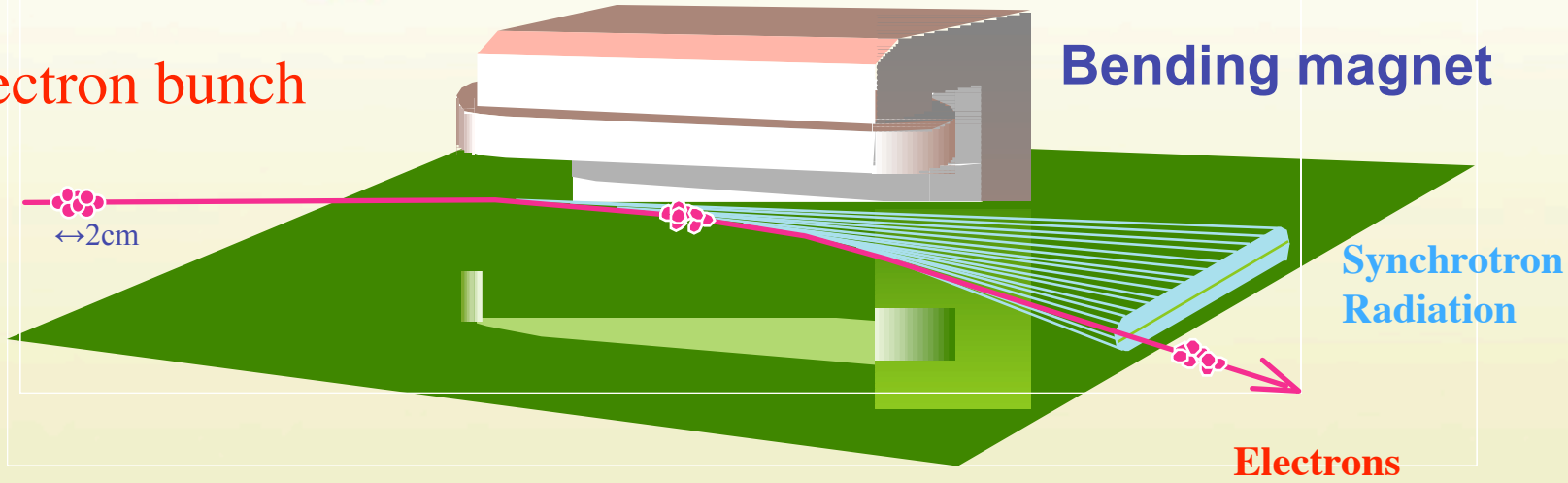

Production of synchrotron radiation

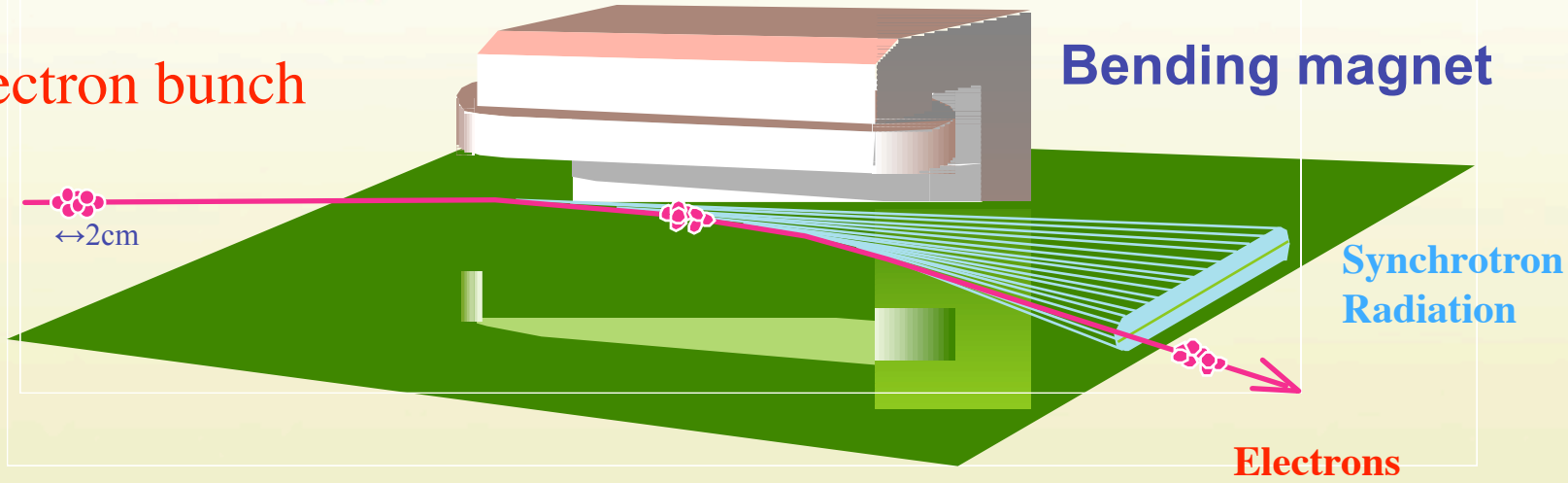

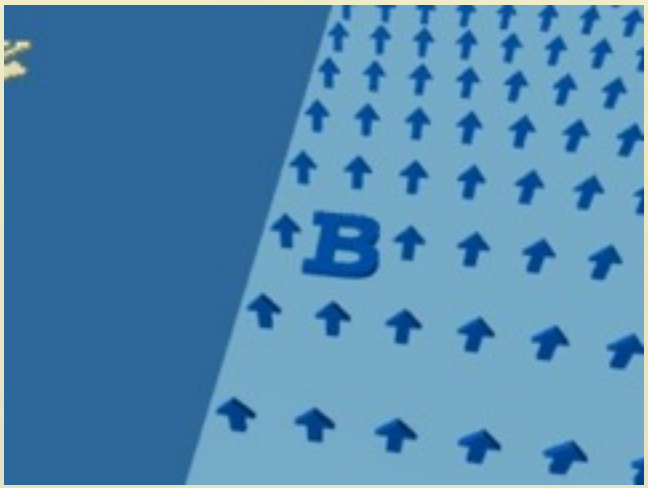

2 Generation

Production of synchrotron radiation

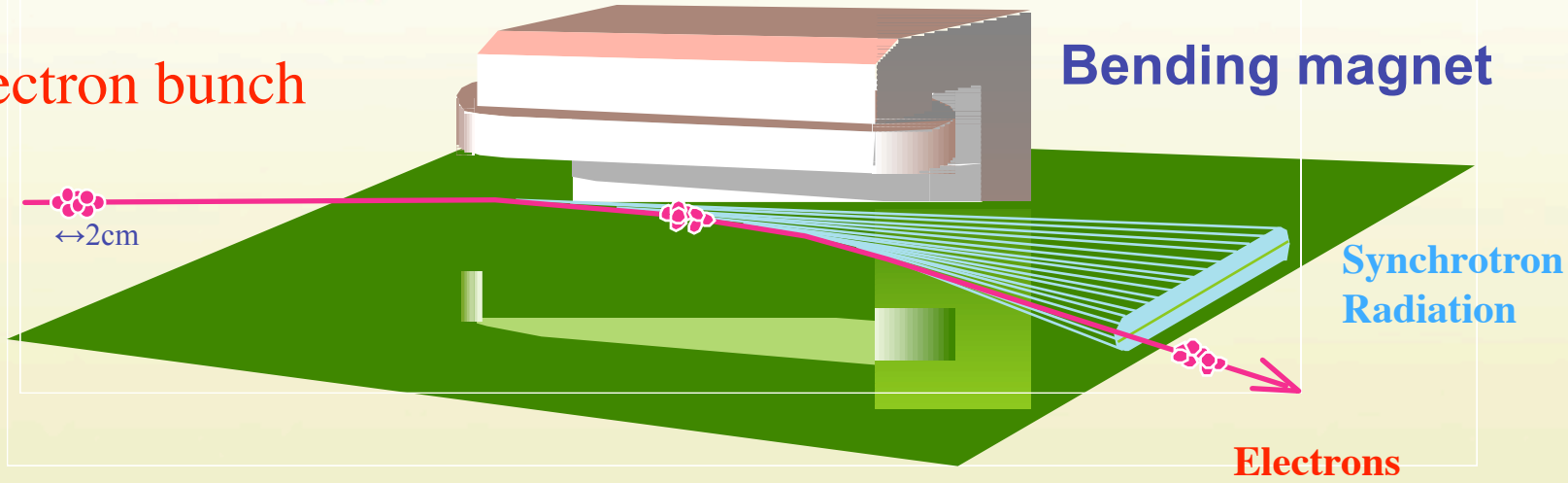

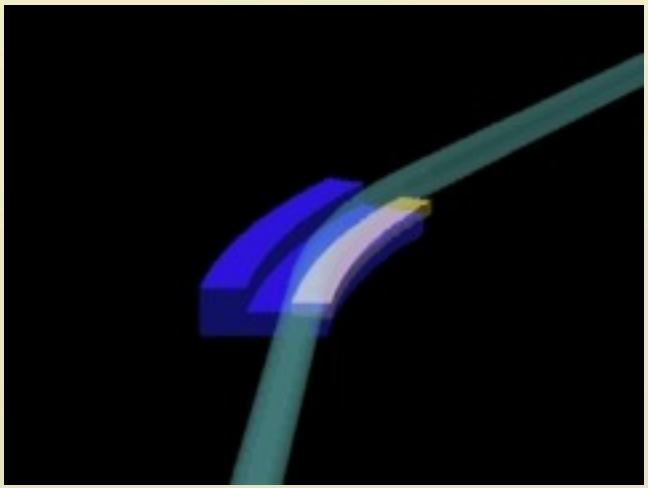

2 Generation

Production of synchrotron radiation

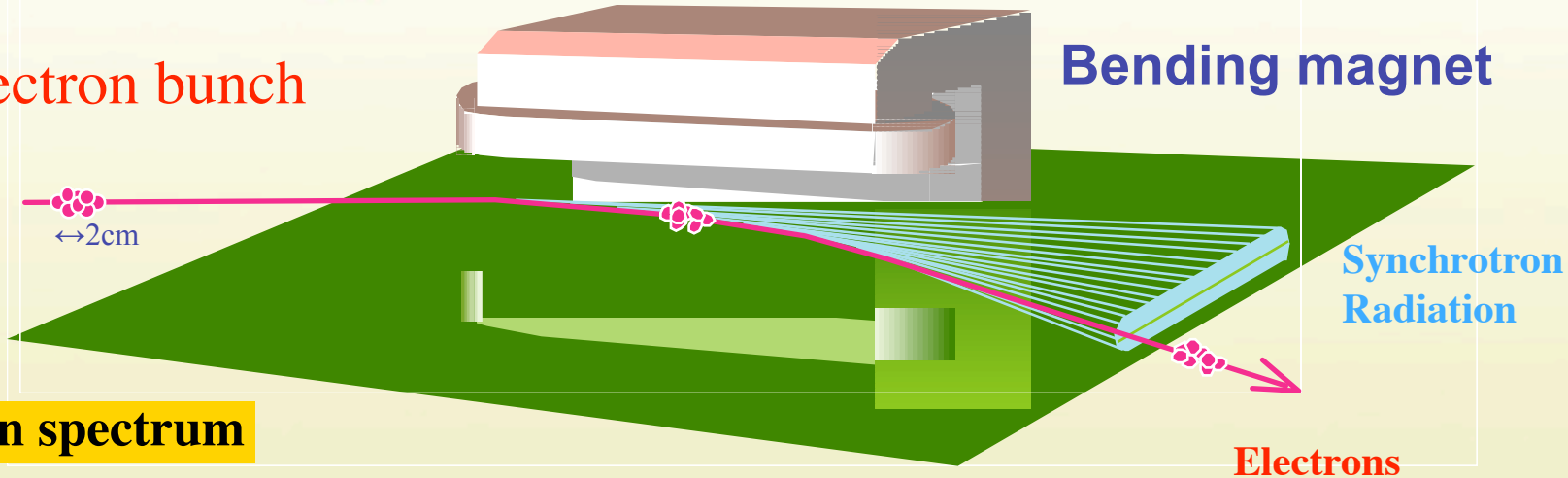

Emission spectrum

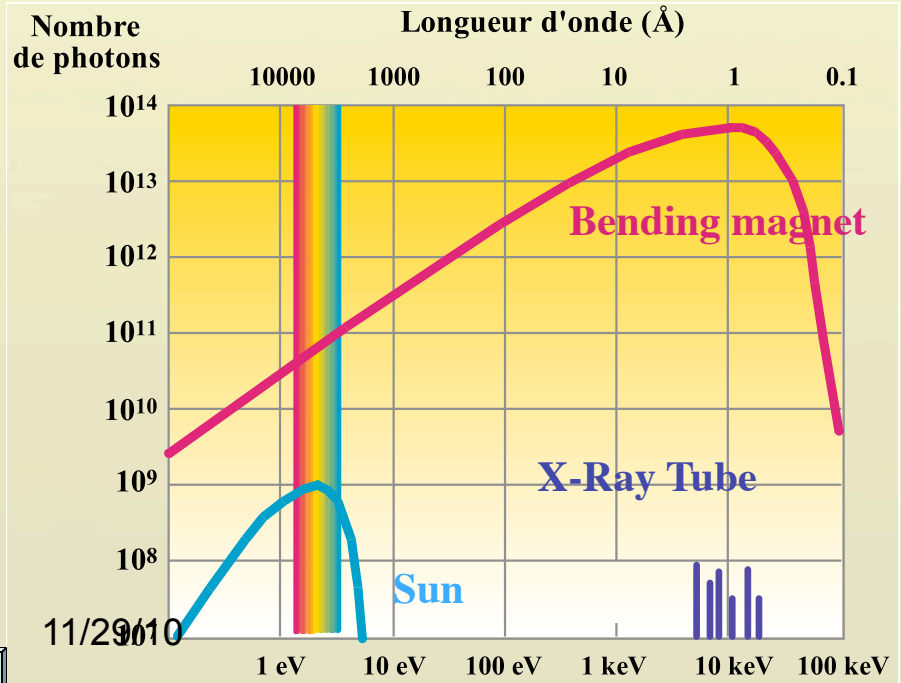

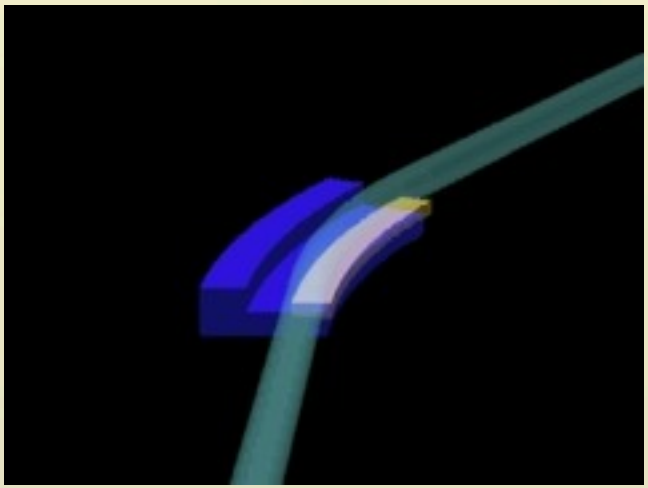

3 th Generation

Insertion devices

← NOTICE THE VERY SMALL DIVERGENCE OF THE BEAM

3 th Generation

Insertion devices

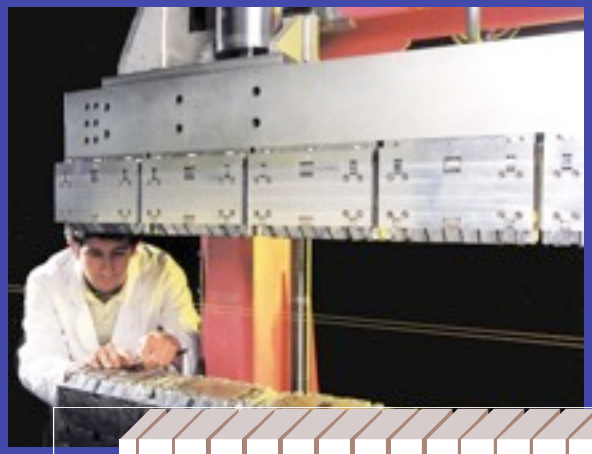

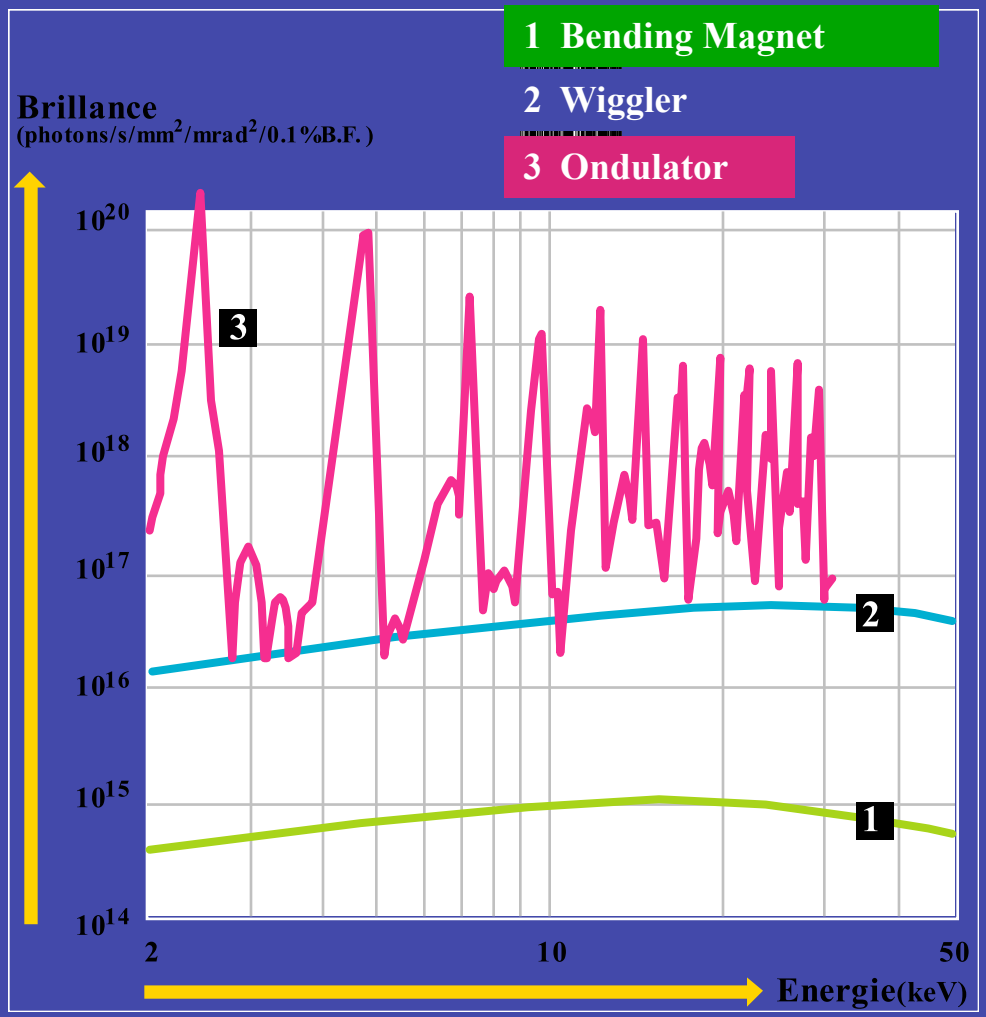

← NOTICE THE VERY SMALL DIVERGENCE OF THE BEAM

COHERENCE

- Light is coherent if it has:
  - Spatial (transverse)coherence→ divergence
  - Temporal (longitudinal) coherence→ monochromaticity

- The light emitted by an undulator has spatial coherence, temporal coherence can be added by a monochromator

- Coherence length:
  - longitudinal: $L^{long} = ½ \lambda^2/\Delta\lambda$
  - transverse: $L^{tra} = \lambda R/(2\pi\sigma)$

  (λ = wavelength, σ= beam size and R = distance source-sample)

  Ex: L^{tra} =25/100 μm in the vertical plane, 3/10 in the horizontal

SYNCHROTRON RADIATION IN THE WORLD

SYNCHROTRON RADIATION IN THE WORLD

SYNCHROTRON RADIATION IN THE WORLD

- Scientific research and technological development with synchrotron radiation have experienced an enormous growth all around the world over the past 20 years. In fact, there are today more than 50 operating synchrotron light sources all around the globe. Sixteen of them are 3th generation sources, characterized by low emmittance (small size and very small divergence of the beam) and the intensive use of magnetic insertion devices called undulators: they have been put in operation after 1994 and have allowed to gain 4 orders of magnitude in brightness. Some of the sources have come into operation quite recently, such as the British (Diamond), the French (SOLEIL), the Australian (BOOMERANG), the Canadian Light Source, the Chinese SSRF, the German (PETRA III) facilities and the Spanish one, ALBA, will come in operation next year.

- All of those laboratories represent the response of these various countries to the explosive growth in demand for synchrotron radiation, as a result of the wide range of scientific and technological applications which were made possible by the availability of these new sources.
It is interesting to notice that the number of users of the DOE facilities in the USA (APS, ALS, NSLS, SSRL) has increased by 4O% (6000→ 8400) between 2000 and 2008 while the number of users of the European Facility (ESRF) has increased by 46% during the period 2002/2009.

SYNCHROTRON RADIATION IN THE WORLD

- Scientific research and technological development with synchrotron radiation have experienced an enormous growth all around the world over the past 20 years. In fact, there are today more than 50 operating synchrotron light sources all around the globe. Sixteen of them are 3th generation sources, characterized by low emmittance (small size and very small divergence of the beam) and the intensive use of magnetic insertion devices called undulators: they have been put in operation after 1994 and have allowed to gain 4 orders of magnitude in brightness. Some of the sources have come into operation quite recently, such as the British (Diamond), the French (SOLEIL), the Australian (BOOMERANG), the Canadian Light Source, the Chinese SSRF, the German (PETRA III) facilities and the Spanish one, ALBA, will come in operation next year.

- All of those laboratories represent the response of these various countries to the explosive growth in demand for synchrotron radiation, as a result of the wide range of scientific and technological applications which were made possible by the availability of these new sources.
It is interesting to notice that the number of users of the DOE facilities in the USA (APS, ALS, NSLS, SSRL) has increased by 4O% (6000→ 8400) between 2000 and 2008 while the number of users of the European Facility (ESRF) has increased by 46% during the period 2002/2009.

SYNCHROTRON RADIATION IN THE WORLD

- Scientific research and technological development with synchrotron radiation have experienced an enormous growth all around the world over the past 20 years. In fact, there are today more than 50 operating synchrotron light sources all around the globe. Sixteen of them are 3th generation sources, characterized by low emmittance (small size and very small divergence of the beam) and the intensive use of magnetic insertion devices called undulators: they have been put in operation after 1994 and have allowed to gain 4 orders of magnitude in brightness. Some of the sources have come into operation quite recently, such as the British (Diamond), the French (SOLEIL), the Australian (BOOMERANG), the Canadian Light Source, the Chinese SSRF, the German (PETRA III) facilities and the Spanish one, ALBA, will come in operation next year.

- All of those laboratories represent the response of these various countries to the explosive growth in demand for synchrotron radiation, as a result of the wide range of scientific and technological applications which were made possible by the availability of these new sources.
It is interesting to notice that the number of users of the DOE facilities in the USA (APS, ALS, NSLS, SSRL) has increased by 4O% (6000→ 8400) between 2000 and 2008 while the number of users of the European Facility (ESRF) has increased by 46% during the period 2002/2009.

- **Why that?**

SYNCHROTRON RADIATION IN THE WORLD

- Scientific research and technological development with synchrotron radiation have experienced an enormous growth all around the world over the past 20 years. In fact, there are today more than 50 operating synchrotron light sources all around the globe. Sixteen of them are 3th generation sources, characterized by low emmittance (small size and very small divergence of the beam) and the intensive use of magnetic insertion devices called undulators: they have been put in operation after 1994 and have allowed to gain 4 orders of magnitude in brightness. Some of the sources have come into operation quite recently, such as the British (Diamond), the French (SOLEIL), the Australian (BOOMERANG), the Canadian Light Source, the Chinese SSRF, the German (PETRA III) facilities and the Spanish one, ALBA, will come in operation next year.

- All of those laboratories represent the response of these various countries to the explosive growth in demand for synchrotron radiation, as a result of the wide range of scientific and technological applications which were made possible by the availability of these new sources.
It is interesting to notice that the number of users of the DOE facilities in the USA (APS, ALS, NSLS, SSRL) has increased by 4O% (6000→ 8400) between 2000 and 2008 while the number of users of the European Facility (ESRF) has increased by 46% during the period 2002/2009.

- **Why that?**

  - the very important development of structural biology everywhere in the world: 127 beamlines are used exclusively for structural biology. All the pharmaceutical companies are using those beamlines.

SYNCHROTRON RADIATION IN THE WORLD

- Scientific research and technological development with synchrotron radiation have experienced an enormous growth all around the world over the past 20 years. In fact, there are today more than 50 operating synchrotron light sources all around the globe. Sixteen of them are 3th generation sources, characterized by low emmittance (small size and very small divergence of the beam) and the intensive use of magnetic insertion devices called undulators: they have been put in operation after 1994 and have allowed to gain 4 orders of magnitude in brightness. Some of the sources have come into operation quite recently, such as the British (Diamond), the French (SOLEIL), the Australian (BOOMERANG), the Canadian Light Source, the Chinese SSRF, the German (PETRA III) facilities and the Spanish one, ALBA, will come in operation next year.

- All of those laboratories represent the response of these various countries to the explosive growth in demand for synchrotron radiation, as a result of the wide range of scientific and technological applications which were made possible by the availability of these new sources.
It is interesting to notice that the number of users of the DOE facilities in the USA (APS, ALS, NSLS, SSRL) has increased by 4O% (6000→ 8400) between 2000 and 2008 while the number of users of the European Facility (ESRF) has increased by 46% during the period 2002/2009.

- **Why that?**

  - the very important development of structural biology everywhere in the world: 127 beamlines are used exclusively for structural biology. All the pharmaceutical companies are using those beamlines.

SYNCHROTRON RADIATION IN THE WORLD

- Scientific research and technological development with synchrotron radiation have experienced an enormous growth all around the world over the past 20 years. In fact, there are today more than 50 operating synchrotron light sources all around the globe. Sixteen of them are 3th generation sources, characterized by low emmittance (small size and very small divergence of the beam) and the intensive use of magnetic insertion devices called undulators: they have been put in operation after 1994 and have allowed to gain 4 orders of magnitude in brightness. Some of the sources have come into operation quite recently, such as the British (Diamond), the French (SOLEIL), the Australian (BOOMERANG), the Canadian Light Source, the Chinese SSRF, the German (PETRA III) facilities and the Spanish one, ALBA, will come in operation next year.

- All of those laboratories represent the response of these various countries to the explosive growth in demand for synchrotron radiation, as a result of the wide range of scientific and technological applications which were made possible by the availability of these new sources.
It is interesting to notice that the number of users of the DOE facilities in the USA (APS, ALS, NSLS, SSRL) has increased by 4O% (6000→ 8400) between 2000 and 2008 while the number of users of the European Facility (ESRF) has increased by 46% during the period 2002/2009.

- **Why that?**

- the very important development of structural biology everywhere in the world: 127 beamlines are used exclusively for structural biology. All the pharmaceutical companies are using those beamlines.

- the exploitation of specific properties of the X-Ray beams of these new facilities (phase contrast and coherence) allowing to obtain three-dimensional images of any object with submicron resolution. This has brought to synchrotrons new communities: paleontology, cultural heritage, geophysics environment…

2- EXPLOITATION OF THE PHASE CONTRAST IN X-RAY IMAGING

■The behaviour of x-rays as they travel through an object can be described in terms of a complex index of refraction. In the x-ray region, it can be written as:

$$n = 1 - \delta - i\beta$$

2- EXPLOITATION OF THE PHASE CONTRAST IN X-RAY IMAGING

■The behaviour of x-rays as they travel through an object can be described in terms of a complex index of refraction. In the x-ray region, it can be written as:

$$n = 1 - \delta - i\beta$$

where the real part δ corresponds to the phase shift due to refraction and the imaginary part β to the absorption.

2- EXPLOITATION OF THE PHASE CONTRAST IN X-RAY IMAGING

■The behaviour of x-rays as they travel through an object can be described in terms of a complex index of refraction. In the x-ray region, it can be written as:

$$n = 1 - \delta - i\beta$$

where the real part δ corresponds to the phase shift due to refraction and the imaginary part β to the absorption.

■ The real and imaginary parts have very different dependences on the photon energy; in the regime where the photoelectric effect dominates and far from absorption edges, $\beta \sim E^{-4}$ while $\delta \sim E^{-2}$. As a consequence, the values of δ can be orders of magnitude larger than β terms; for example, the values for nylon (C_2H_4) at 25 keV are $\delta = 3.50 \times 10^{-7}$ and $\beta = 8.12 \times 10^{-11}$.

2- EXPLOITATION OF THE PHASE CONTRAST IN X-RAY IMAGING

■The behaviour of x-rays as they travel through an object can be described in terms of a complex index of refraction. In the x-ray region, it can be written as:

$$n = 1 - \delta - i\beta$$

where the real part δ corresponds to the phase shift due to refraction and the imaginary part β to the absorption.

■ The real and imaginary parts have very different dependences on the photon energy; in the regime where the photoelectric effect dominates and far from absorption edges, $\beta \sim E^{-4}$ while $\delta \sim E^{-2}$. As a consequence, the values of δ can be orders of magnitude larger than β terms; for example, the values for nylon (C_2H_4) at 25 keV are $\delta = 3.50 \times 10^{-7}$ and $\beta = 8.12 \times 10^{-11}$.

■ X-rays passing through regions of different δ values are subjected to phase shifts that correspond to being refracted. These changes, which can originate from the purely geometrical effect of the shape of the object or, for instance, from local homogeneity defects of the object, cannot often be visualized using absorption imaging techniques.

■ Different techniques have been developed for detecting the phase variations:
- in-line holography (holotomography)
- interferometry
- diffractometry

2- EXPLOITATION OF THE PHASE CONTRAST IN X-RAY IMAGING

■The behaviour of x-rays as they travel through an object can be described in terms of a complex index of refraction. In the x-ray region, it can be written as:

$$n = 1 - \delta - i\beta$$

where the real part δ corresponds to the phase shift due to refraction and the imaginary part β to the absorption.

■ The real and imaginary parts have very different dependences on the photon energy; in the regime where the photoelectric effect dominates and far from absorption edges, $\beta \sim E^{-4}$ while $\delta \sim E^{-2}$. As a consequence, the values of δ can be orders of magnitude larger than β terms; for example, the values for nylon (C_2H_4) at 25 keV are $\delta = 3.50 \times 10^{-7}$ and $\beta = 8.12 \times 10^{-11}$.

■ X-rays passing through regions of different δ values are subjected to phase shifts that correspond to being refracted. These changes, which can originate from the purely geometrical effect of the shape of the object or, for instance, from local homogeneity defects of the object, cannot often be visualized using absorption imaging techniques.

■ Different techniques have been developed for detecting the phase variations:
- in-line holography (holotomography)
- interferometry
- diffractometry
- SAXS (small angle scattering)

II.(A) PHASE PROPAGATION CONTRAST

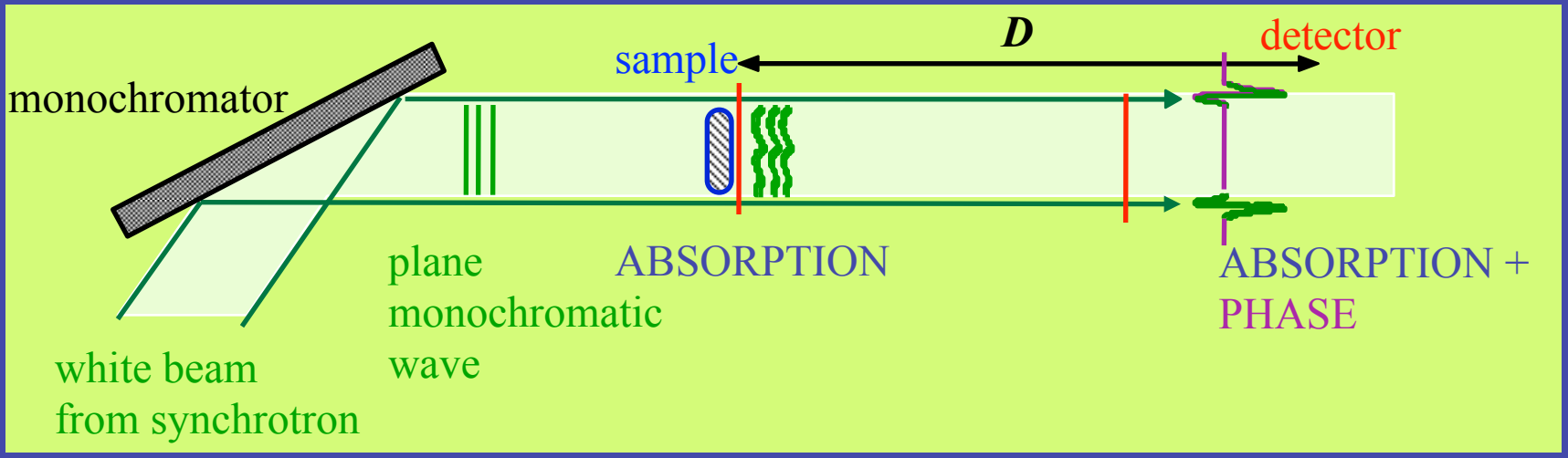

II.(A) PHASE PROPAGATION CONTRAST

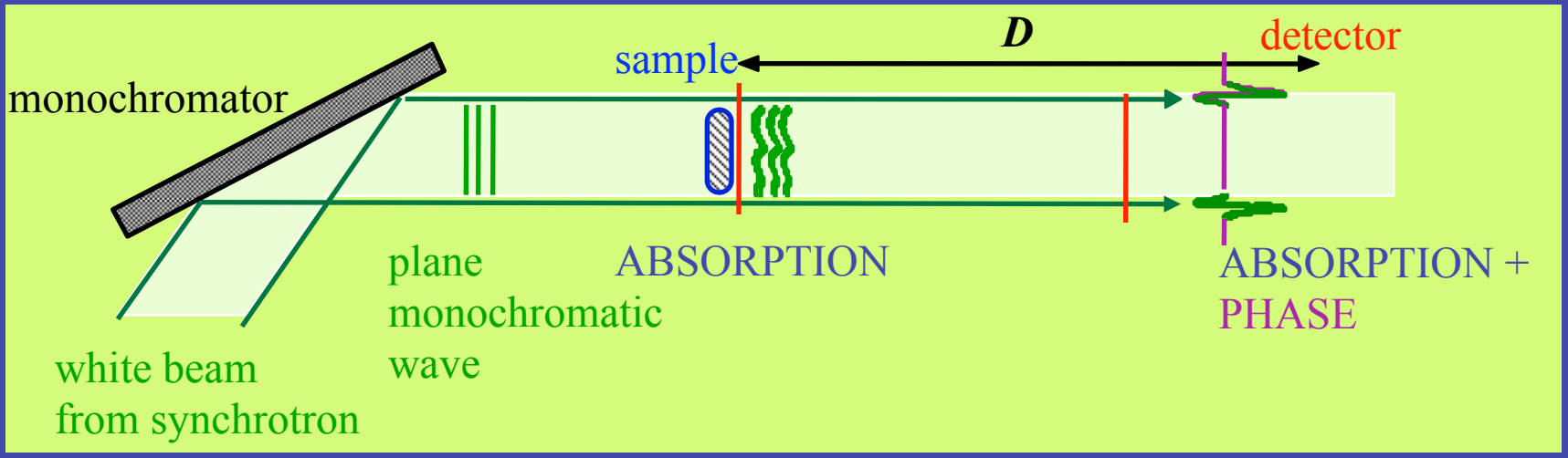

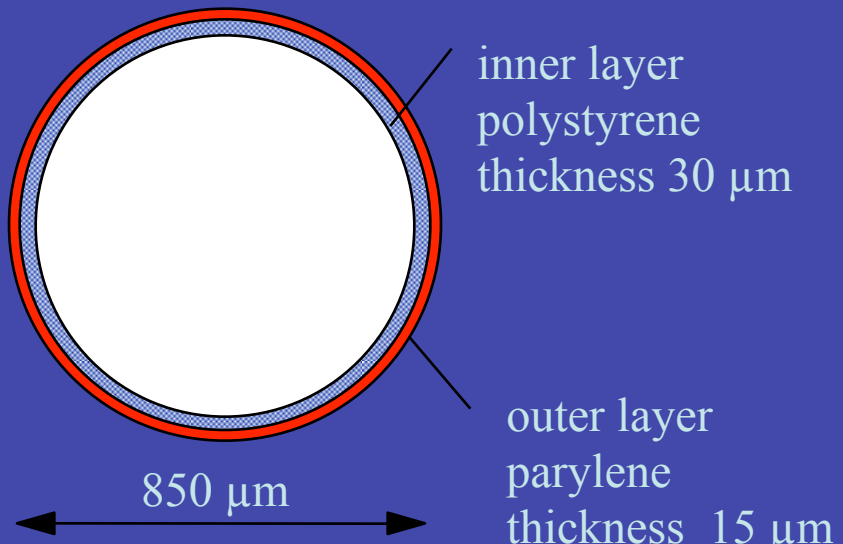

II.(A) PHASE PROPAGATION CONTRAST

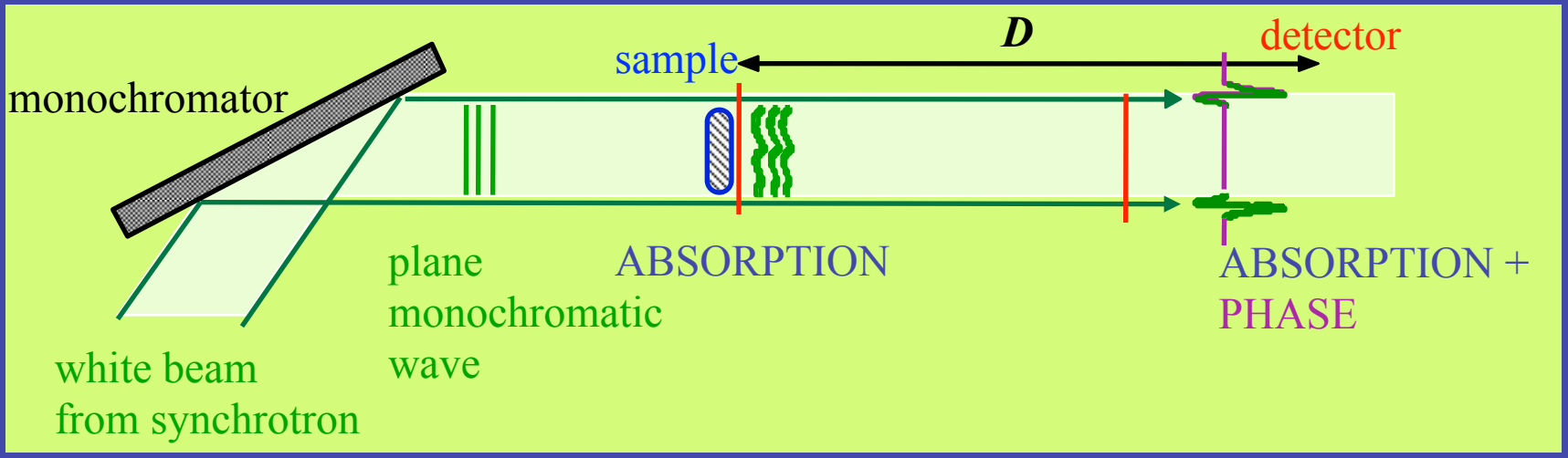

II.(A) PHASE PROPAGATION CONTRAST

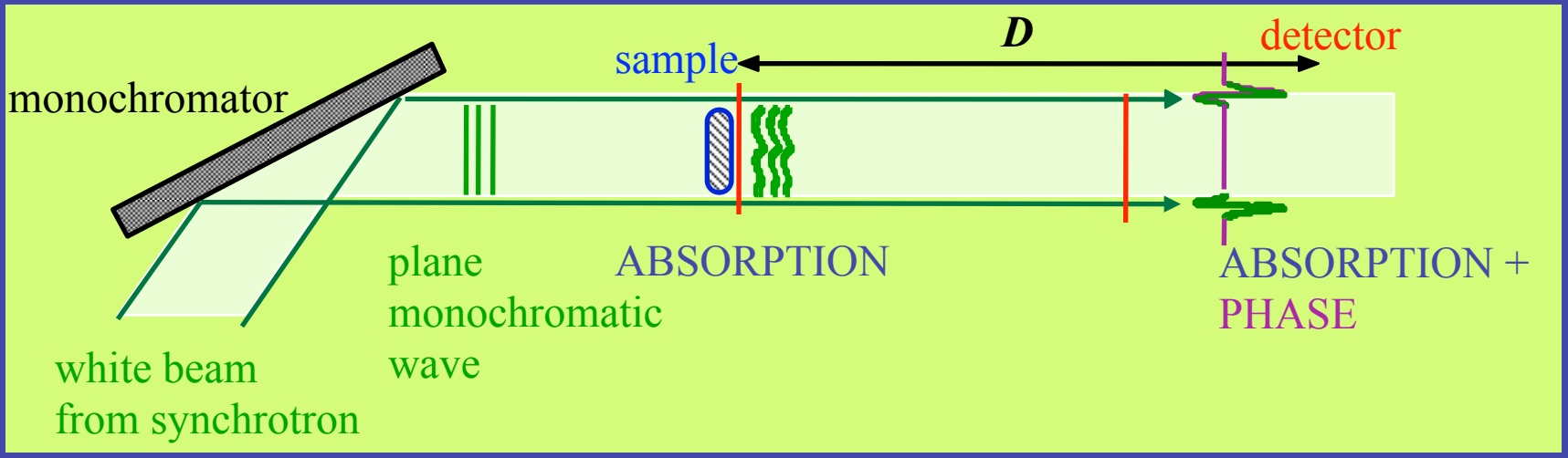

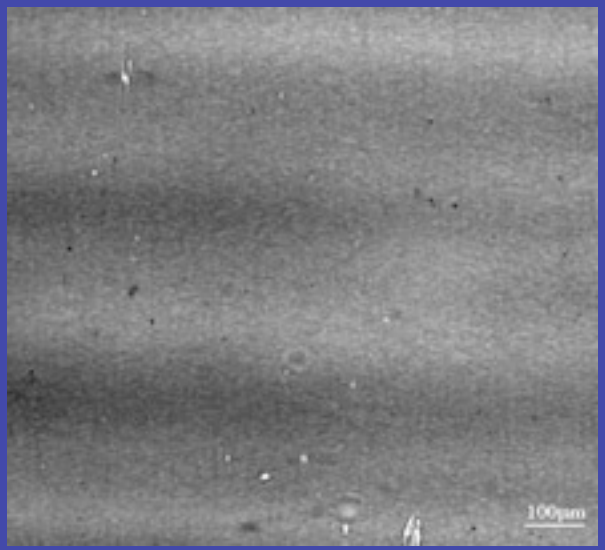

II.(A) PHASE PROPAGATION CONTRAST

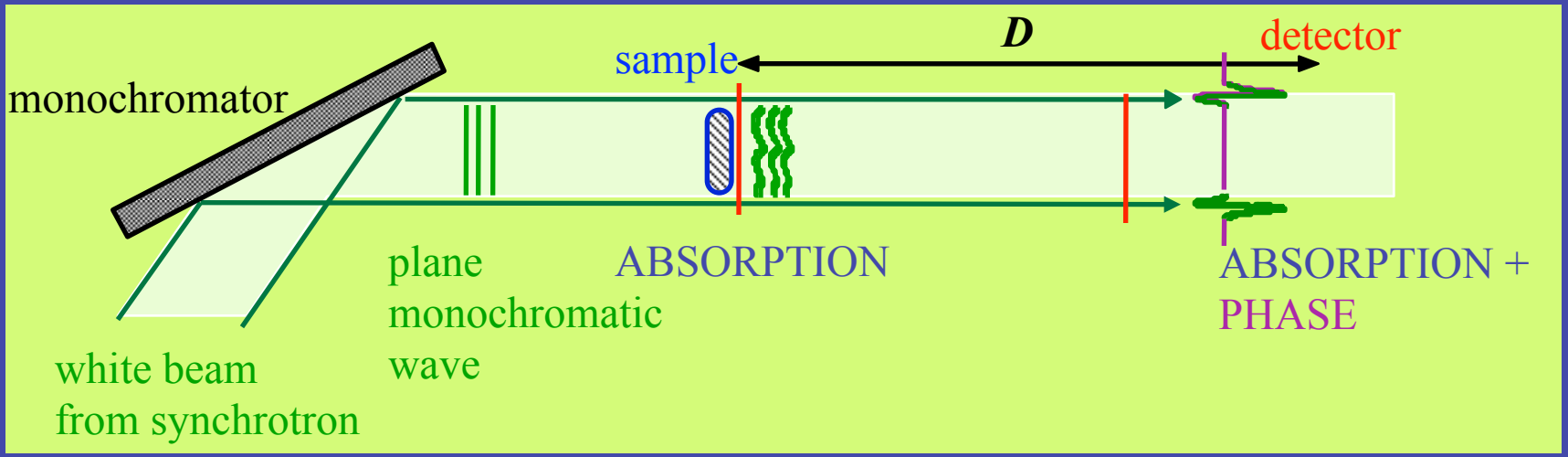

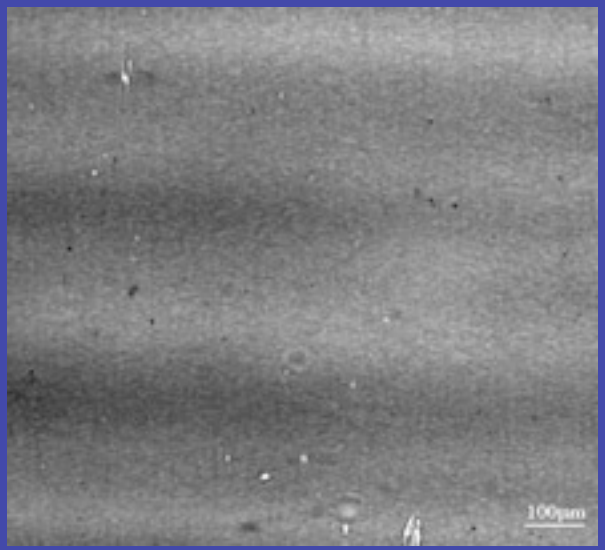

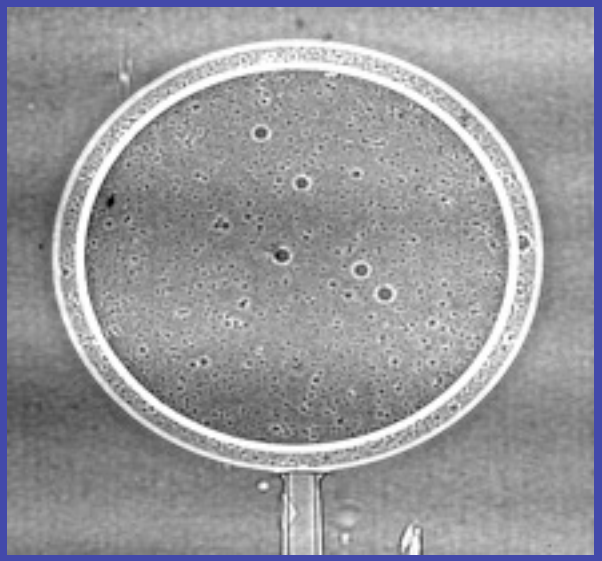

Principle of holotomography.

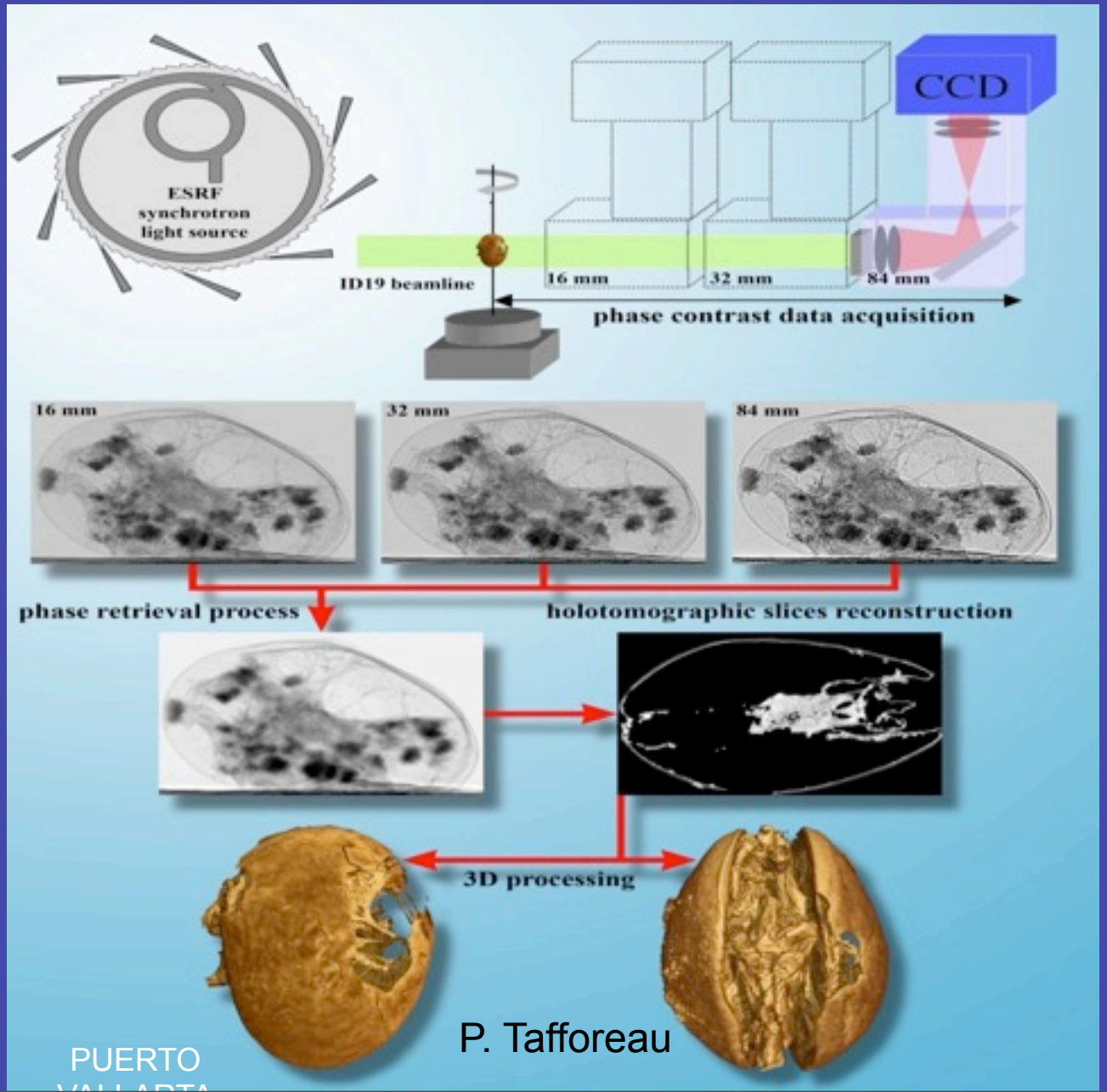

P. Tafforeau

Archaeopteryx: bird or dinosaur?

- Discovered in Germany in 1861.
- Missing link between birds and dinosaurs.

- Crow-sized, lived about 150 M years ago.
- Feathers identical to that of modern bird.

- Also had sharp teeth, a long bony tail, clawed fingers, and long feathers on its back and legs.

- This suggests that the first birds were four-winged gliders that coasted between treetops like flying squirrels.

P.TAFFOREAU and E. BUFFETAUT

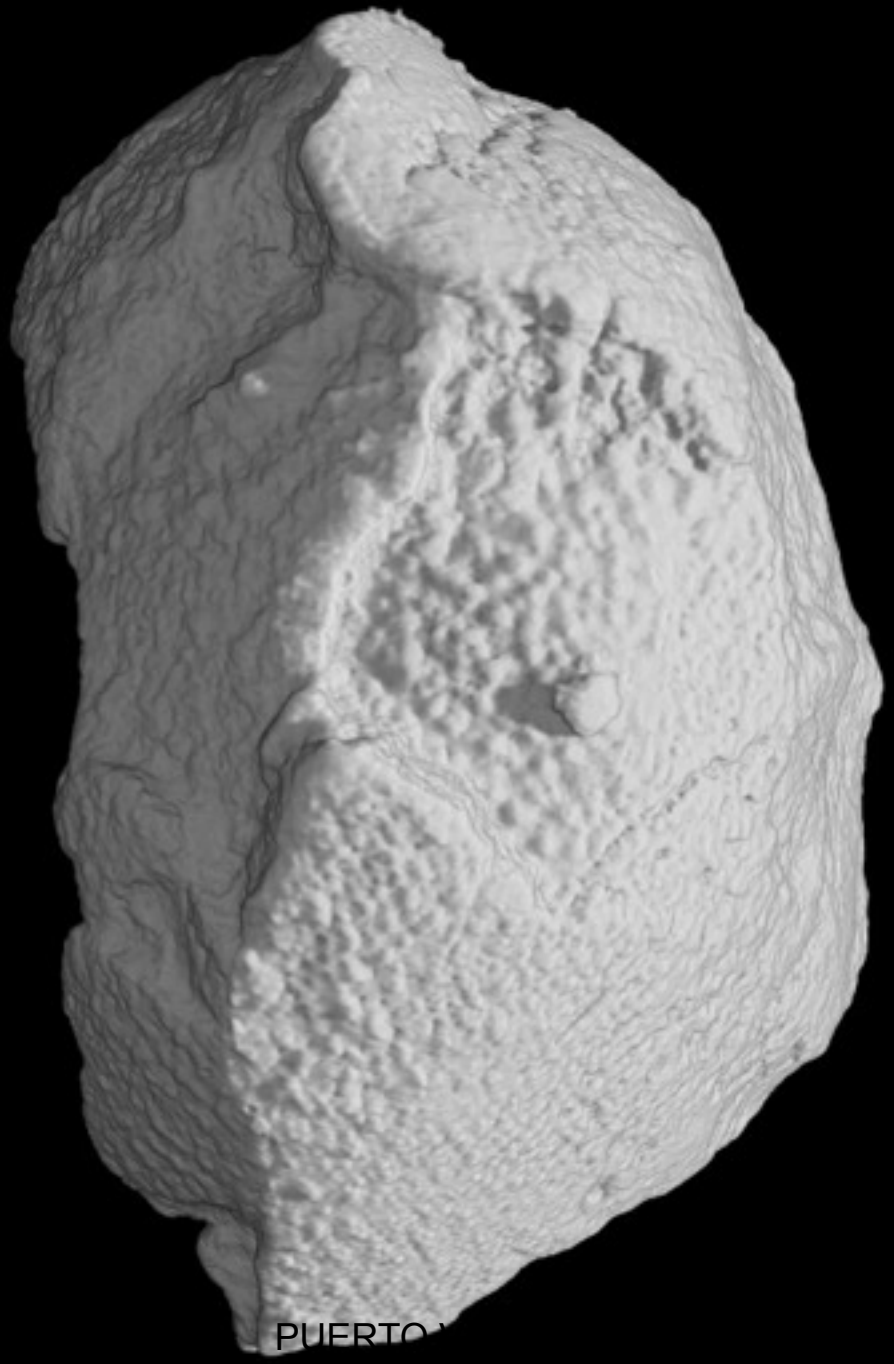
PUERTO

The impossible fish brain revealed by synchrotron

holotomography A. Pradel (a,b), M. Langer (c), J.G. Maisey (d), D. Geffard-Kuriyama (a), P. Cloetens (c), P. Janvier (a) and P. Tafforeau (c). PNAS, 106, 5225-5228 (2009).

Animal fossils are generally remains of mineralised hard tissues (i.e. understanding of the evolution of life on our planet.

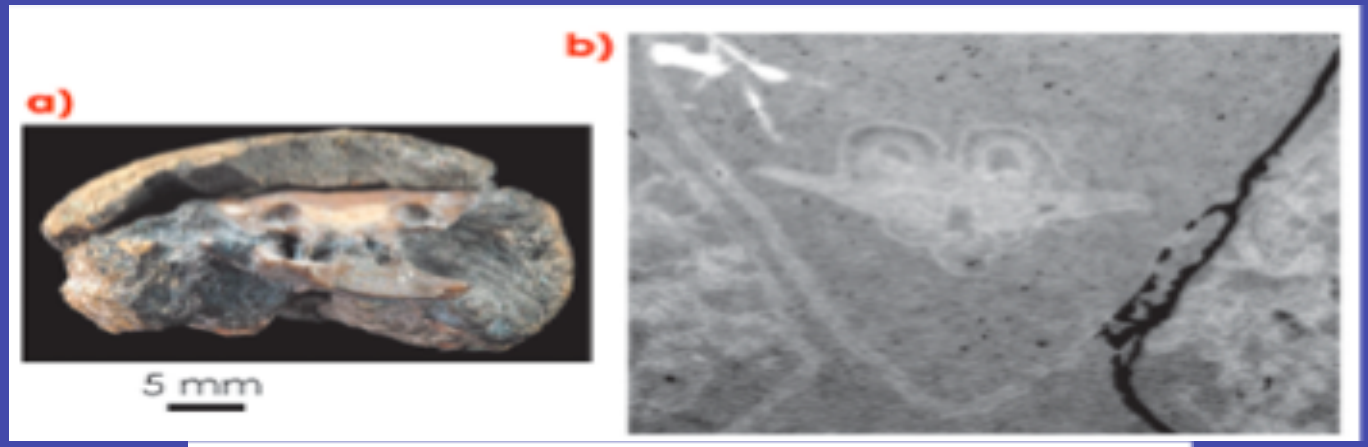

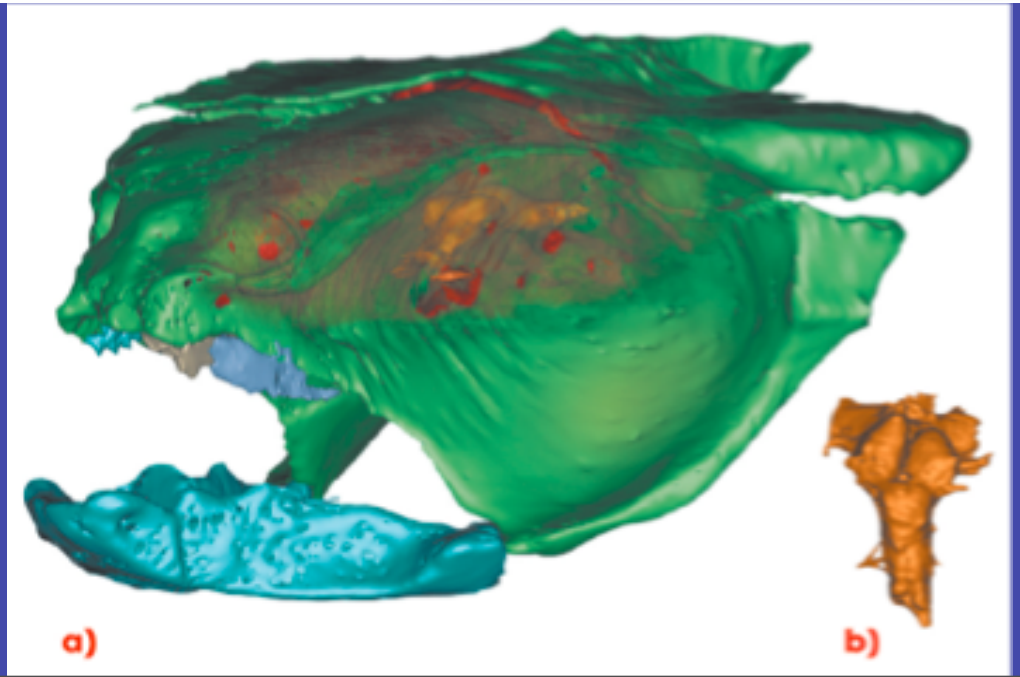

Fig. 125: 3D Rendering and virtual histological slice of a 145 million years old Cretaceous mammalian tooth from Cherves-de-Cognac (Charente, France). This minute fossil tooth was imaged using submicrometre resolution holotomography on ID19. The highly monochromatic source, in addition to short acquisition time, leads to unprecedented image quality for this kind of microfossil.
The detailed 3D morphology gives access to the internal histological information of dental microstructures including its developmental record. Study of the growth lines in such fossils should bring new evidence of the controversial physiological thermal regulation in our mammalian ancestors as well as in dinosaurs
(Courtesy: J. Pouech, J.-M. Mazin and P.Tafforeau, unpublished).

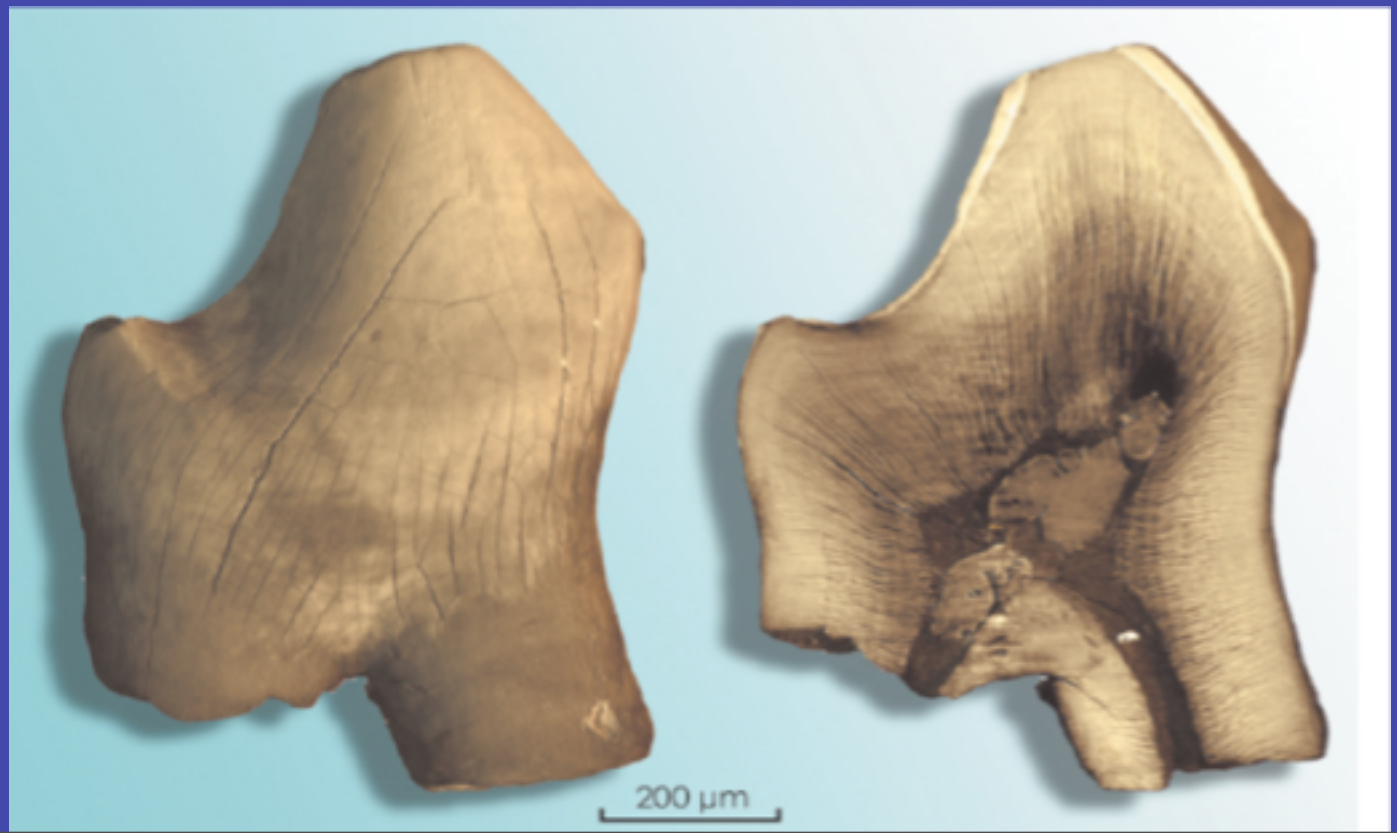

P. Verboven et al., Plant Physiology 147, 518, 2008

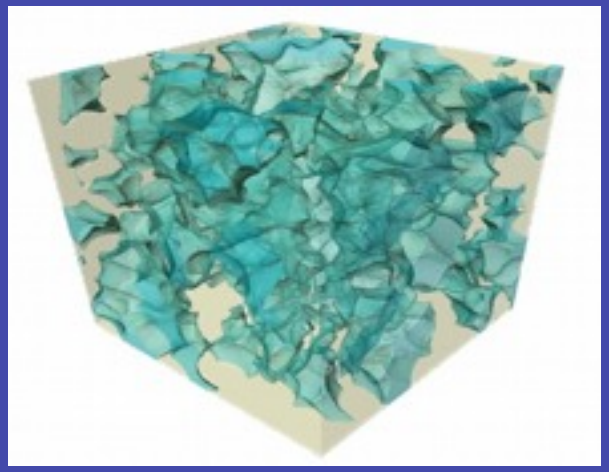

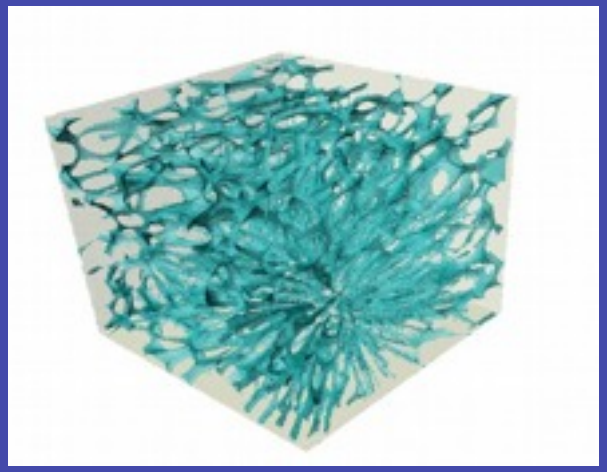

ICE CREAM, CHOCOLATE….

PHASE CONTRAST WITHOUT A 3rd GENERATION SOURCE?

a)Schematic of a Bonse–Hart interferometer

b) a shearing interferometer.

The first grating splits the incoming wave into the +1st and -1st diffraction orders, which are then recombined by a second grating with half the pitch of the first grating.

C. David et al., APL 81, 3287, 2002

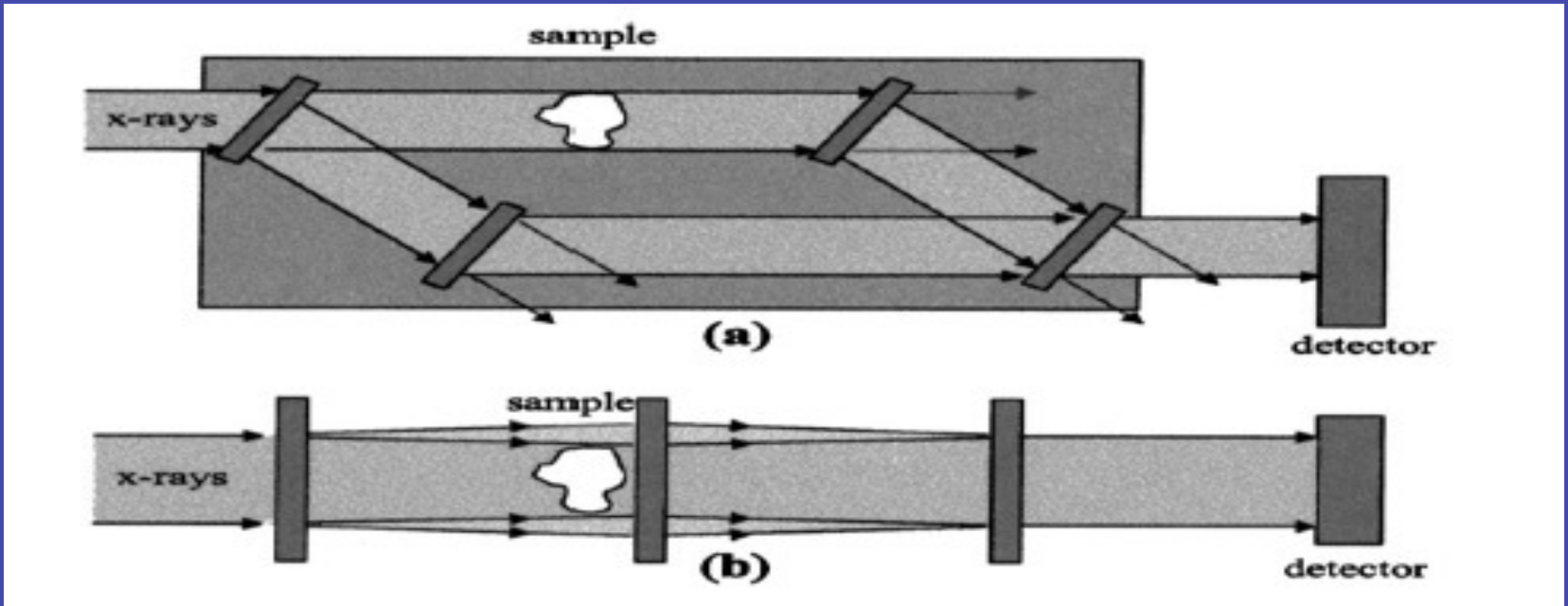

X-Ray Talbot Interferometer

- Principle: the beam splitter grating (G1) splits the incident beam into essentially two diffraction orders, which form a periodic interference pattern in the plane of the analyzer grating. A phase object in the incident beam will cause slight refraction, which results in changes of the locally transmitted intensity through the analyzer.
- (Weitkamp ., Optics Express **13** (2005) 6296-6304.).

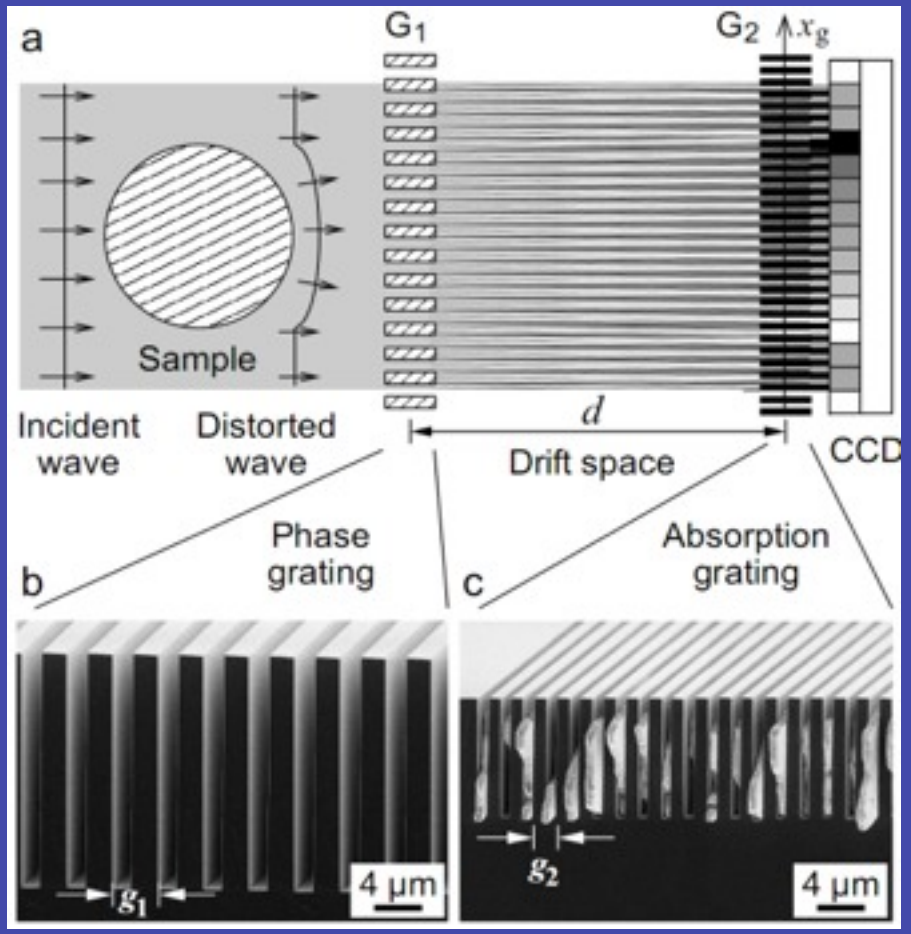

Example: mouse in formalin

Transmission tomogram

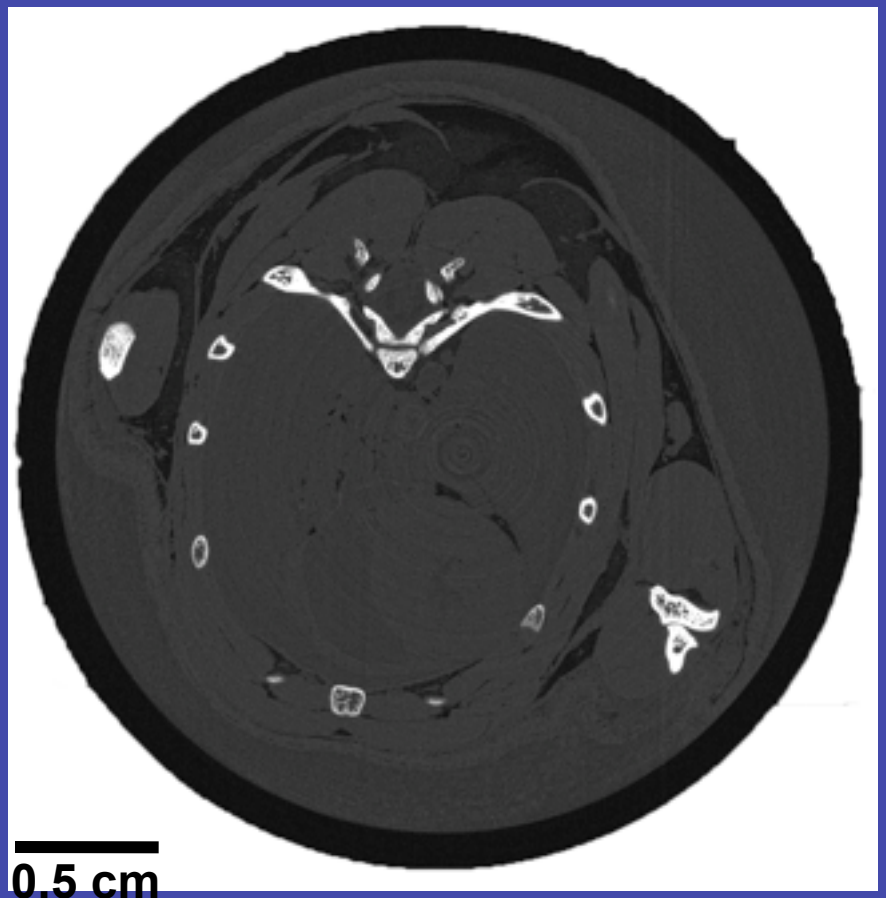

PUERTO VALLARTA

tomography of a mouse in formalin – ESRF, ID19 9–14 April 2009 – 35.0 keV
30 um pixel size

Example: mouse in formalin

Transmission tomogram

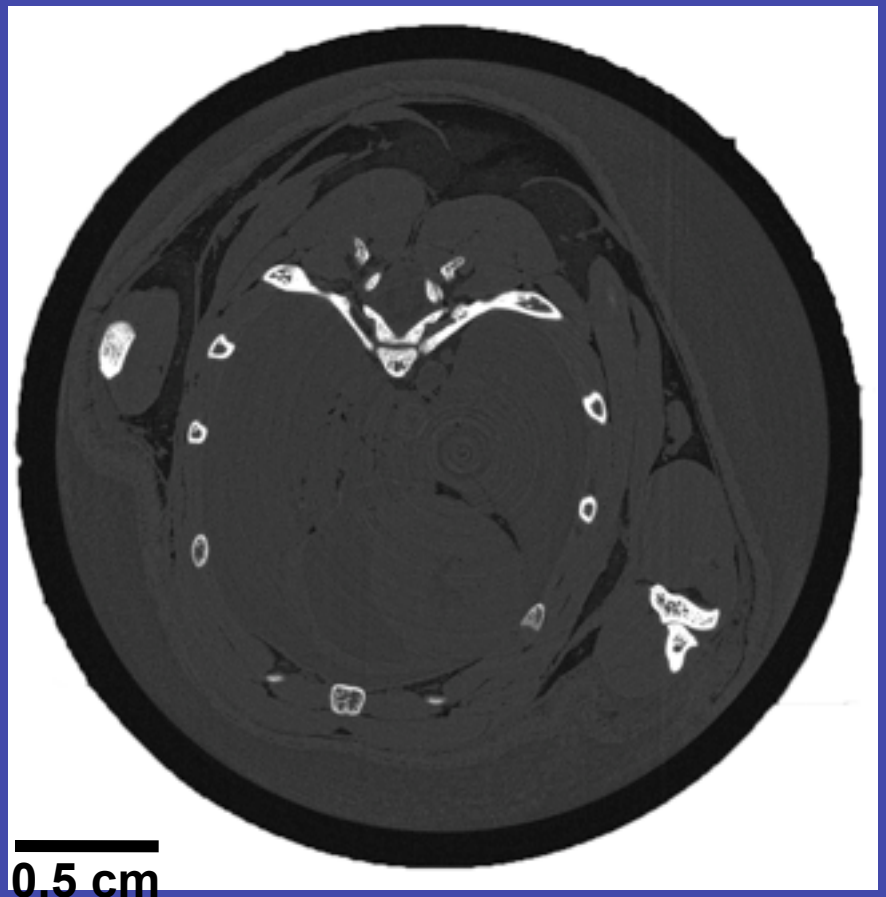

Phase tomogram

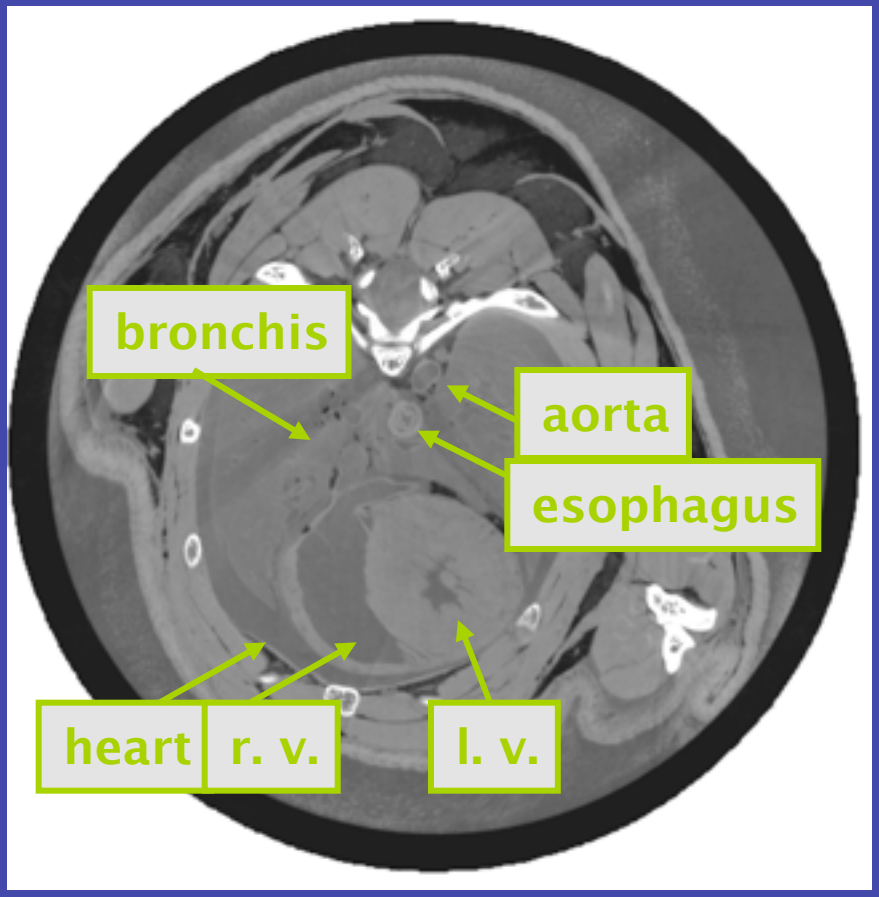

PUERTO VALLARTA

tomography of a mouse in formalin – ESRF, ID19 9–14 April 2009 – 35.0 keV
30 um pixel size

Grating-based X-ray tomography offers superior three dimensional images of the human cerebellum, which not only allow for the discrimination between grey and white matter but also between stratum moleculare and stratum granulosum. Additionally, the clear visualization of non-stained individual Purkinje cells is possible—a technique that is unrivalled so far.

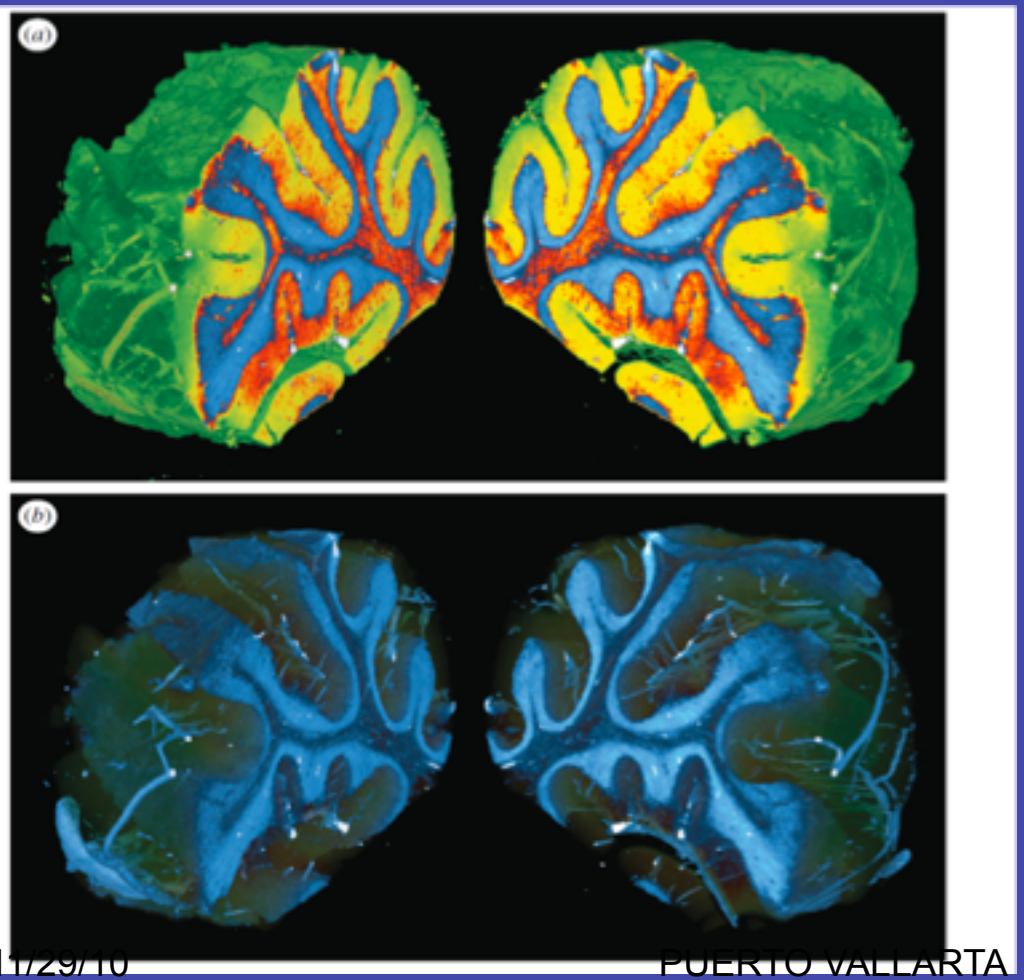

-the stratum granulosum (blue),
- the stratum moleculare (green–yellow–red gradient)
-the white matter (mainly red).
G. SHULTZ et al., J. R. Soc. Interface published on line 21/07/2010

II. (B) DIFFRACTION

W.Ludwig, S. Schmidt, E. Mejdal Lauridsen and H.F. Poulsen-Appl. Crystallography 41,302,2008

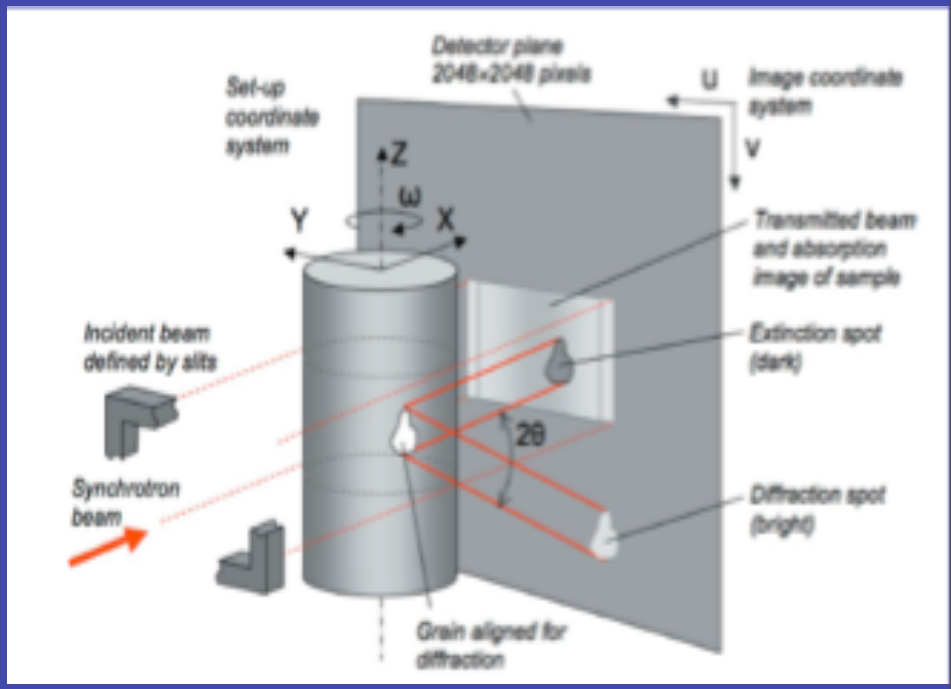

II. (B) DIFFRACTION

W.Ludwig, S. Schmidt, E. Mejdal Lauridsen and H.F. Poulsen-Appl. Crystallography 41,302,2008

- A radically different data acquisition strategy, aiming at simultaneous reconstruction of the absorption and grain microstructure of a material, has been proposed.

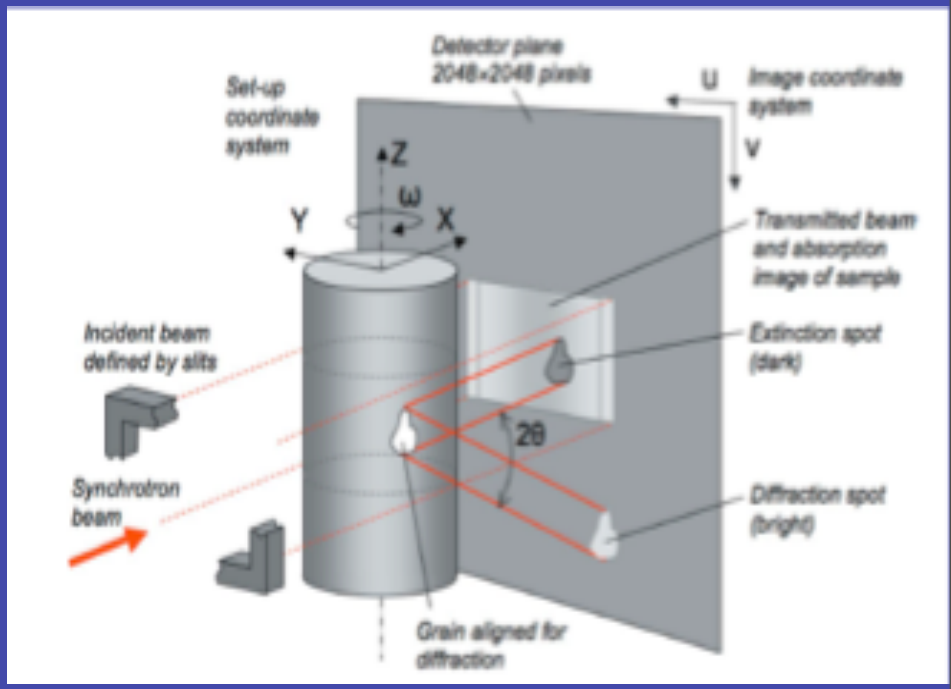

II. (B) DIFFRACTION

W.Ludwig, S. Schmidt, E. Mejdal Lauridsen and H.F. Poulsen-Appl. Crystallography 41,302,2008

- A radically different data acquisition strategy, aiming at simultaneous reconstruction of the absorption and grain microstructure of a material, has been proposed.

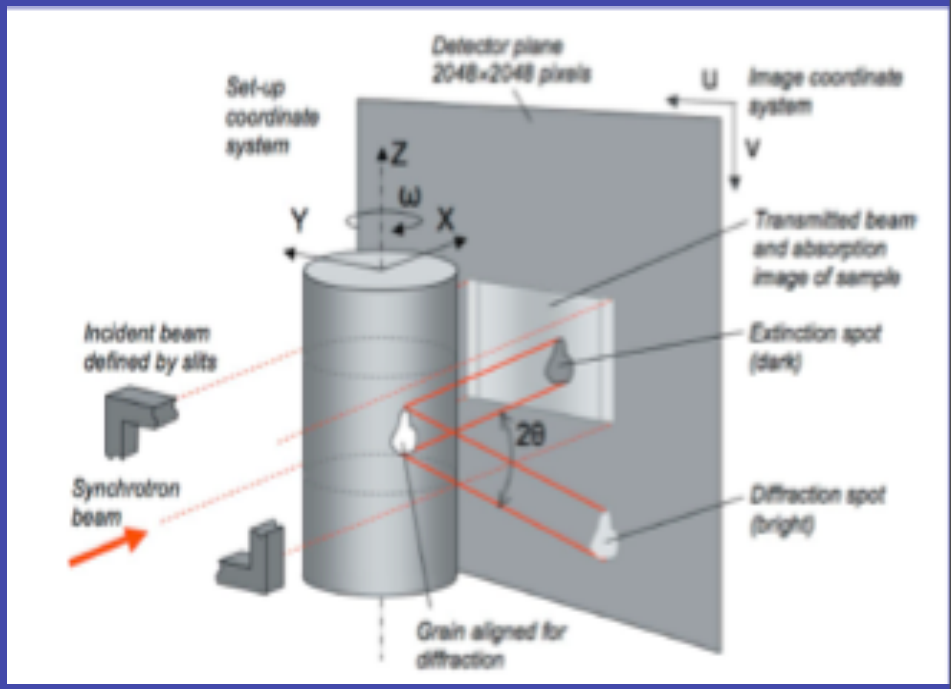

II. (B) DIFFRACTION

W.Ludwig, S. Schmidt, E. Mejdal Lauridsen and H.F. Poulsen-Appl. Crystallography 41,302,2008

- A radically different data acquisition strategy, aiming at simultaneous reconstruction of the absorption and grain microstructure of a material, has been proposed.

- The procedure is termed X-Ray diffraction contrast tomography (DCT), reflecting its similarities to conventional absorption contrast tomography. During acquisition of an optimized tomographic scan, undeformed grains embedded in the bulk of a polycrystalline sample give rise to distinct diffraction contrasts which can be observed in the transmitted beam each time a grain fulfils the Bragg diffraction condition.

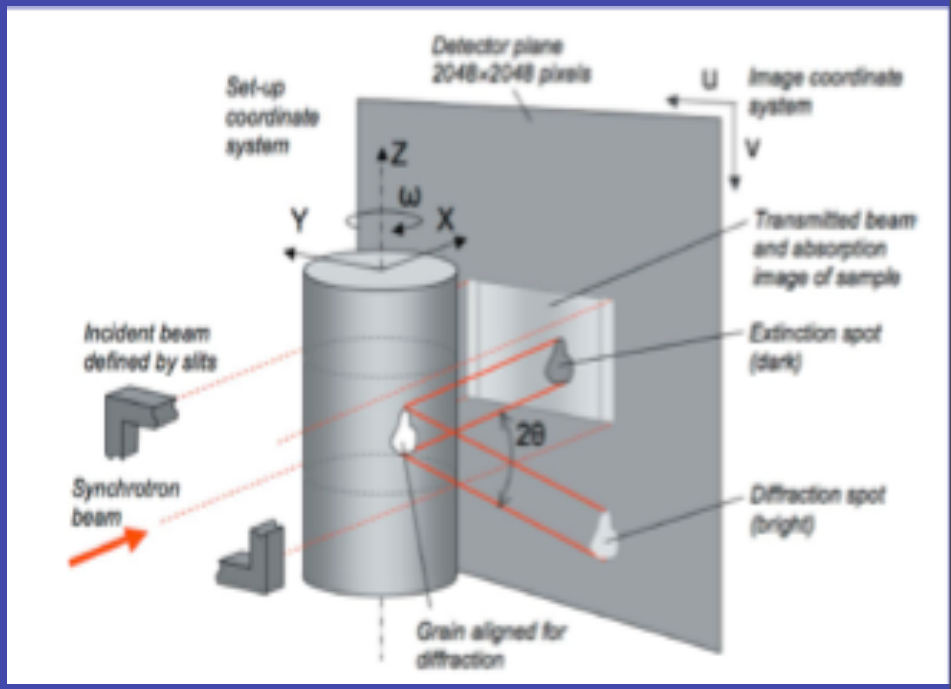

II. (B) DIFFRACTION

W.Ludwig, S. Schmidt, E. Mejdal Lauridsen and H.F. Poulsen-Appl. Crystallography 41,302,2008

- A radically different data acquisition strategy, aiming at simultaneous reconstruction of the absorption and grain microstructure of a material, has been proposed.

- The procedure is termed X-Ray diffraction contrast tomography (DCT), reflecting its similarities to conventional absorption contrast tomography. During acquisition of an optimized tomographic scan, undeformed grains embedded in the bulk of a polycrystalline sample give rise to distinct diffraction contrasts which can be observed in the transmitted beam each time a grain fulfils the Bragg diffraction condition.

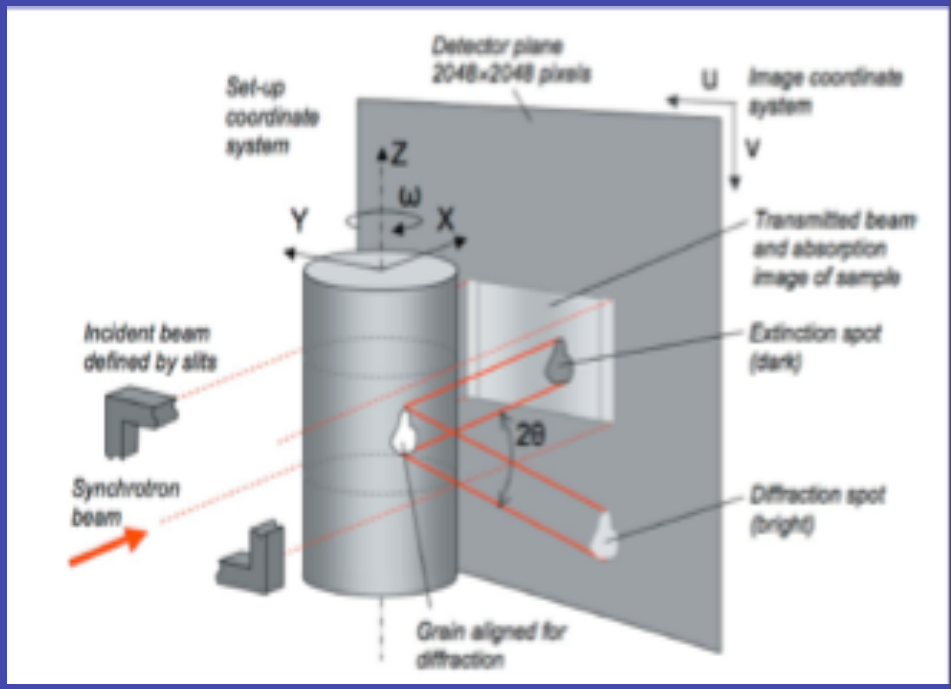

II. (B) DIFFRACTION

W.Ludwig, S. Schmidt, E. Mejdal Lauridsen and H.F. Poulsen-Appl. Crystallography 41,302,2008

- A radically different data acquisition strategy, aiming at simultaneous reconstruction of the absorption and grain microstructure of a material, has been proposed.

- The procedure is termed X-Ray diffraction contrast tomography (DCT), reflecting its similarities to conventional absorption contrast tomography. During acquisition of an optimized tomographic scan, undeformed grains embedded in the bulk of a polycrystalline sample give rise to distinct diffraction contrasts which can be observed in the transmitted beam each time a grain fulfils the Bragg diffraction condition.

- By extracting and sorting these contrasts into groups belonging to individual grains, one is able to reconstruct the 3D grain shapes by means of parallel beam, algebraic construction techniques.

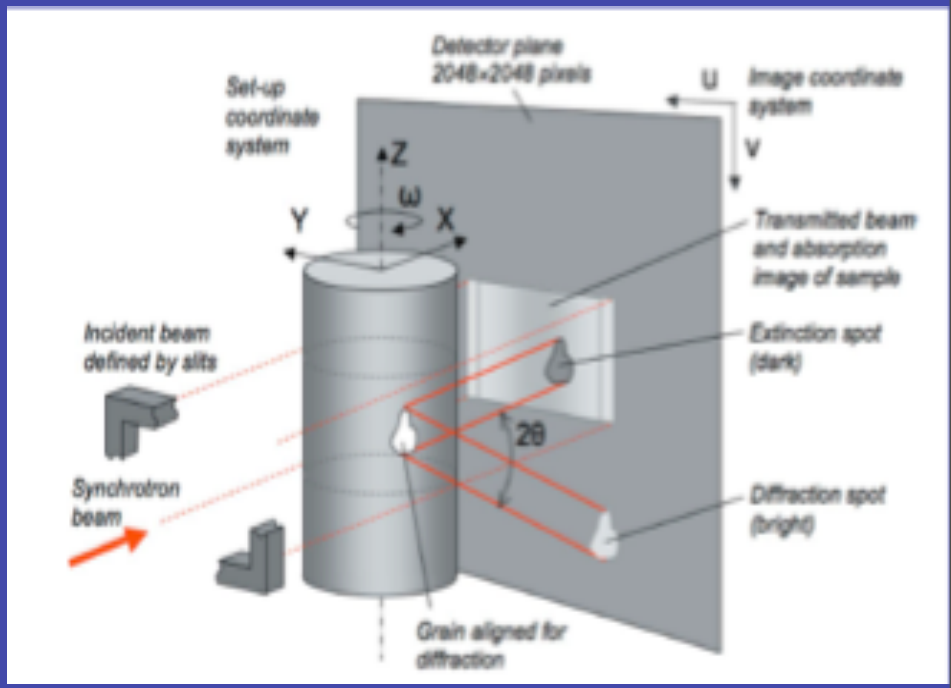

TRACKING CORROSION CRACKING

→ During fabrication and operation, many stainless steel components are exposed to mechanical loads that create high strains inside the material, which results in mechanical failures at unexpectedly low loads.

→ Recently, King, Johnson, Engelberg, Ludwig &Marrow(SCIENCE 382, 321,2008) have shed light on the microscopic origin of environmental corrosion by studying crack formation in situ, such as an acidified solution of $K_2S_4O_6$ on the polycristalline grain structure of samples in an electrochemical cell.

→ They combine grain reconstruction with an in situ localization of corrosion processes inside the sample.

→ They use for that DCT(Diffraction Contrast Tomography) and CT (Computed Tomography)

→In these studies, the spatial resolution is 1μm. Next step: 50 nm

Fig. 1. Part of the 3D grain map obtained by DCT, including 169 grains (a total of 362 grains were mapped). The circumference of the sample is outlined, and the plane of the 2D section in Fig. 3 is also shown.

(**A**) Grains colored using a RBG scale, according to their crystallographic orientation.

(**B**) Low CSL grain boundaries are shown in color: low-angle Σ 1(orange), twins Σ 3 (red), Σ 9 (blue), other boundaries Σ< 29 (purple)

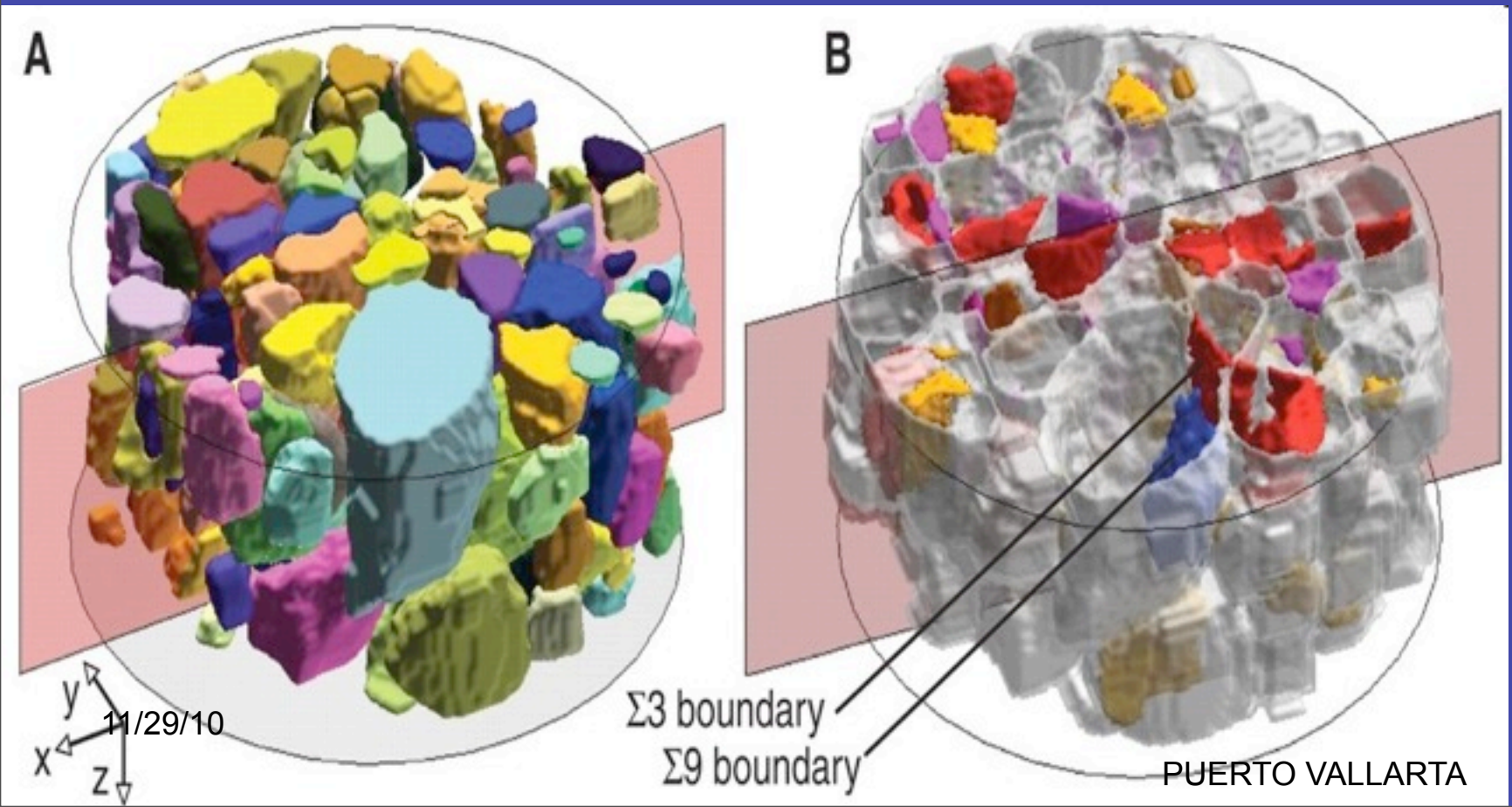

→ Combined use of Diffraction Contrast Tomography (DCT) and Computed Tomography (CT) data to identify crack bridging grain boundary structure

(A) Cracks obtained from CT data are shown in black, at the final step before sample failure, and compared with DCT data of 3D grain shapes.

(B) 2D section of the grain boundaries, identified by DCT, compared with the crack path identified by CT. The boundaries are colored as in Fig.1, and a crack bridge is shown.

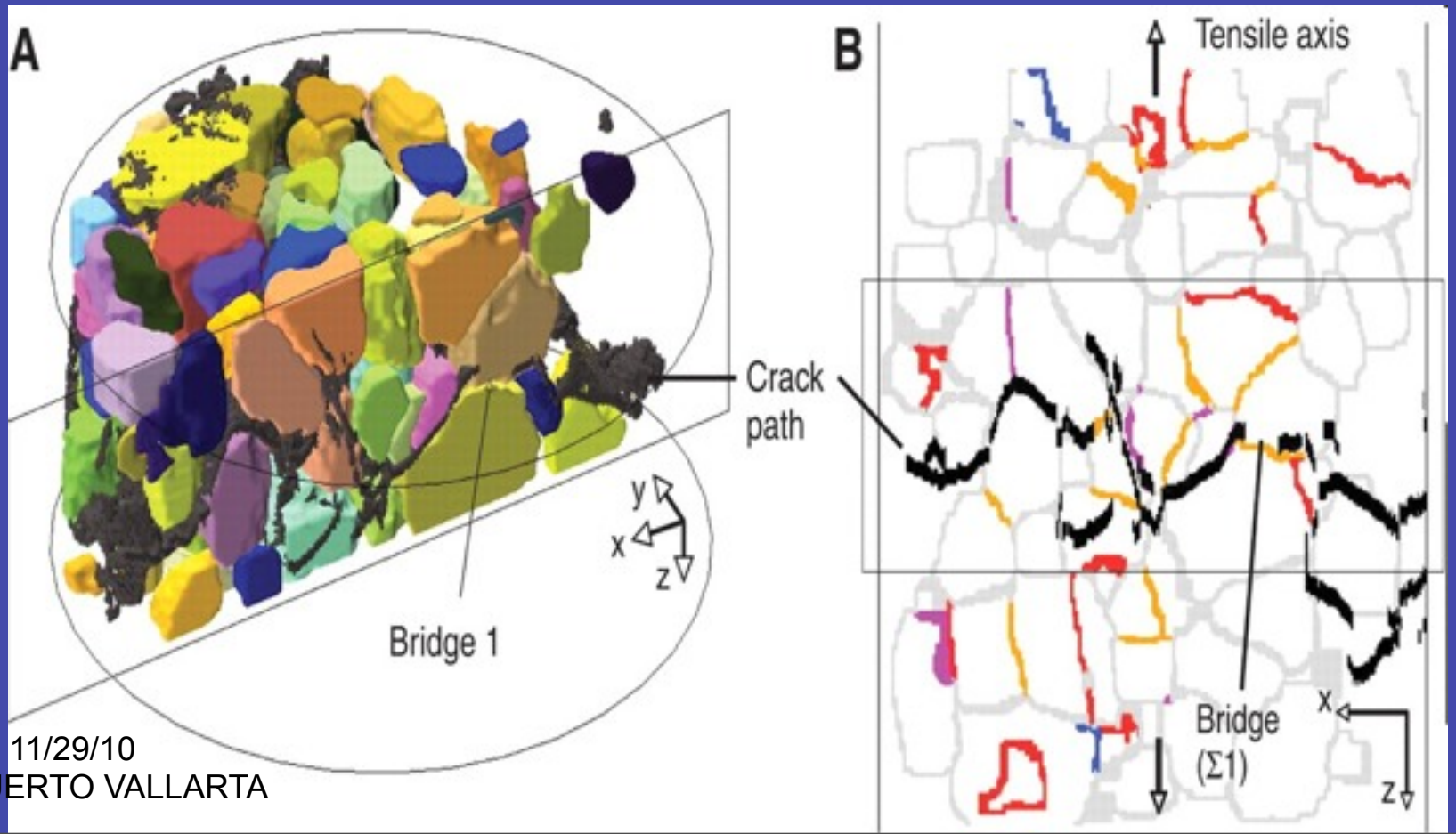

Morphological clues to wet granular pile stability

M. SCHEEL[1], R. SEEMANN[1], M. BRINKMANN[1], M. DI MICHIEL[2], A. SHEPPARD[3], B. BREIDENBACH[4] AND S. HERMINGHAUS[1]*

[1] Max Planck Institute for Dynamics and Self-Organization, Bunsenstr. 10, D-37073 Göttingen, Germany
[2] European Synchrotron Radiation Facility, BP 220, F-38043 Grenoble Cedex, France
[3] Dept. Appl. Math., Australian National University, Canberra ACT 0200, Australia
[4] Institut für Theoretische Physik, Universität Erlangen-Nürnberg, Staudtstrasse 7, D-91058 Erlangen, Germany
*e-mail: stephan.herminghaus@ds.mpg.de

- *When a granular material such as sand is mixed with a certain amount of liquid, the surface tension of the latter bestows considerable stiffness to the material, which enables sand castles to be sculpted*
- The geometry of the liquid interface within the granular pile is of extraordinary complexity and strongly varies with the liquid content.
- *Surprisingly, the mechanical properties of the pile are largely independent of the amount of liquid over a wide range.*
- This puzzle has been resolved with the help of X-Ray microtomography, showing that the remarquable insensitivity of the mechanical properties to the liquid content is due to the particular organization of the liquid in the pile into open structures

Liquid bridge form at the contact between grains, as a result of surface tension
a,Fluorescence microscopy image of liquid bridges between 375- μm-diameter glass beads.
b, Schematic of a liquid bridge (blue) between spherical surfaces (yellow). θ is the liquid–solid contact angle, φ is the half-filling angle, defined as $\varphi = \tan^{-1}(r/R)$, where r is the radius of the liquid bridge, and R is the radius of the grain.

The curvature of the liquid interface leads to low pressure in the liquid causing a force of attraction between grains

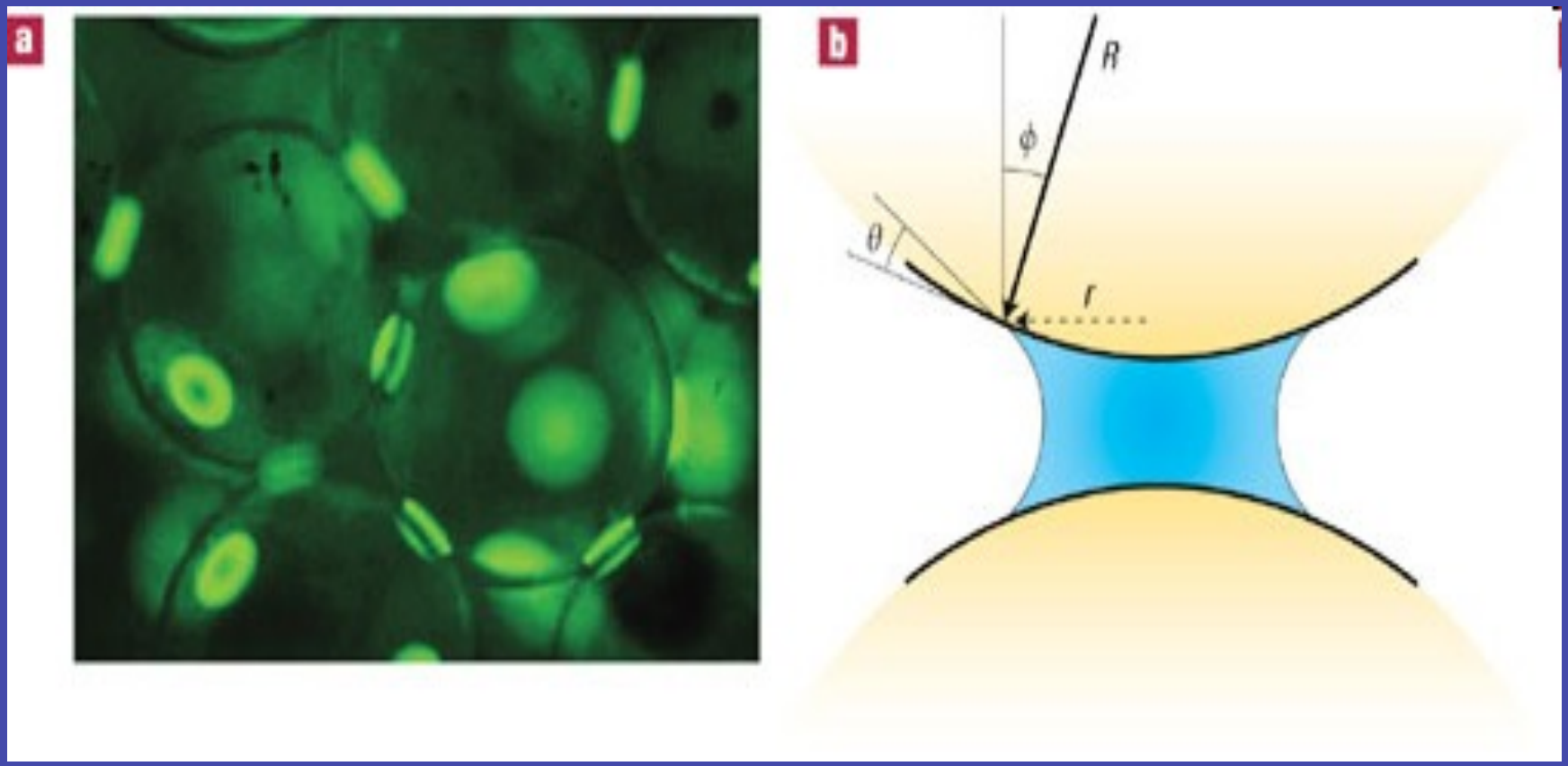

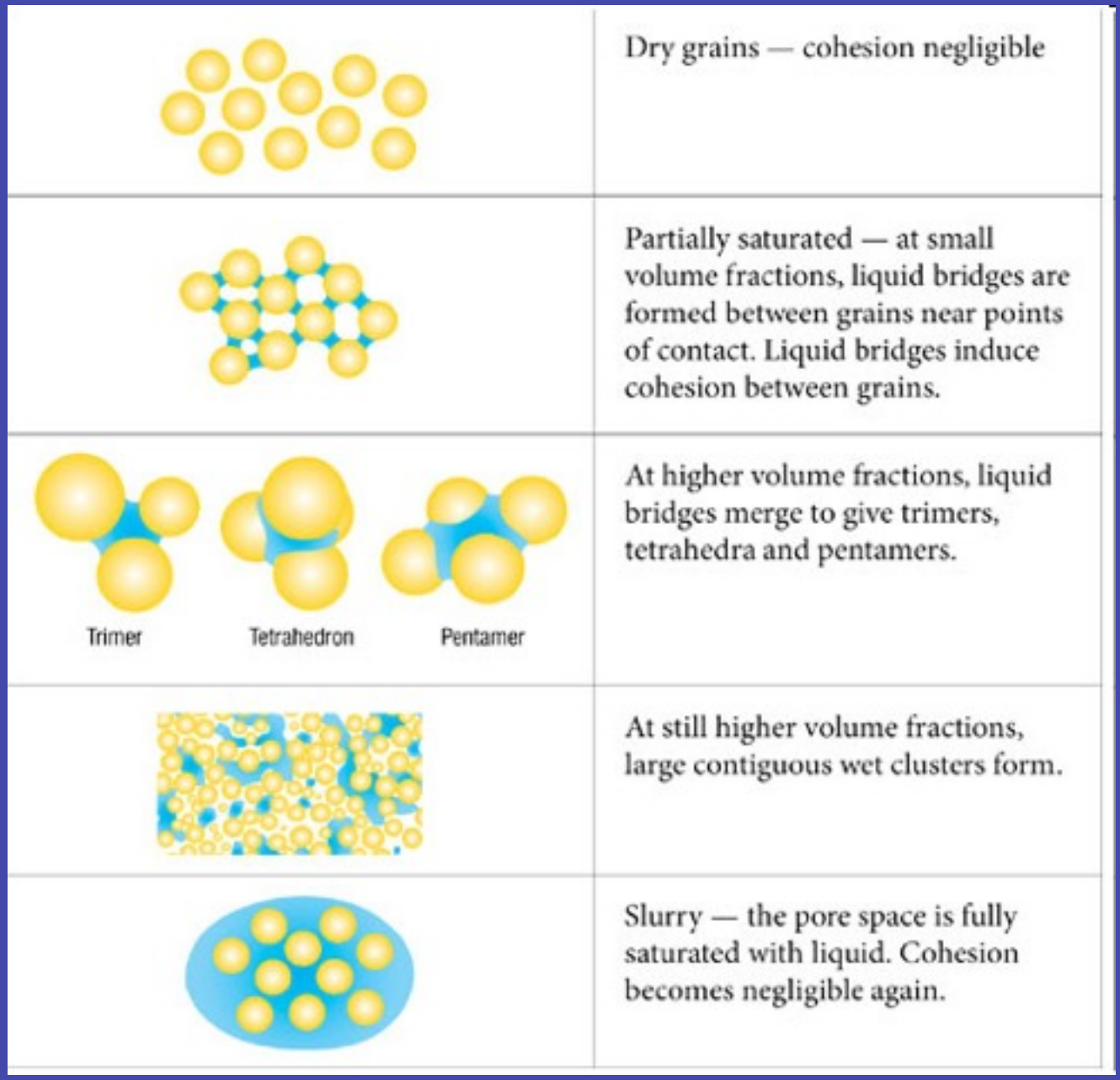

(from Arshad Kudrolli Nature Materials 7, 175, 2008)

a, Top row: Capillary bridge (cb), trimer (tr), pentamer (pt) and filled tetrahedra (th) as obtained from X-ray tomography. Bottom row: As obtained numerically.

. **b**, Fraction of a large percolating liquid cluster (X-ray tomography)

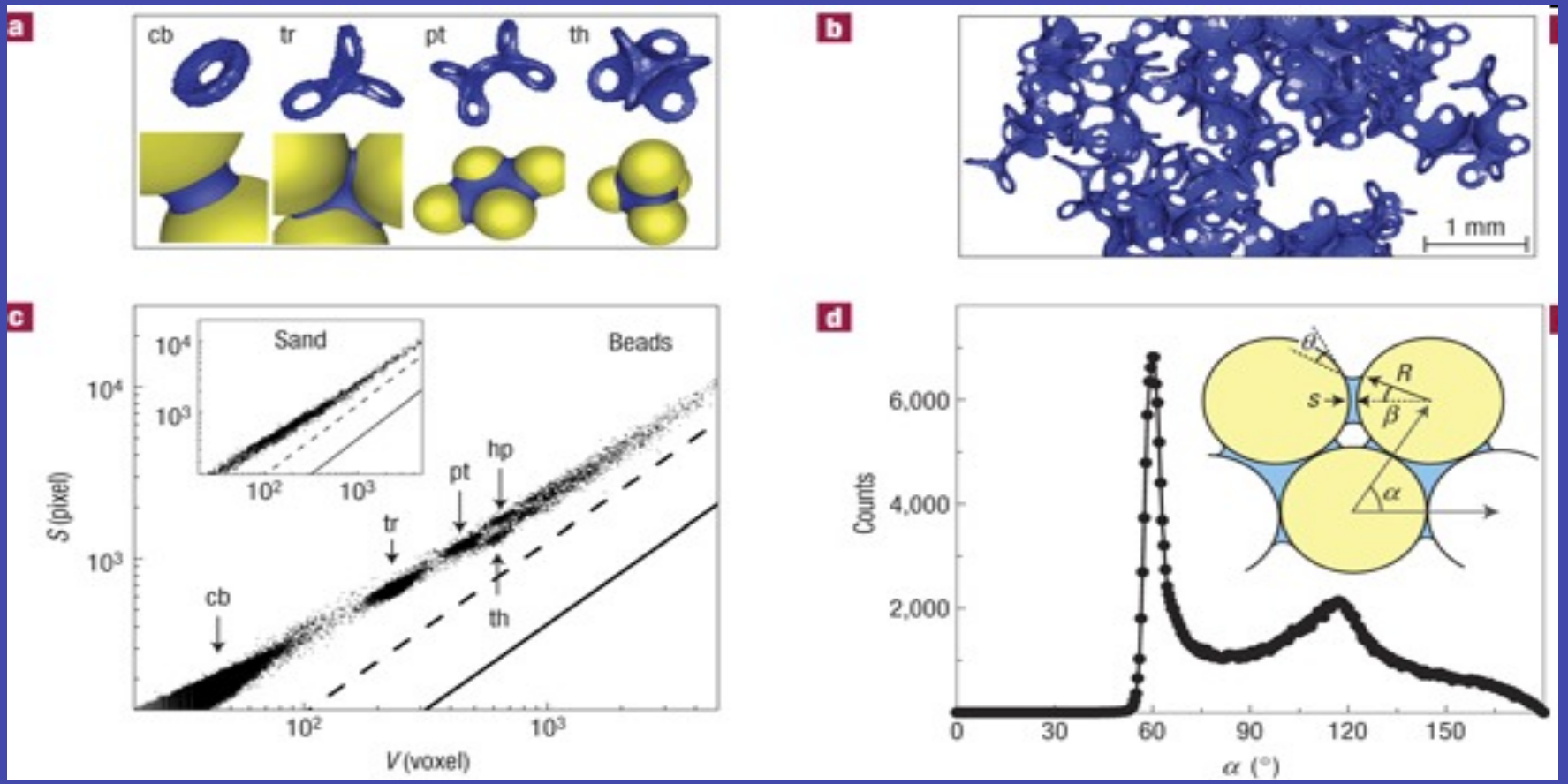

c, Cumulative plot of the total liquid surface area versus the volume of all clusters appearing at W (liquid content) =0.035, as obtained by X-ray microtomography (hp: heptamers).

d, Distribution of angular distances between two neighbouring contact points (threshold separation 0.05 R). Inset: Schematic diagram of a capillary bridge at bead separation s, and two trimers.

PUERTO VALLARTA

3. EXPLOITATION OF THE COHERENCE

3. EXPLOITATION OF THE COHERENCE

There are different ways to do microscopy in the hard X-Ray:

3. EXPLOITATION OF THE COHERENCE

There are different ways to do microscopy in the hard X-Ray:

→ By using lenses (Fresnel, refractive..), mirrors or capillaries. For the moment the resolution is limited to 100-50 nm.

3. EXPLOITATION OF THE COHERENCE

There are different ways to do microscopy in the hard X-Ray:

→ By using lenses (Fresnel, refractive..), mirrors or capillaries. For the moment the resolution is limited to 100-50 nm.

→ By coherent X-Ray diffraction imaging (CDXI).

● In CDXI, the object is illuminated with coherent X-rays and its far-field diffraction pattern is recorded without any optic. From this diffraction pattern, the wave field behind the object is reconstructed by iteratively solving the phase problem. 3D imaging is possible by recording a (tomographic) series of diffraction patterns. Coherent illumination of the object is crucial to this this technique, and the coherent dose on the sample determines the spatial resolution. As the coherent flux at modern SR sources is limited, CDXI experiments require nanofocusing: a resolution of 5 nm has been achieved with 100 nm focusing.

3. EXPLOITATION OF THE COHERENCE

There are different ways to do microscopy in the hard X-Ray:

→ By using lenses (Fresnel, refractive..), mirrors or capillaries. For the moment the resolution is limited to 100-50 nm.

→ By coherent X-Ray diffraction imaging (CDXI).

● In CDXI, the object is illuminated with coherent X-rays and its far-field diffraction pattern is recorded without any optic. From this diffraction pattern, the wave field behind the object is reconstructed by iteratively solving the phase problem. 3D imaging is possible by recording a (tomographic) series of diffraction patterns. Coherent illumination of the object is crucial to this this technique, and the coherent dose on the sample determines the spatial resolution. As the coherent flux at modern SR sources is limited, CDXI experiments require nanofocusing: a resolution of 5 nm has been achieved with 100 nm focusing.

● Coherent diffraction imaging emerged from the realization by Sayre (1952) that oversampled diffraction patterns can be inverted to obtain real-spaces images.

3. EXPLOITATION OF THE COHERENCE

There are different ways to do microscopy in the hard X-Ray:

→ By using lenses (Fresnel, refractive..), mirrors or capillaries. For the moment the resolution is limited to 100-50 nm.

→ By coherent X-Ray diffraction imaging (CDXI).

● In CDXI, the object is illuminated with coherent X-rays and its far-field diffraction pattern is recorded without any optic. From this diffraction pattern, the wave field behind the object is reconstructed by iteratively solving the phase problem. 3D imaging is possible by recording a (tomographic) series of diffraction patterns. Coherent illumination of the object is crucial to this this technique, and the coherent dose on the sample determines the spatial resolution. As the coherent flux at modern SR sources is limited, CDXI experiments require nanofocusing: a resolution of 5 nm has been achieved with 100 nm focusing.

● Coherent diffraction imaging emerged from the realization by Sayre (1952) that oversampled diffraction patterns can be inverted to obtain real-spaces images.

● It was demonstrated by Miao,Charalambous, Kirz and Sayre in 1999 (Nature 400, 342).

Coherent X-Ray Diffraction Imaging: 3D mapping of a deformation field inside a nanocrystal. Pfeifer, Williams, Vartanyants, Harder&Robinson. Nature 442, 63, 2006

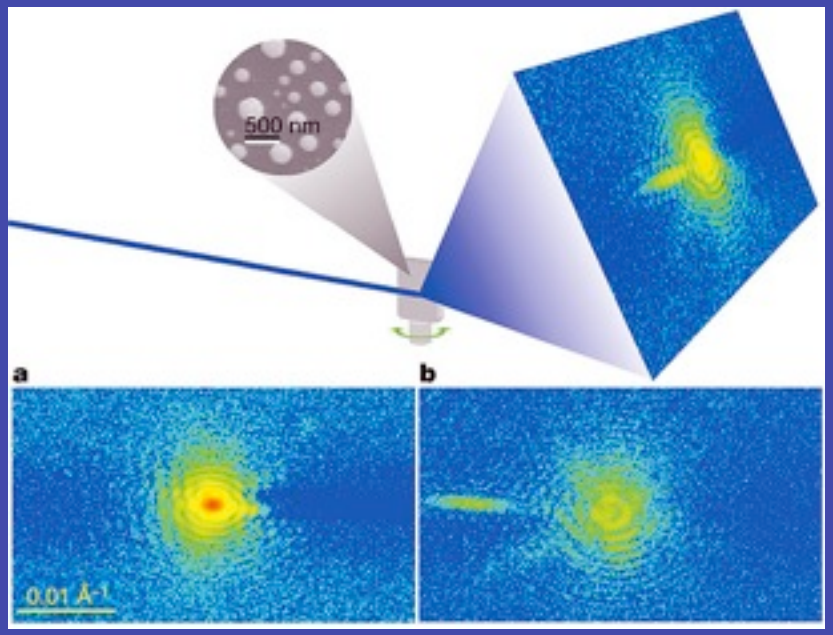

- Pb is evaporated (20 nm)/Si. Aftermelting→moltendroplets→isolated hemispherical crystals. A CCD X-Ray detector is centred on the (111) Bragg peak of one of the crystals, to give the diffraction peak shown below (λ = 1.38Å, APS)

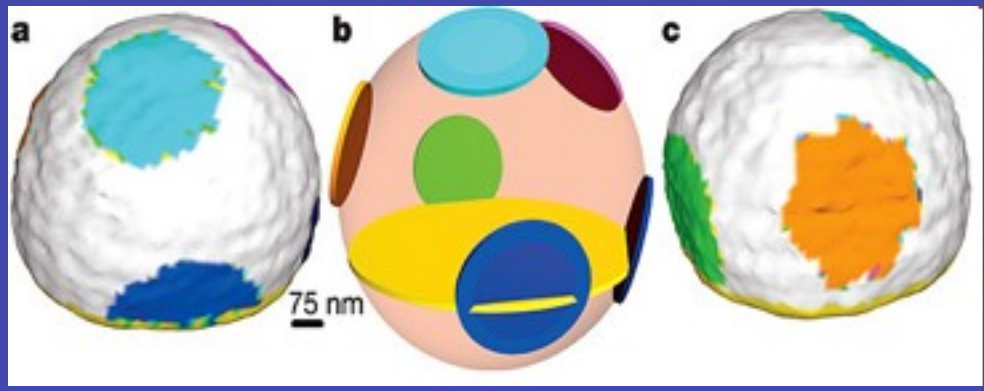

→ The diameter of the nanocrystal is 750 nm and the resolution 40 nm

→ *Diffraction also opens the new possibility of directly imaging the strain field within the crystal because it breaks the local symmetry of a diffraction pattern around a Bragg peak*

→ The strain (yellow) is superposed on a translucent image of the nanocrystal itself (grey)

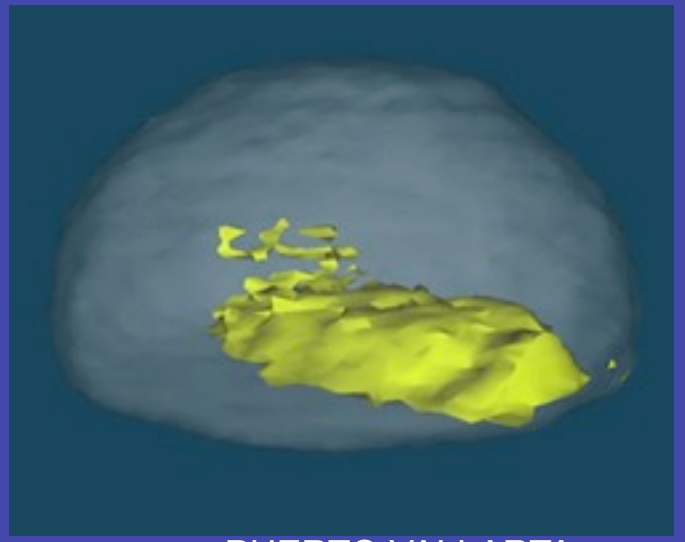

MICROSCOPY WITHOUT LENSES OR MIRRORS: Takahashi, Zettsu, Nishino, Tsutsumi, Matsubara, Ishikawa&Yamauchi NanoLetters 10, 1922, 2010

- **Synchrotron X-rays are focused on a 1-μm-diameter spot through KB mirrors, and a sample (Au/Ag nanobox) is placed on the spot. The intensity distribution of X-rays elastically scattered in the forward direction (coherent X-ray diffraction patterns) is measured by a charge-coupled device (CCD) X-ray detector. The obtained coherent X-ray diffraction patterns are processed by a computer to reconstruct a three-dimensional image of the sample structure. In the reconstruction, coherent X-ray diffraction patterns from different incident angles, obtained by rotating the sample, are used.**

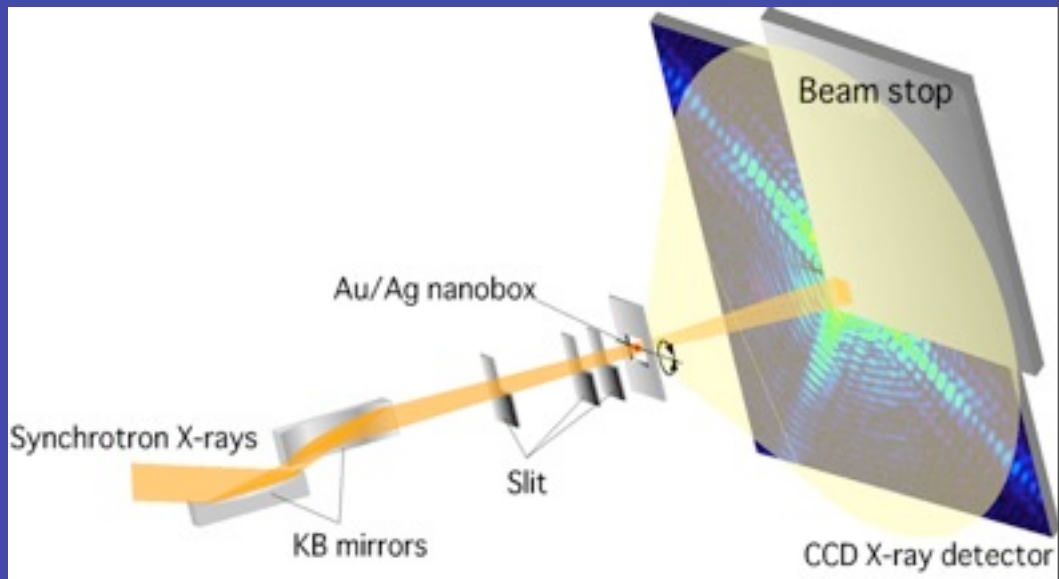

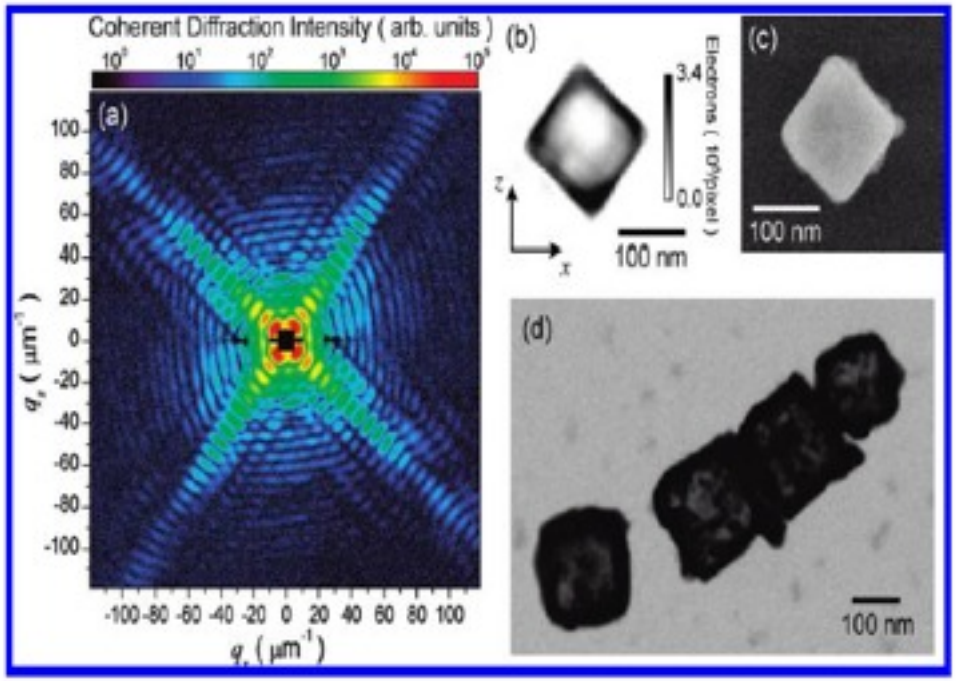

(a) Coherent diffraction pattern of an Au/Ag nanobox in 1251 × 1251 pixels. q is defined as |q|) 2 sin(Θ/2)/λ, where Θ is the scattering angle and λ is the X-ray wavelength.

(b) Reconstructed projection image of coherent X-ray diffraction data.

(c) SEM image of same nanobox.

(d) TEM image of different nanoboxes.

- A three-dimensional electron density distribution is obtained by performing a phase retrieval calculation with respect to the coherent X-ray diffraction patterns of a Au/Ag nanobox observed with different X-ray incident angles. The detailed surface structure of the Au/Ag nanobox can be observed when an equivalent-electron-density plane is displayed. Small pits and a large pit are confirmed at the positions indicated by the blue and green arrows, respectively.

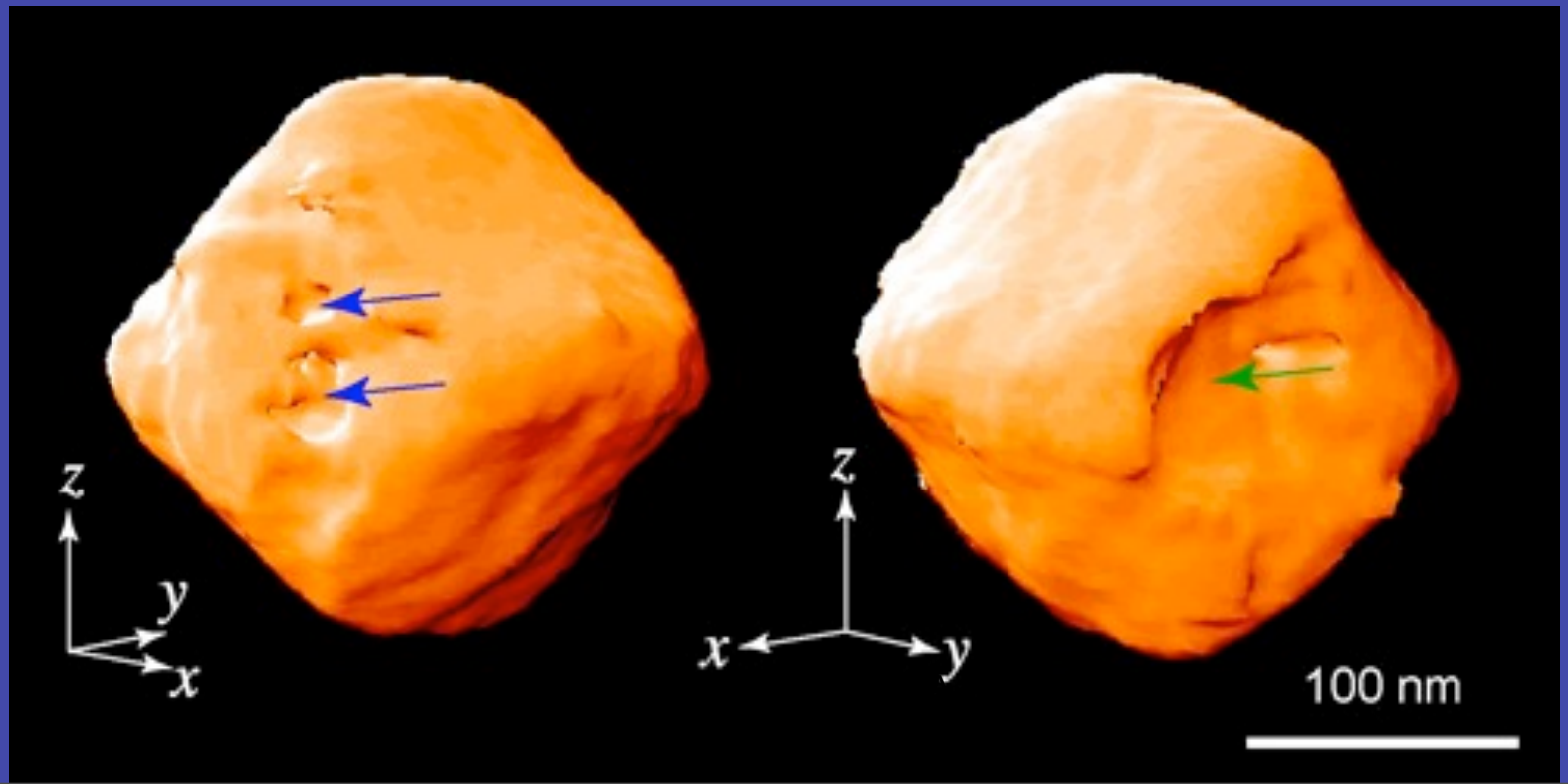

- Cross-sectional views of a Au/Ag nanobox can be obtained by slicing the image of its 3D electron density distribution at arbitrary cross sections.

- The obtained cross-sectional images can be displayed as 2D electron density distributions. The spatial resolution of the cross-sectional profiles was found to be higher than 10 nm by analyzing the cross section of the thinnest structure in the cross-

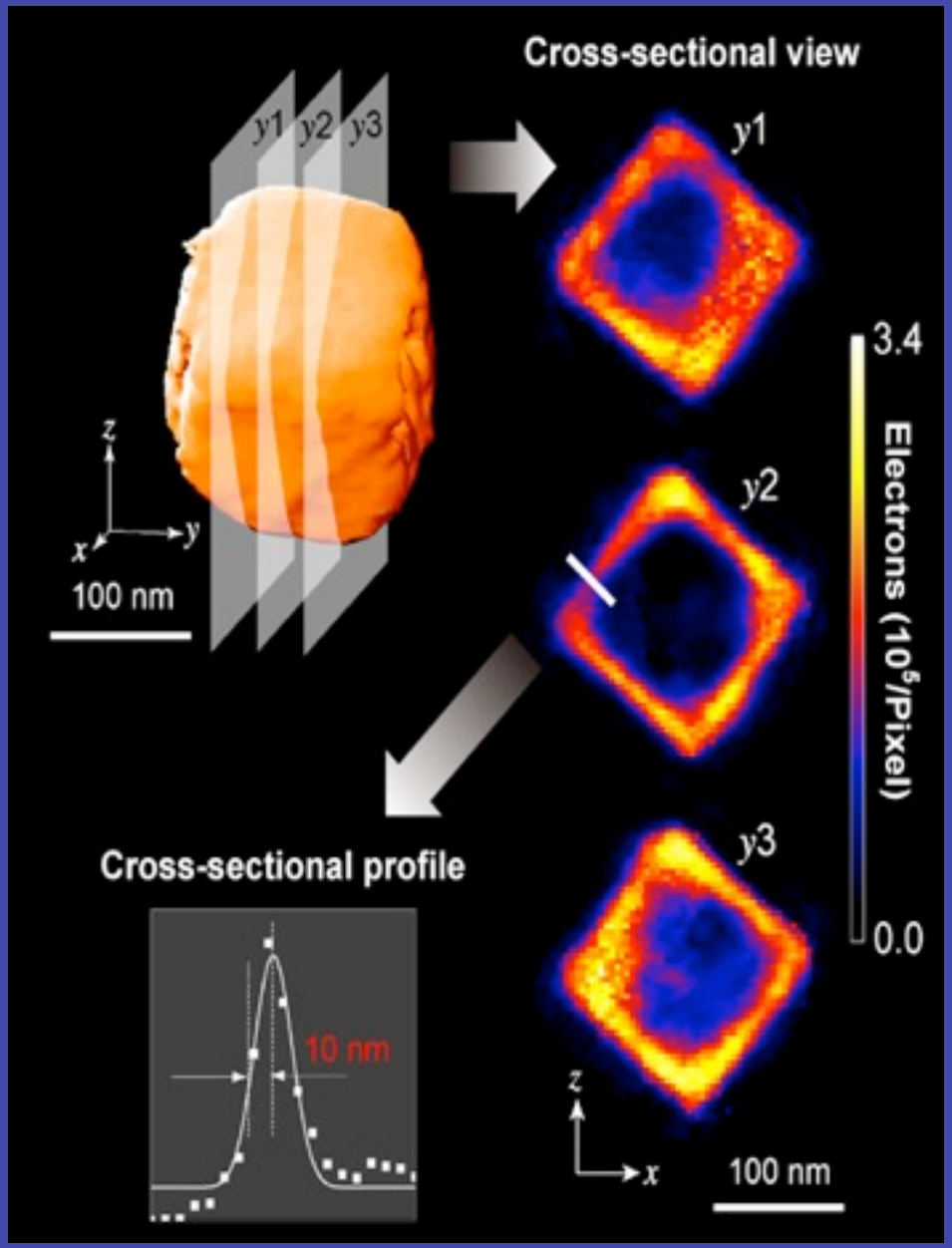

II. (C) COHERENT DIFFRACTION

→ A small gold particle (size < 100 nm) is illuminated with a hard X-Ray nanobeam (E=15.25 keV, beam dimensions ≈ 100x100 nm^2) and is reconstructed from its coherent pattern. A resolution of 5 nm is achieved in 600 S exposure time.
→ What is next? By improving the refractive optics in term of image quality and transmission and by otimally matching the lateral coherence length of the incident beam to the aperture of the optic, the resolution could be pushed below 1 nm?

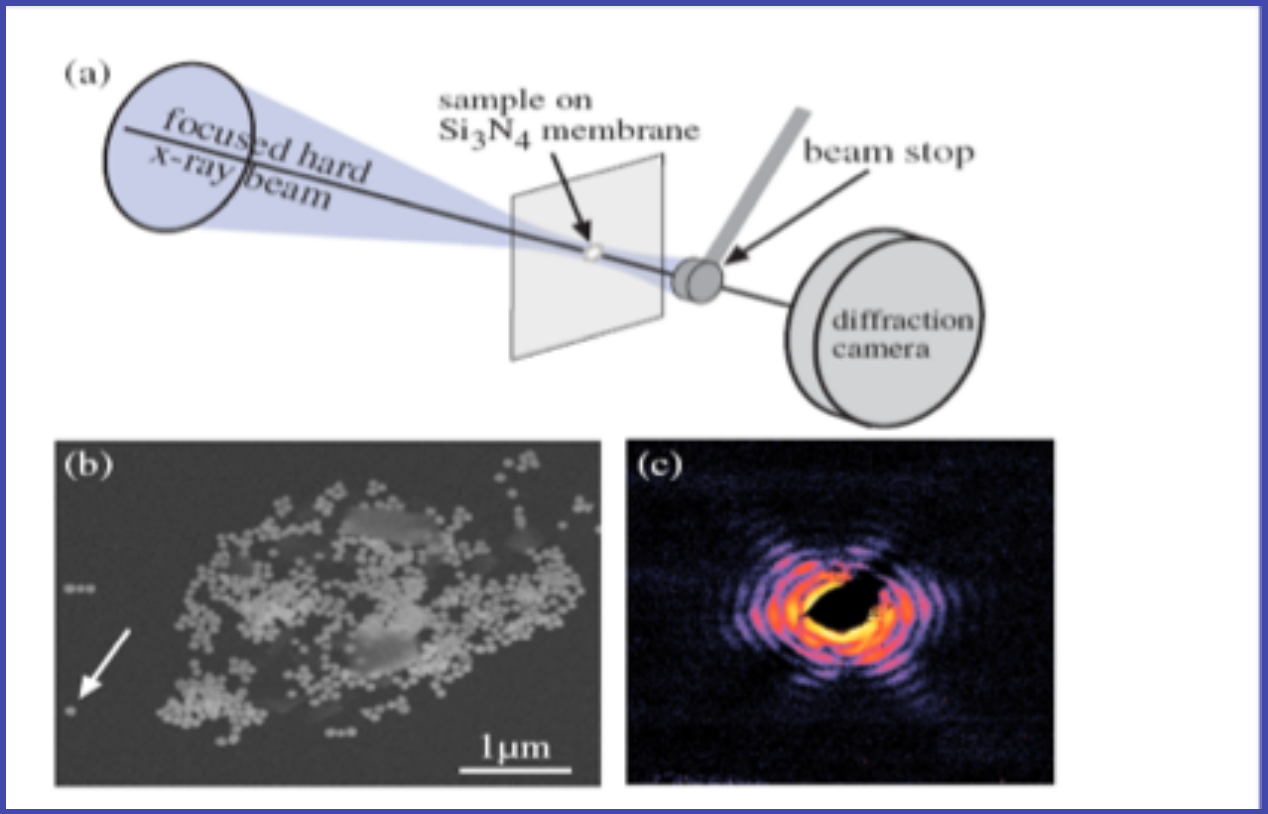

C.G.Schroer et al., PRL101,090801,2009

•Coherent diffractive imaging (CDI), promises to reach diffraction-limited resolution by measuring oversampled diffraction patterns. The need for **isolated objects**, however, prevent a widespread and easy-to-use application of the method. Recently, two approaches have been demonstrated that enable CDI investigation of non isolated objects. [J.Miao, P. Charalambous, J.Kirz and D.Sayre (Nature 400, 342, 1999) , M. A. Pfeifer et al.,(Nature 442, 63, 2006)]

•Ptychography uses multiple diffraction patterns from overlapping sample areas, that are reconstructed jointly by applying a complex iterative phase retrieval algorithm. [P. Thibault et al., [Science 321, 379, 2008]]

•Keyhole CDI uses a single diffraction pattern from a sharply defined, divergent beam to reconstruct a section of an extended object.[B. Abbey et al., [Nature Physics 4, 394, 2008]

• Fourier Transform Holography: much simpler is the image formation process using Fourier transform holography (FTH)-pattern yielding an unambiguous image of the object. As the phases are encoded in the hologram, several numerical contrast enhancing procedures, as e.g., Zernike or Schlieren phase contrast, can be applied to the image. **The spatial resolution in FTH-based methods is limited by the size of the reference aperture-today FTH masks can be routinely produced with reference holes of 30 nm size. However, the image obtained by reverse Fourier transform provides an excellent starting point for a further phase retrieval treatment. In such a way the resolution limitation of FTH can be overcome.** [D. Stickler et al., Applied Physics Letters 96, 042501, 2010]]

4. fs MAGNETISM

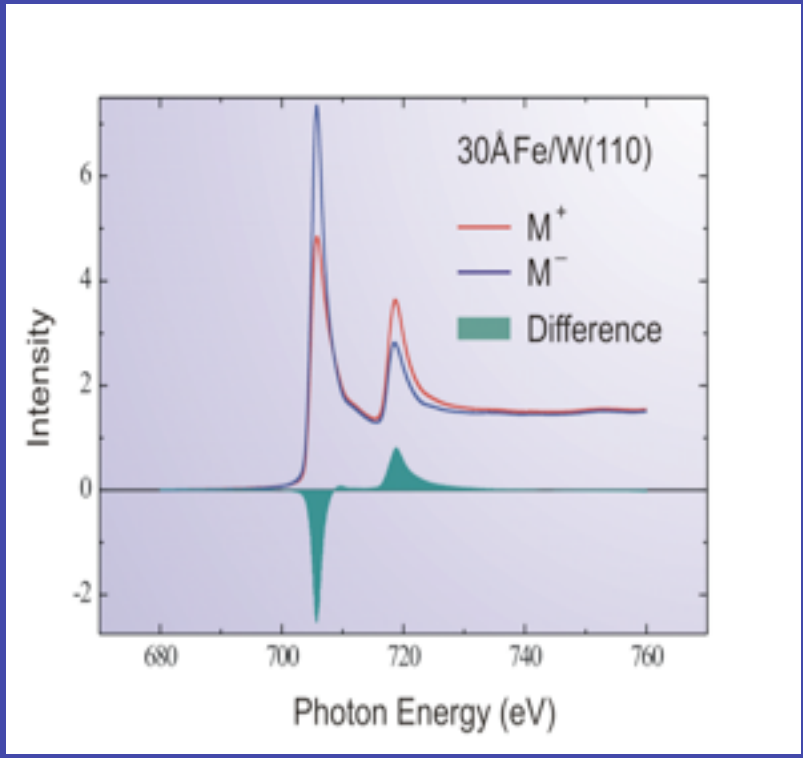

4. fs MAGNETISM

- **X-ray magnetic circular dichroism (XMCD)** is a difference spectrum of two x-ray absorption spectra (XAS) taken in a magnetic field, one taken with left circularly polarized light, and one with right circularly polarized light. By closely analyzing the difference in the XMCD spectrum, information can be obtained on the magnetic properties of the atom, such as its spin and orbital magnetic moment.

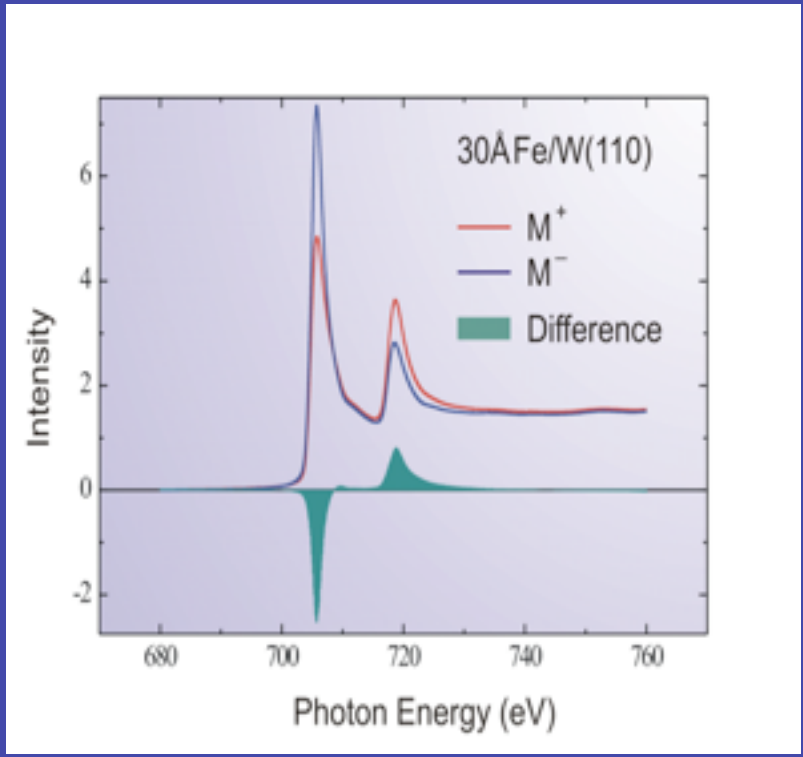

4. fs MAGNETISM

- **X-ray magnetic circular dichroism (XMCD)** is a difference spectrum of two x-ray absorption spectra (XAS) taken in a magnetic field, one taken with left circularly polarized light, and one with right circularly polarized light. By closely analyzing the difference in the XMCD spectrum, information can be obtained on the magnetic properties of the atom, such as its spin and orbital magnetic moment.

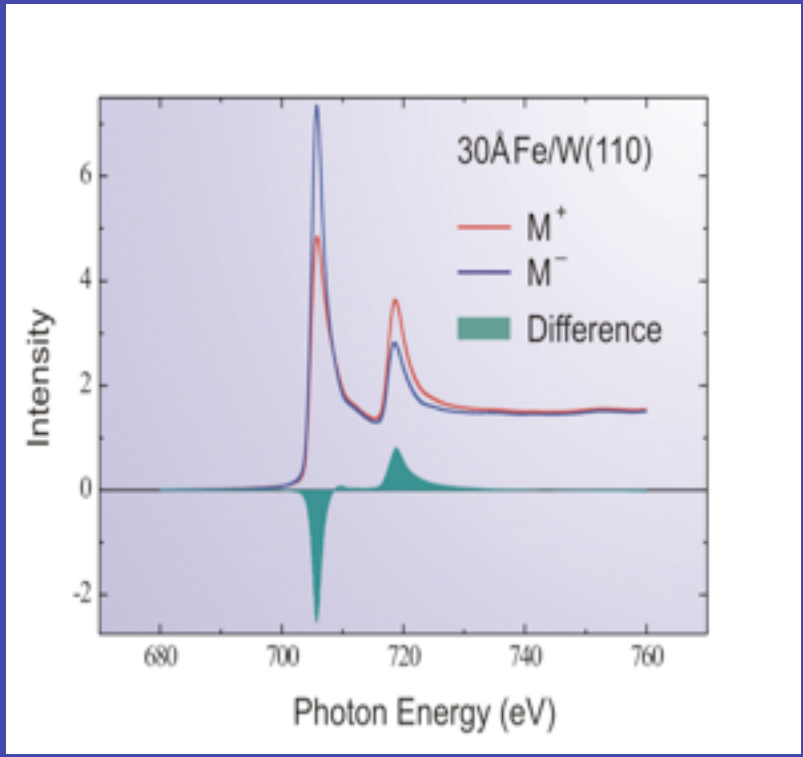

4. fs MAGNETISM

- **X-ray magnetic circular dichroism (XMCD)** is a difference spectrum of two x-ray absorption spectra (XAS) taken in a magnetic field, one taken with left circularly polarized light, and one with right circularly polarized light. By closely analyzing the difference in the XMCD spectrum, information can be obtained on the magnetic properties of the atom, such as its spin and orbital magnetic moment.

- In the case of transition metals such as iron, cobalt, and nickel, the absorption spectra for XMCD are usually measured at the L-edge. This corresponds to the process in the iron case: with iron, a 2p electron is excited to a 3d state by an x-ray of about 700 eV. ***Because the 3d electron states are the origin of the magnetic properties of the elements, the spectra contain information on the magnetic properties***.

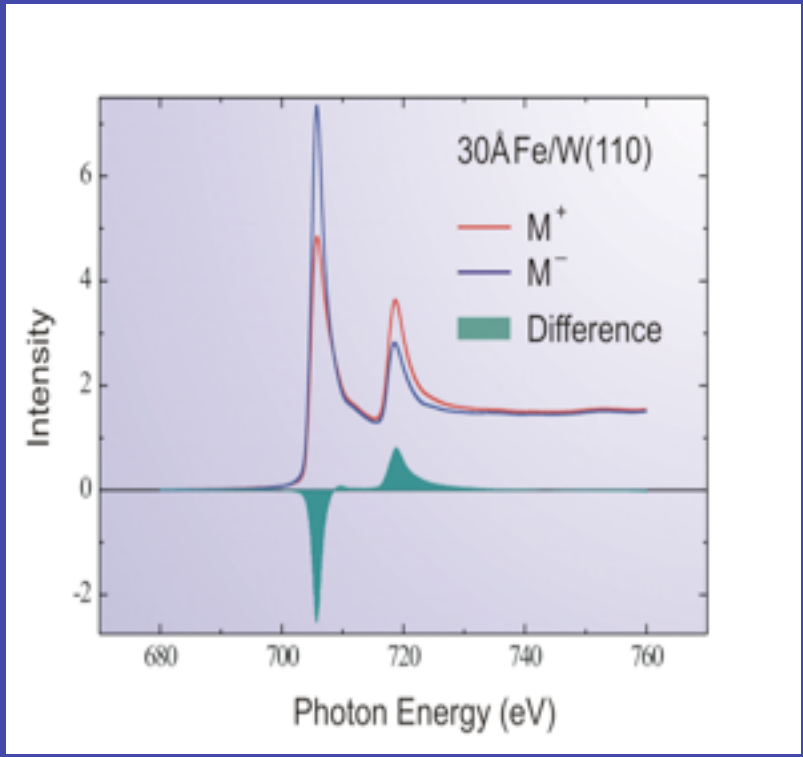

4. fs MAGNETISM

- **X-ray magnetic circular dichroism (XMCD)** is a difference spectrum of two x-ray absorption spectra (XAS) taken in a magnetic field, one taken with left circularly polarized light, and one with right circularly polarized light. By closely analyzing the difference in the XMCD spectrum, information can be obtained on the magnetic properties of the atom, such as its spin and orbital magnetic moment.

- In the case of transition metals such as iron, cobalt, and nickel, the absorption spectra for XMCD are usually measured at the L-edge. This corresponds to the process in the iron case: with iron, a 2p electron is excited to a 3d state by an x-ray of about 700 eV. ***Because the 3d electron states are the origin of the magnetic properties of the elements, the spectra contain information on the magnetic properties***.

- We will see that this allows to measure the spin and the orbital momentum

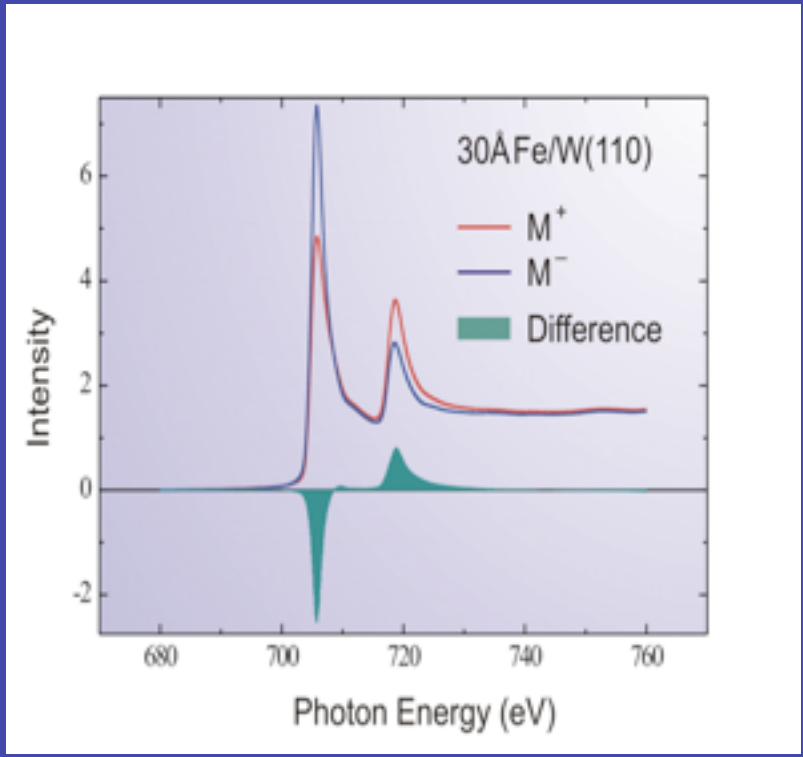

PUERTO VALLARTA

DISTINGUISHING THE ULTRAFAST DYNAMICS OF SPIN AND ORBITAL MOMENT IN SOLIDS.

- For an isolated electron, the orbital (L) and spin (S) magnetic moments can change provided that the total angular momentum of the particle is conserved. In condensed matter, an efficient transfer between L and S can occur owing to the spin–orbit interaction, which originates in the relativistic motion of electrons. Disentangling the absolute contributions of the orbital and spin angular momenta is challenging, however, as any transfer between the two occurs on femtosecond timescales.

DISTINGUISHING THE ULTRAFAST DYNAMICS OF SPIN AND ORBITAL MOMENT IN SOLIDS.

- For an isolated electron, the orbital (L) and spin (S) magnetic moments can change provided that the total angular momentum of the particle is conserved. In condensed matter, an efficient transfer between L and S can occur owing to the spin–orbit interaction, which originates in the relativistic motion of electrons. Disentangling the absolute contributions of the orbital and spin angular momenta is challenging, however, as any transfer between the two occurs on femtosecond timescales.

DISTINGUISHING THE ULTRAFAST DYNAMICS OF SPIN AND ORBITAL MOMENT IN SOLIDS.

- For an isolated electron, the orbital (L) and spin (S) magnetic moments can change provided that the total angular momentum of the particle is conserved. In condensed matter, an efficient transfer between L and S can occur owing to the spin–orbit interaction, which originates in the relativistic motion of electrons. Disentangling the absolute contributions of the orbital and spin angular momenta is challenging, however, as any transfer between the two occurs on femtosecond timescales.

- For electrons, the spin–orbit interaction (SOI) connects their orbital motion to their internal spin degree of freedom. An interesting class of materials where the SOI plays a key role are

DISTINGUISHING THE ULTRAFAST DYNAMICS OF SPIN AND ORBITAL MOMENT IN SOLIDS.

- For an isolated electron, the orbital (L) and spin (S) magnetic moments can change provided that the total angular momentum of the particle is conserved. In condensed matter, an efficient transfer between L and S can occur owing to the spin–orbit interaction, which originates in the relativistic motion of electrons. Disentangling the absolute contributions of the orbital and spin angular momenta is challenging, however, as any transfer between the two occurs on femtosecond timescales.

- For electrons, the spin–orbit interaction (SOI) connects their orbital motion to their internal spin degree of freedom. An interesting class of materials where the SOI plays a key role are ***ferromagnetic films with a magnetization perpendicular to the plane of the film***. Such materials are used for large storage densities in computer hard drives. The perpendicular magnetic anisotropy (PMA) responsible for the spin orientation along the disk normal has to be artificially induced by tailoring spin–orbit coupling in the material.

DISTINGUISHING THE ULTRAFAST DYNAMICS OF SPIN AND ORBITAL MOMENT IN SOLIDS.

- For an isolated electron, the orbital (L) and spin (S) magnetic moments can change provided that the total angular momentum of the particle is conserved. In condensed matter, an efficient transfer between L and S can occur owing to the spin–orbit interaction, which originates in the relativistic motion of electrons. Disentangling the absolute contributions of the orbital and spin angular momenta is challenging, however, as any transfer between the two occurs on femtosecond timescales.

- For electrons, the spin–orbit interaction (SOI) connects their orbital motion to their internal spin degree of freedom. An interesting class of materials where the SOI plays a key role are ***ferromagnetic films with a magnetization perpendicular to the plane of the film***. Such materials are used for large storage densities in computer hard drives. The perpendicular magnetic anisotropy (PMA) responsible for the spin orientation along the disk normal has to be artificially induced by tailoring spin–orbit coupling in the material.

DISTINGUISHING THE ULTRAFAST DYNAMICS OF SPIN AND ORBITAL MOMENT IN SOLIDS.

- For an isolated electron, the orbital (L) and spin (S) magnetic moments can change provided that the total angular momentum of the particle is conserved. In condensed matter, an efficient transfer between L and S can occur owing to the spin–orbit interaction, which originates in the relativistic motion of electrons. Disentangling the absolute contributions of the orbital and spin angular momenta is challenging, however, as any transfer between the two occurs on femtosecond timescales.

- For electrons, the spin–orbit interaction (SOI) connects their orbital motion to their internal spin degree of freedom. An interesting class of materials where the SOI plays a key role are ***ferromagnetic films with a magnetization perpendicular to the plane of the film***. Such materials are used for large storage densities in computer hard drives. The perpendicular magnetic anisotropy (PMA) responsible for the spin orientation along the disk normal has to be artificially induced by tailoring spin–orbit coupling in the material.

- How to do that? By electronic hybridization of 3d transition metal valence levels (for example, of Fe or Co carrying large magnetic moments but relatively small spin–orbit coupling) with valence levels of 4d, 5d transition metals (for example, of Pd or Pt) with small magnetic moments but a large spin–orbit coupling. A layered sample structure can then induce a preferential spin orientation perpendicular to the layers. At the microscopic level, the change in ground state energy due to orienting the spin moment **S** is given by $E_{PMA}=-\xi$ **L.S**, where ξ is the spin–orbit coupling parameter.

DISTINGUISHING THE ULTRAFAST DYNAMICS OF SPIN AND ORBITAL MOMENT IN SOLIDS.

- For an isolated electron, the orbital (L) and spin (S) magnetic moments can change provided that the total angular momentum of the particle is conserved. In condensed matter, an efficient transfer between L and S can occur owing to the spin–orbit interaction, which originates in the relativistic motion of electrons. Disentangling the absolute contributions of the orbital and spin angular momenta is challenging, however, as any transfer between the two occurs on femtosecond timescales.

- For electrons, the spin–orbit interaction (SOI) connects their orbital motion to their internal spin degree of freedom. An interesting class of materials where the SOI plays a key role are ***ferromagnetic films with a magnetization perpendicular to the plane of the film***. Such materials are used for large storage densities in computer hard drives. The perpendicular magnetic anisotropy (PMA) responsible for the spin orientation along the disk normal has to be artificially induced by tailoring spin–orbit coupling in the material.

- How to do that? By electronic hybridization of 3d transition metal valence levels (for example, of Fe or Co carrying large magnetic moments but relatively small spin–orbit coupling) with valence levels of 4d, 5d transition metals (for example, of Pd or Pt) with small magnetic moments but a large spin–orbit coupling. A layered sample structure can then induce a preferential spin orientation perpendicular to the layers. At the microscopic level, the change in ground state energy due to orienting the spin moment **S** is given by $E_{PMA}=-\xi$ **L.S**, where ξ is the spin–orbit coupling parameter.

DISTINGUISHING THE ULTRAFAST DYNAMICS OF SPIN AND ORBITAL MOMENT IN SOLIDS.

- For an isolated electron, the orbital (L) and spin (S) magnetic moments can change provided that the total angular momentum of the particle is conserved. In condensed matter, an efficient transfer between L and S can occur owing to the spin–orbit interaction, which originates in the relativistic motion of electrons. Disentangling the absolute contributions of the orbital and spin angular momenta is challenging, however, as any transfer between the two occurs on femtosecond timescales.

- For electrons, the spin–orbit interaction (SOI) connects their orbital motion to their internal spin degree of freedom. An interesting class of materials where the SOI plays a key role are ***ferromagnetic films with a magnetization perpendicular to the plane of the film***. Such materials are used for large storage densities in computer hard drives. The perpendicular magnetic anisotropy (PMA) responsible for the spin orientation along the disk normal has to be artificially induced by tailoring spin–orbit coupling in the material.

- How to do that? By electronic hybridization of 3d transition metal valence levels (for example, of Fe or Co carrying large magnetic moments but relatively small spin–orbit coupling) with valence levels of 4d, 5d transition metals (for example, of Pd or Pt) with small magnetic moments but a large spin–orbit coupling. A layered sample structure can then induce a preferential spin orientation perpendicular to the layers. At the microscopic level, the change in ground state energy due to orienting the spin moment **S** is given by $E_{PMA}=-\xi$ **L.S**, where ξ is the spin–orbit coupling parameter.

- As the orbital and spin angular momentum can vary separately providing that the total angular momentum is conserved, a fundamental question is then: how do the orbital and spin magnetic moments change after an ultrafast laser excitation? On such ultrashort timescales (t,1 ps), the way the electronic subsystem may exchange angular momentum is still debated.

Boeglin, Beaurepaire, Halté, Lopes-Flores, Stamm, Pontius, Dürr&Bigot [NATURE 465, 458, 2010] have shown that this exchange indeed takes place during the thermalization time of the spins and charges. Moreover, a detailed analysis suggests that the orbital moment changes faster than its spin counterpart. They provide experimental evidence that ultrafast quenching of the PMA occurs.

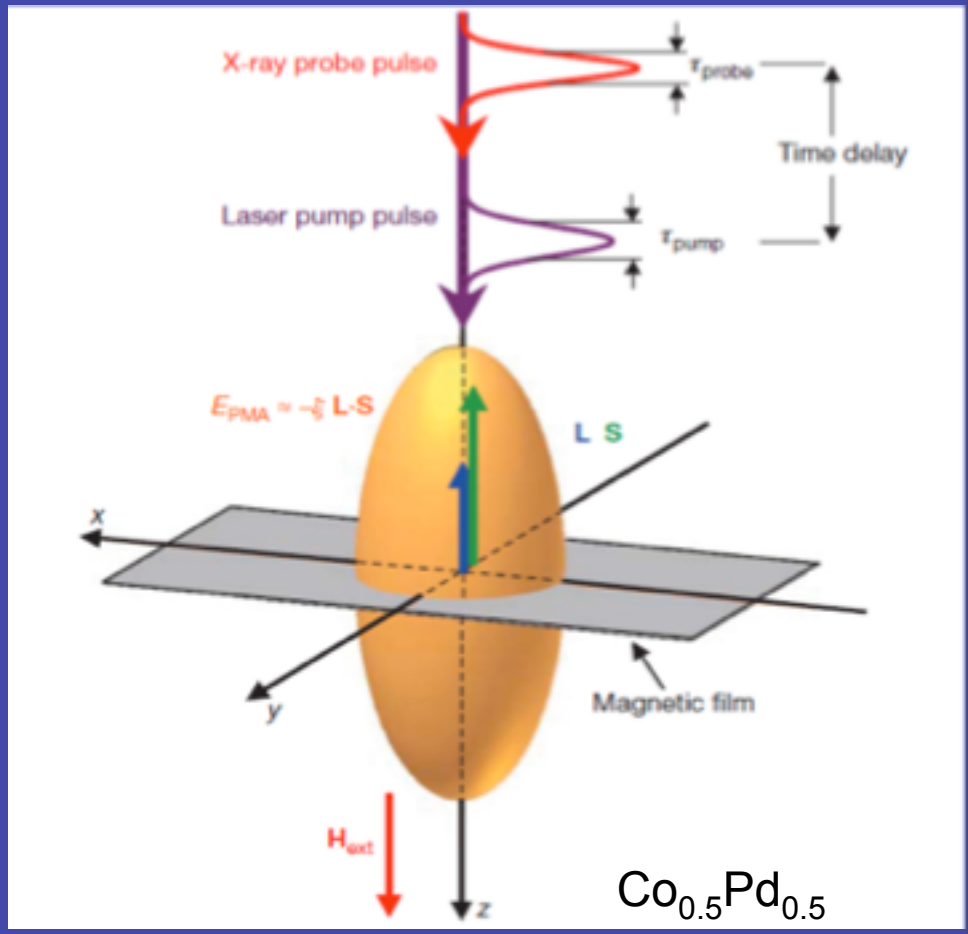

Boeglin, Beaurepaire, Halté, Lopes-Flores, Stamm, Pontius, Dürr&Bigot [NATURE 465, 458, 2010] have shown that this exchange indeed takes place during the thermalization time of the spins and charges. Moreover, a detailed analysis suggests that the orbital moment changes faster than its spin counterpart. They provide experimental evidence that ultrafast quenching of the PMA occurs.

- Geometry of the pump–probe experiment at the femtoslicing synchrotron beam line at BESSY. Time resolved XMCD allows measurement of the ultrafast dynamics of spin and orbital momenta along the quantification axis z parallel to the applied magnetic field.

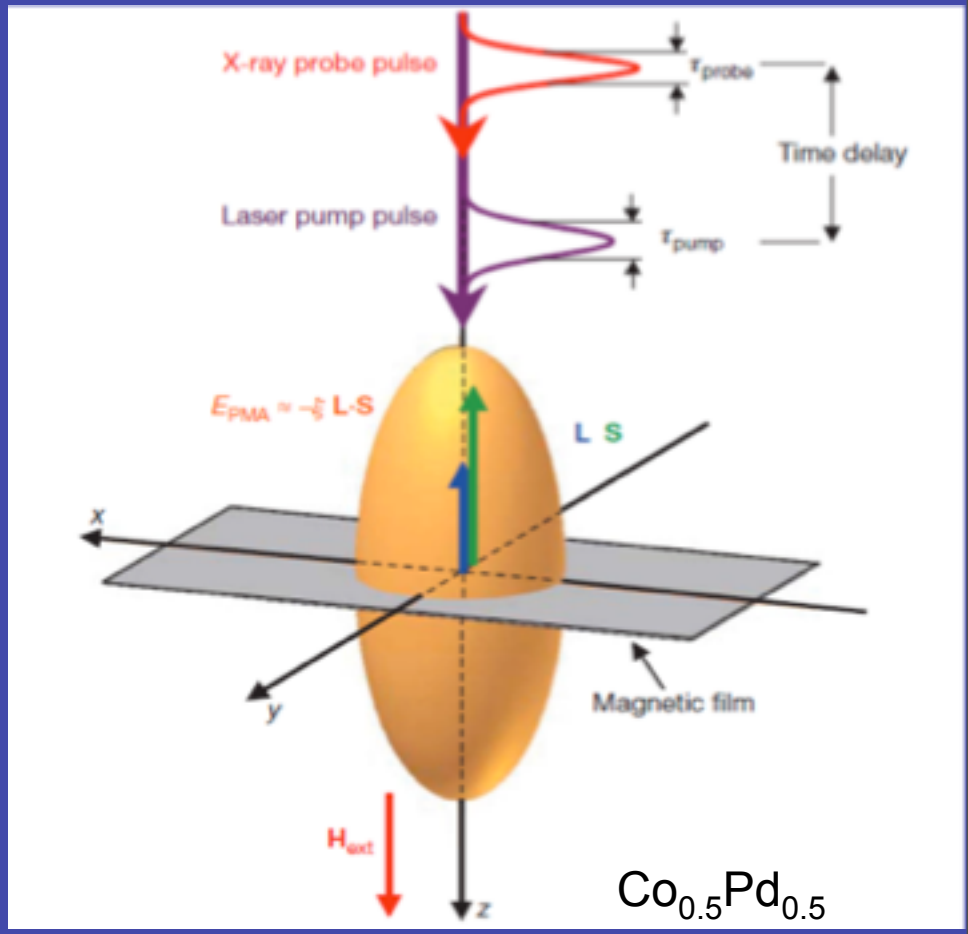

Boeglin, Beaurepaire, Halté, Lopes-Flores, Stamm, Pontius, Dürr&Bigot [NATURE 465, 458, 2010] have shown that this exchange indeed takes place during the thermalization time of the spins and charges. Moreover, a detailed analysis suggests that the orbital moment changes faster than its spin counterpart. They provide experimental evidence that ultrafast quenching of the PMA occurs.

- Geometry of the pump–probe experiment at the femtoslicing synchrotron beam line at BESSY. Time resolved XMCD allows measurement of the ultrafast dynamics of spin and orbital momenta along the quantification axis z parallel to the applied magnetic field.

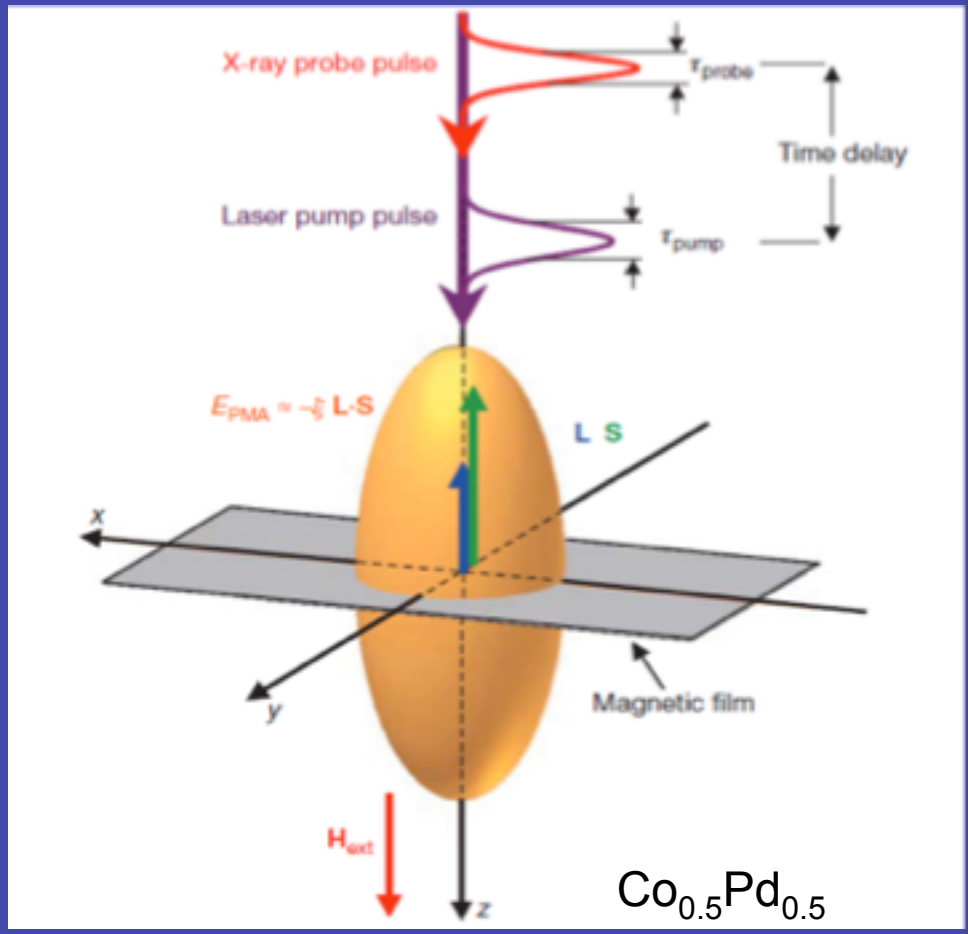

Boeglin, Beaurepaire, Halté, Lopes-Flores, Stamm, Pontius, Dürr&Bigot [NATURE 465, 458, 2010] have shown that this exchange indeed takes place during the thermalization time of the spins and charges. Moreover, a detailed analysis suggests that the orbital moment changes faster than its spin counterpart. They provide experimental evidence that ultrafast quenching of the PMA occurs.

- Geometry of the pump–probe experiment at the femtoslicing synchrotron beam line at BESSY. Time resolved XMCD allows measurement of the ultrafast dynamics of spin and orbital momenta along the quantification axis z parallel to the applied magnetic field.

- Optical pulses with a central wavelength of λ_{pump}= 579 nm and a duration of τ_{pump}=60±20 fs excite the ferromagnetic films perpendicularly, aligning the electric vector **E** in the film plane. The density of absorbed laser energy is E_{abs}=12 mJ cm^{-2}.

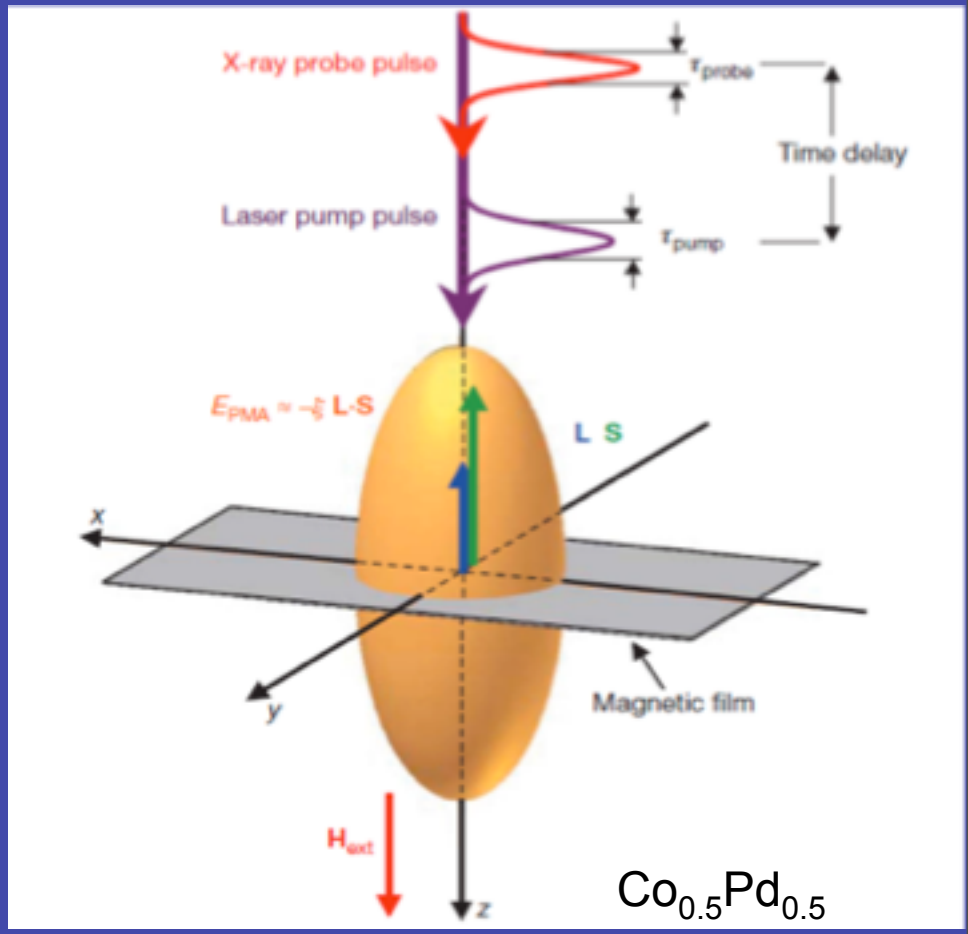

Boeglin, Beaurepaire, Halté, Lopes-Flores, Stamm, Pontius, Dürr&Bigot [NATURE 465, 458, 2010] have shown that this exchange indeed takes place during the thermalization time of the spins and charges. Moreover, a detailed analysis suggests that the orbital moment changes faster than its spin counterpart. They provide experimental evidence that ultrafast quenching of the PMA occurs.

- Geometry of the pump–probe experiment at the femtoslicing synchrotron beam line at BESSY. Time resolved XMCD allows measurement of the ultrafast dynamics of spin and orbital momenta along the quantification axis z parallel to the applied magnetic field.

- Optical pulses with a central wavelength of λ_{pump}= 579 nm and a duration of τ_{pump}=60±20 fs excite the ferromagnetic films perpendicularly, aligning the electric vector **E** in the film plane. The density of absorbed laser energy is E_{abs}=12 mJ cm^{-2}.

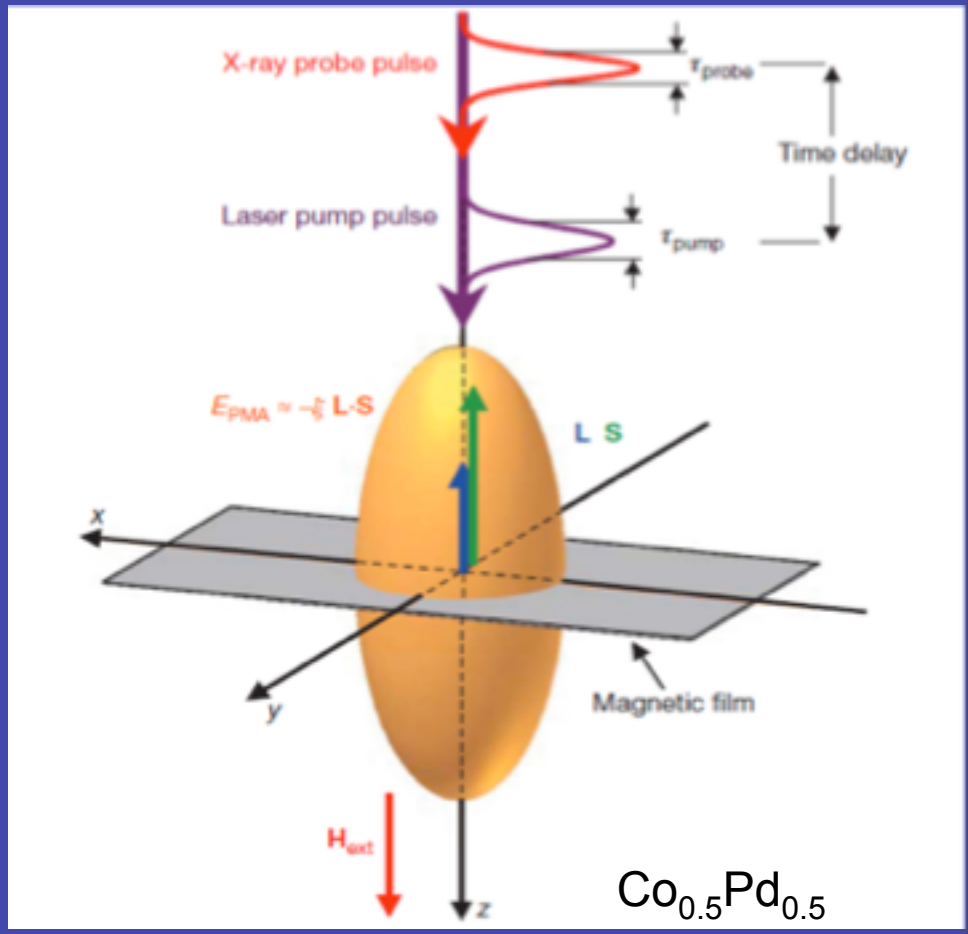

Boeglin, Beaurepaire, Halté, Lopes-Flores, Stamm, Pontius, Dürr&Bigot [NATURE 465, 458, 2010] have shown that this exchange indeed takes place during the thermalization time of the spins and charges. Moreover, a detailed analysis suggests that the orbital moment changes faster than its spin counterpart. They provide experimental evidence that ultrafast quenching of the PMA occurs.

- Geometry of the pump–probe experiment at the femtoslicing synchrotron beam line at BESSY. Time resolved XMCD allows measurement of the ultrafast dynamics of spin and orbital momenta along the quantification axis z parallel to the applied magnetic field.

- Optical pulses with a central wavelength of λ_{pump}= 579 nm and a duration of τ_{pump}=60±20 fs excite the ferromagnetic films perpendicularly, aligning the electric vector **E** in the film plane. The density of absorbed laser energy is E_{abs}=12 mJ cm^{-2}.

- The ellipsoidal shape of $-E_{PMA}$ illustrates the perpendicular anisotropy of the film. The easy magnetization direction is defined by the largest value of the z-axis projected value of L, (Lz). On applying the external magnetic field $\mathbf{H}_{ext}$, the spin magnetic moment **S** aligns parallel to the orbital magnetic moment **L** along the z axis. A variable

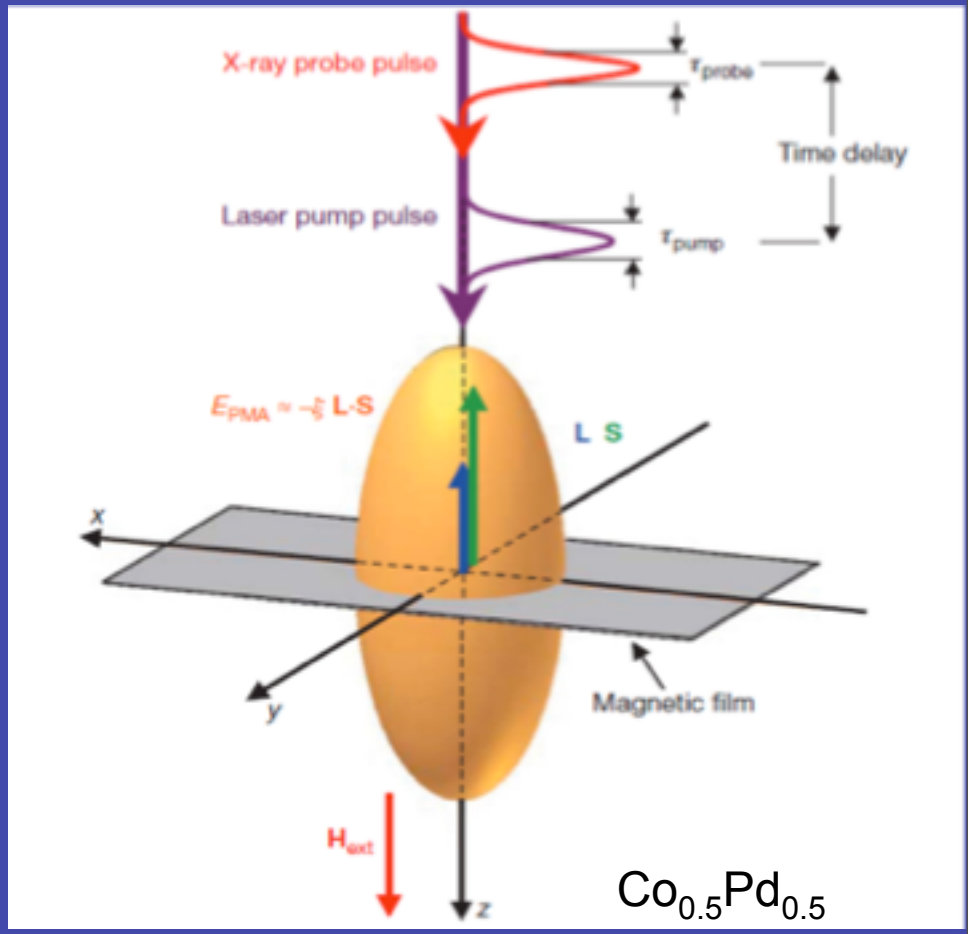

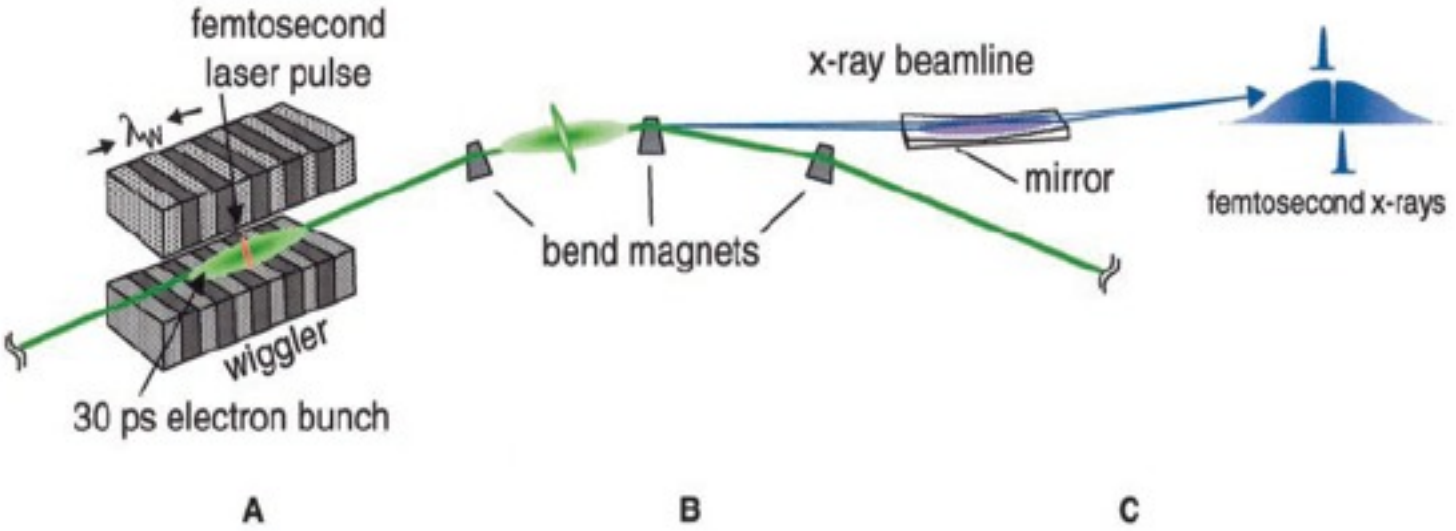

Fig. 1. Schematic of the laser slicing method for generating femtosecond synchrotron pulses. (A) Laser interaction with electron bunch in a resonantly tuned wiggler. (B) Transverse separation of modulated electrons in dispersive bend of the storage ring. (C) Separation of femtosecond synchrotron radiation at the beamline image plane.

Zholents et al, ALS, Berkeley

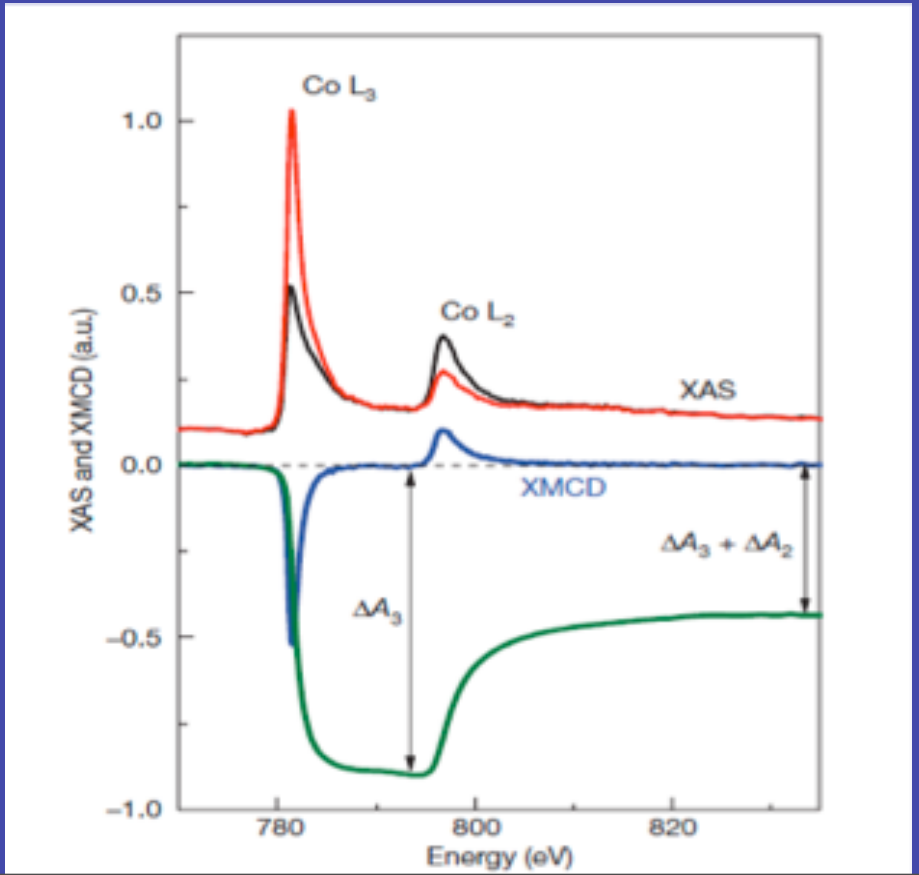

PUERTO VALLARTA

● A typical XMCD spectrum, that is, the difference in X-ray absorption with the sample magnetization oriented parallel and antiparallel to the incident X-ray direction, is shown in the next figure. The XMCD signals, $\Delta A_{2,3}$, integrated over the respective $L_{2,3}$ absorption edges are related to the spin and orbital momentum components via sum rules:

$$S_z = -(7/2)T_z - (\Delta A_3 - 2\Delta A_2)C$$
$$L_z = -(\Delta A_3 + \Delta A_2)C$$

- C is a constant related to the number of unoccupied 3d states that can be determined from the X-ray absorption spectra measured with linearly polarized radiation.

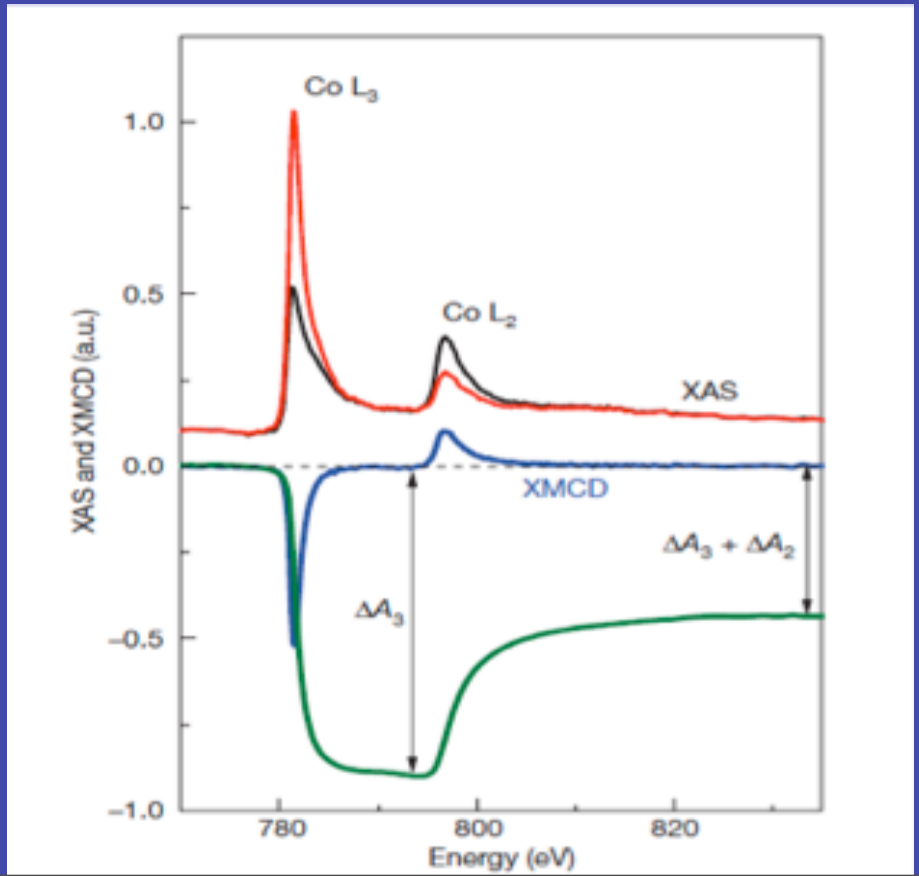

● A typical XMCD spectrum, that is, the difference in X-ray absorption with the sample magnetization oriented parallel and antiparallel to the incident X-ray direction, is shown in the next figure. The XMCD signals, $\Delta A_{2,3}$, integrated over the respective $L_{2,3}$ absorption edges are related to the spin and orbital momentum components via sum rules:

$$S_z = -(7/2)T_z - (\Delta A_3 - 2\Delta A_2)C$$
$$L_z = -(\Delta A_3 + \Delta A_2)C$$

- C is a constant related to the number of unoccupied 3d states that can be determined from the X-ray absorption spectra measured with linearly polarized radiation.
- The so-called magnetic dipole term T_z is usually less than 10% of the S_z value and is neglected.

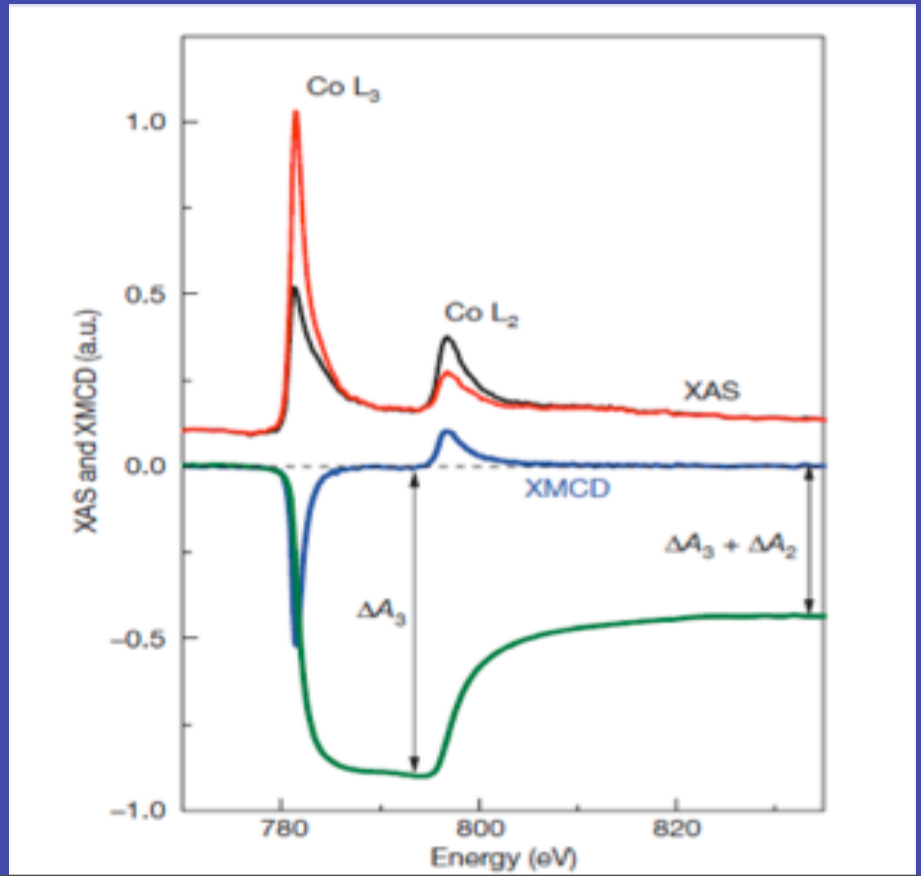

● A typical XMCD spectrum, that is, the difference in X-ray absorption with the sample magnetization oriented parallel and antiparallel to the incident X-ray direction, is shown in the next figure. The XMCD signals, $\Delta A_{2,3}$, integrated over the respective $L_{2,3}$ absorption edges are related to the spin and orbital momentum components via sum rules:

$$S_z = -(7/2)T_z - (\Delta A_3 - 2\Delta A_2)C$$
$$L_z = -(\Delta A_3 + \Delta A_2)C$$

- C is a constant related to the number of unoccupied 3d states that can be determined from the X-ray absorption spectra measured with linearly polarized radiation.
- The so-called magnetic dipole term T_z is usually less than 10% of the S_z value and is neglected.

●Static energy resolved X-ray absorption spectra of CoPd film using circularly polarized light. Two XAS spectra (red and black) and the normalized difference spectrum XMCD (line in blue) at the Co $L_{2,3}$ edges are displayed for the 15-nm $Co_{0.5}Pd_{0.5}$ film in normal incidence geometry with a magnetic field of ± 4 kOe, collinear with the incident circularly polarized X-rays.

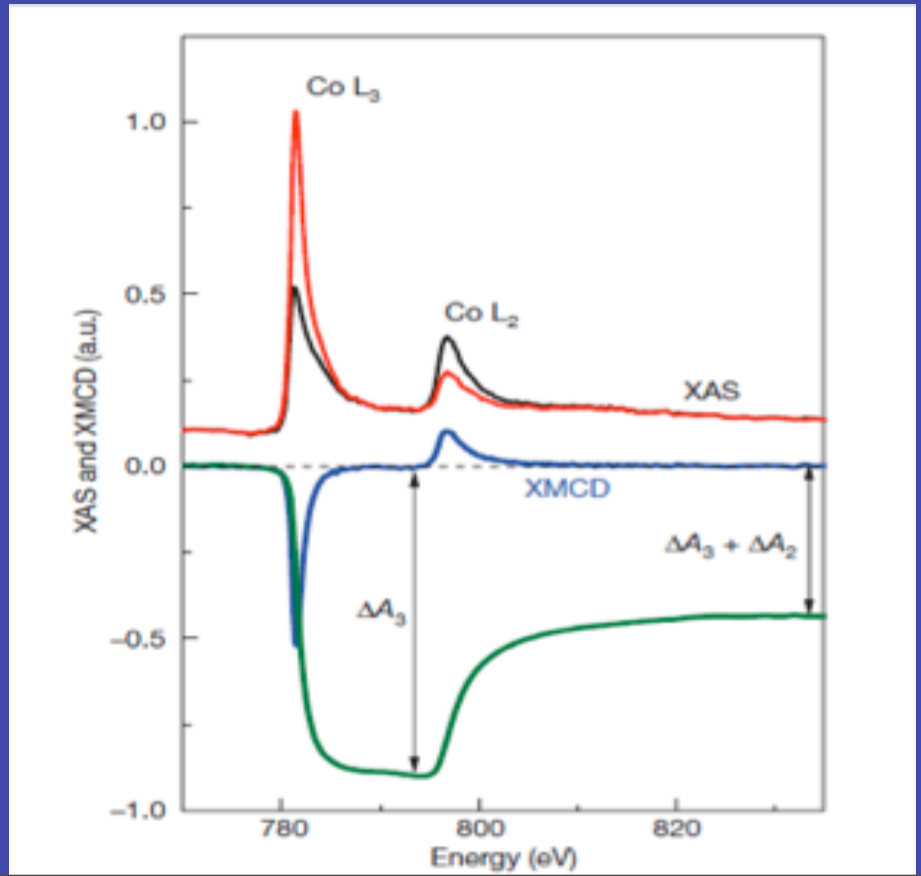

● A typical XMCD spectrum, that is, the difference in X-ray absorption with the sample magnetization oriented parallel and antiparallel to the incident X-ray direction, is shown in the next figure. The XMCD signals, $\Delta A_{2,3}$, integrated over the respective $L_{2,3}$ absorption edges are related to the spin and orbital momentum components via sum rules:

$$S_z = -(7/2)T_z - (\Delta A_3 - 2\Delta A_2)C$$
$$L_z = -(\Delta A_3 + \Delta A_2)C$$

- C is a constant related to the number of unoccupied 3d states that can be determined from the X-ray absorption spectra measured with linearly polarized radiation.
- The so-called magnetic dipole term T_z is usually less than 10% of the S_z value and is neglected.

●Static energy resolved X-ray absorption spectra of CoPd film using circularly polarized light. Two XAS spectra (red and black) and the normalized difference spectrum XMCD (line in blue) at the Co $L_{2,3}$ edges are displayed for the 15-nm $Co_{0.5}Pd_{0.5}$ film in normal incidence geometry with a magnetic field of ± 4 kOe, collinear with the incident circularly polarized X-rays.

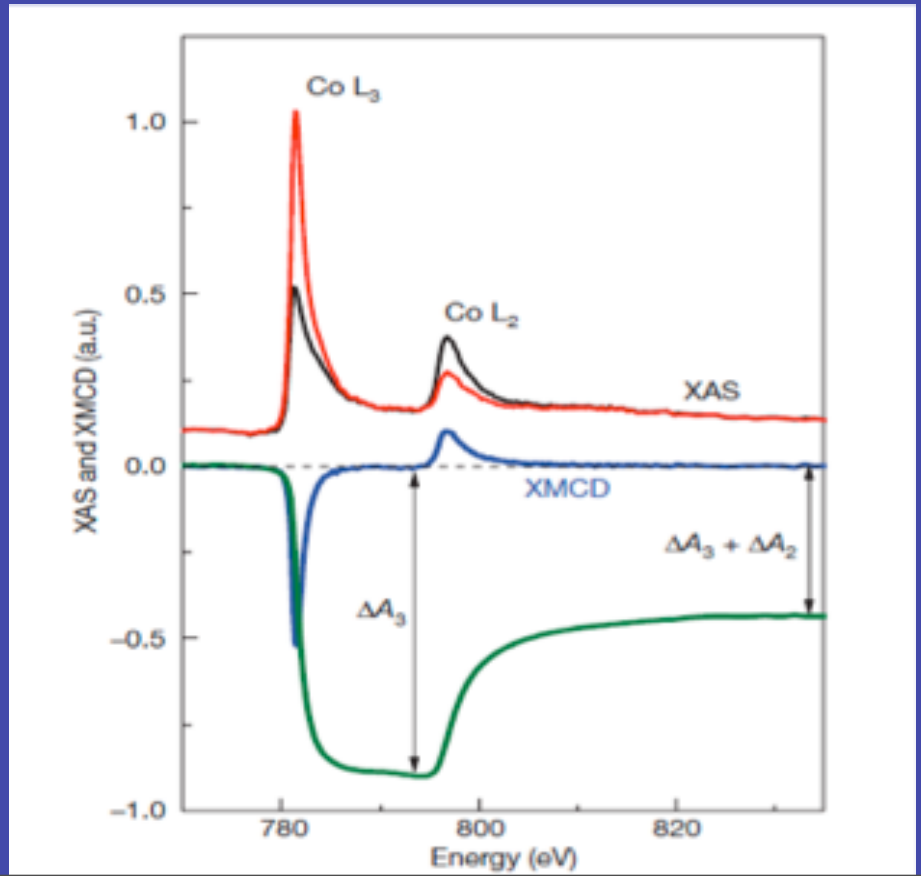

● Integration of the energy resolved XMCD spectrum (green curve) allows a quantitative determination of the static values (without pump) of the spin and

● A typical XMCD spectrum, that is, the difference in X-ray absorption with the sample magnetization oriented parallel and antiparallel to the incident X-ray direction, is shown in the next figure. The XMCD signals, $\Delta A_{2,3}$, integrated over the respective $L_{2,3}$ absorption edges are related to the spin and orbital momentum components via sum rules:

$$S_z = -(7/2)T_z - (\Delta A_3 - 2\Delta A_2)C$$
$$L_z = -(\Delta A_3 + \Delta A_2)C$$

- C is a constant related to the number of unoccupied 3d states that can be determined from the X-ray absorption spectra measured with linearly polarized radiation.
- The so-called magnetic dipole term T_z is usually less than 10% of the S_z value and is neglected.

●Static energy resolved X-ray absorption spectra of CoPd film using circularly polarized light. Two XAS spectra (red and black) and the normalized difference spectrum XMCD (line in blue) at the Co $L_{2,3}$ edges are displayed for the 15-nm $Co_{0.5}Pd_{0.5}$ film in normal incidence geometry with a magnetic field of ± 4 kOe, collinear with the incident circularly polarized X-rays.

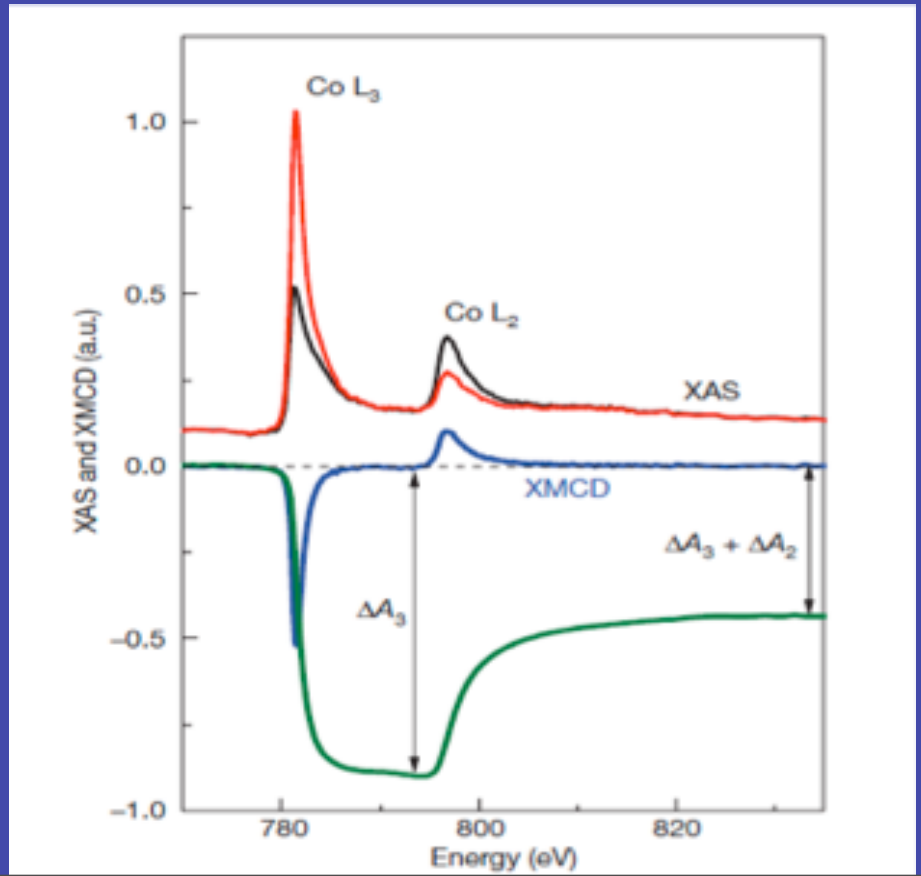

● Integration of the energy resolved XMCD spectrum (green curve) allows a quantitative determination of the static values (without pump) of the spin and orbital magnetic moments at t<0:

Femtosecond evolution of the magnetic spin and orbital

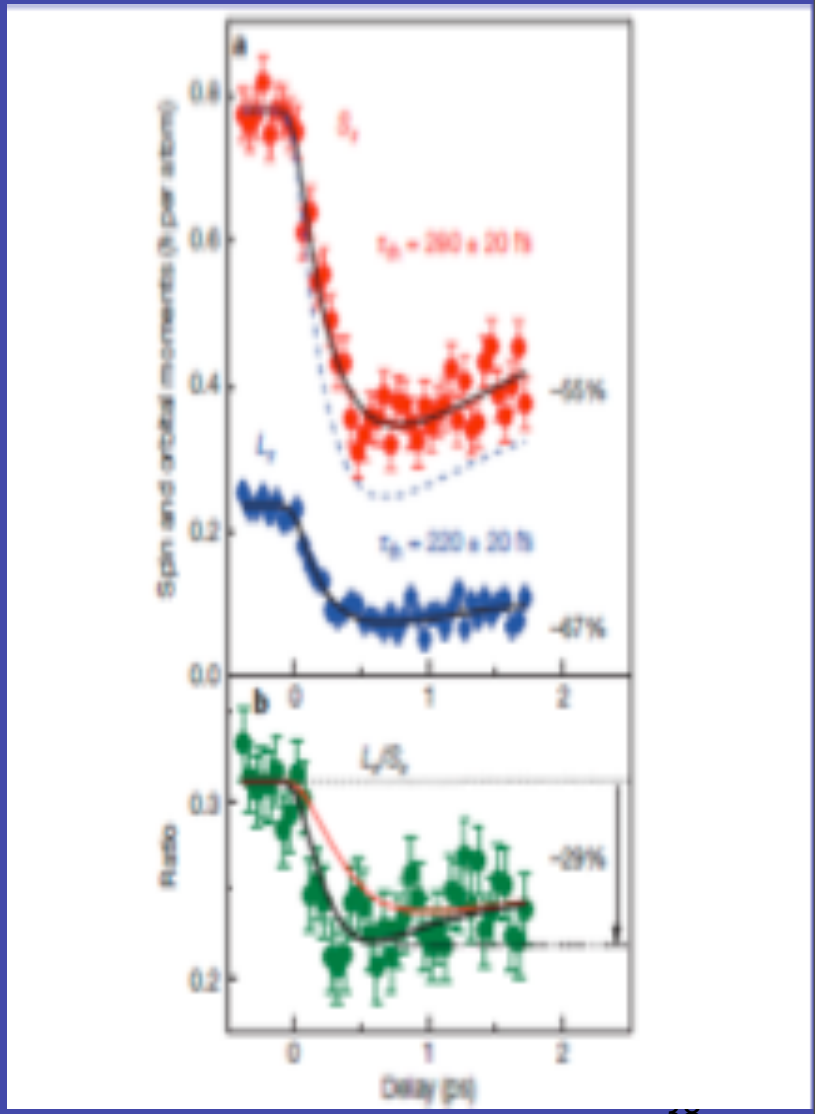

Femtosecond evolution of the magnetic spin and orbital

a, Sum rule extracted effective spin and orbital magnetic moments $S_z(t)$ and $L_z(t)$ as a function of the delay time between the laser pump and the X-ray probe. The continuous lines are fits obtained by using a 130-fs FWHM Gaussian function accounting for the time resolution of the experiment (including the X-ray probe and the fs laser pump).The blue dashed line represents the fit to $L_z(t)$ scaled to the value of $S_z(t)$ before laser excitation.

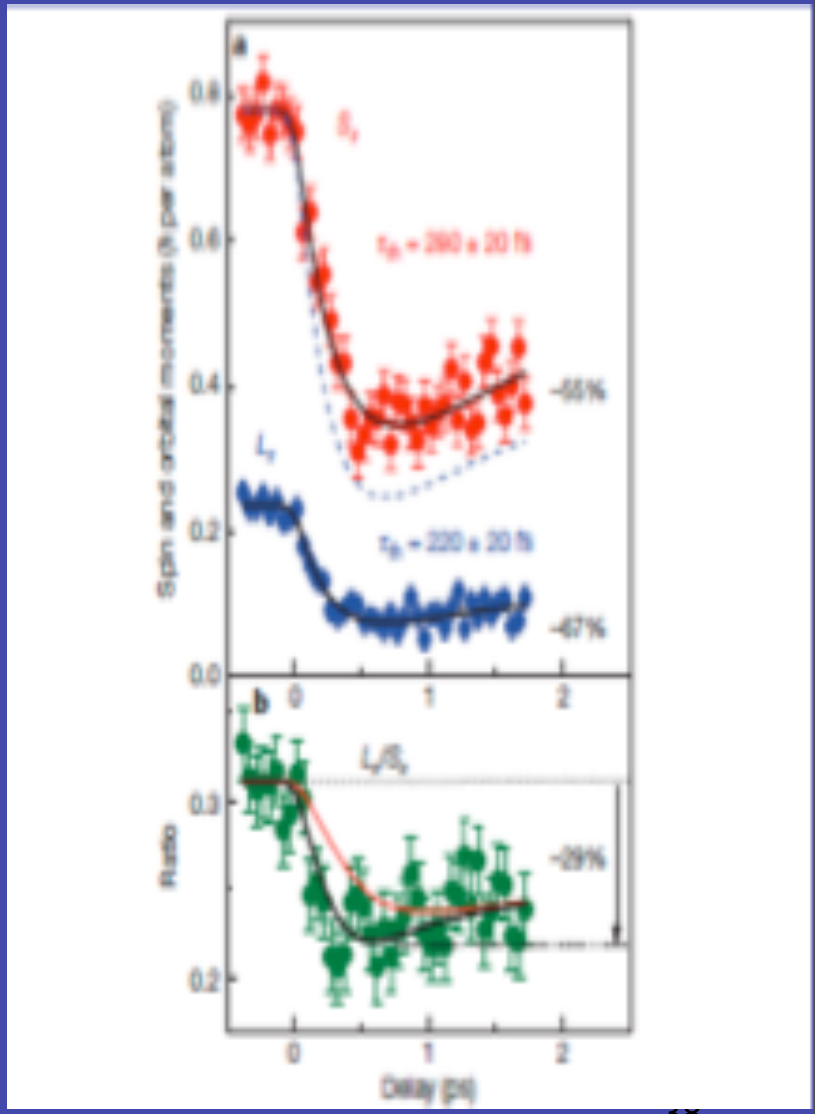

Femtosecond evolution of the magnetic spin and orbital

a, Sum rule extracted effective spin and orbital magnetic moments $S_z(t)$ and $L_z(t)$ as a function of the delay time between the laser pump and the X-ray probe. The continuous lines are fits obtained by using a 130-fs FWHM Gaussian function accounting for the time resolution of the experiment (including the X-ray probe and the fs laser pump).The blue dashed line represents the fit to $L_z(t)$ scaled to the value of $S_z(t)$ before laser excitation.

For both $L_z(t)$ and $S_z(t)$ two main temporal components are observed:

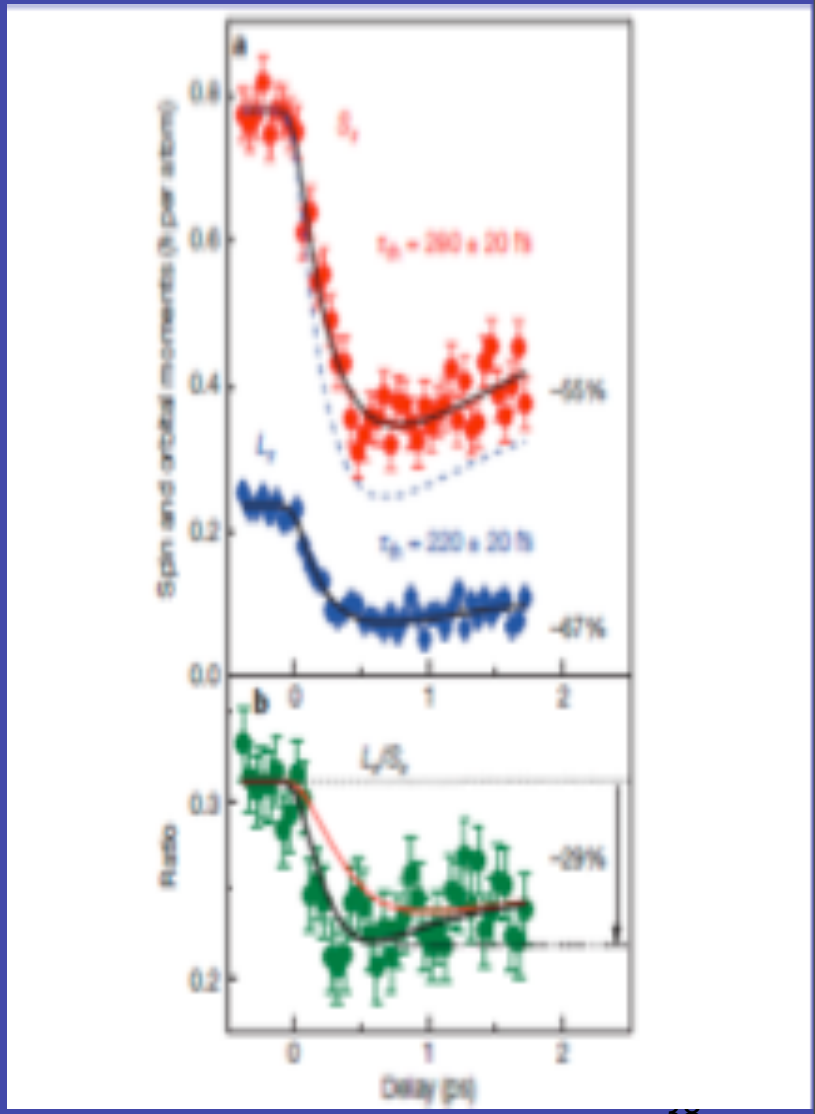

Femtosecond evolution of the magnetic spin and orbital

a, Sum rule extracted effective spin and orbital magnetic moments $S_z(t)$ and $L_z(t)$ as a function of the delay time between the laser pump and the X-ray probe. The continuous lines are fits obtained by using a 130-fs FWHM Gaussian function accounting for the time resolution of the experiment (including the X-ray probe and the fs laser pump).The blue dashed line represents the fit to $L_z(t)$ scaled to the value of $S_z(t)$ before laser excitation.

For both $L_z(t)$ and $S_z(t)$ two main temporal components are observed:

- the first→demagnetization of the film induced by the laser pulse with $\tau_{th}(L_z)$=220±20 fs and $\tau_{th}(S_z)$=280 ±20fs.

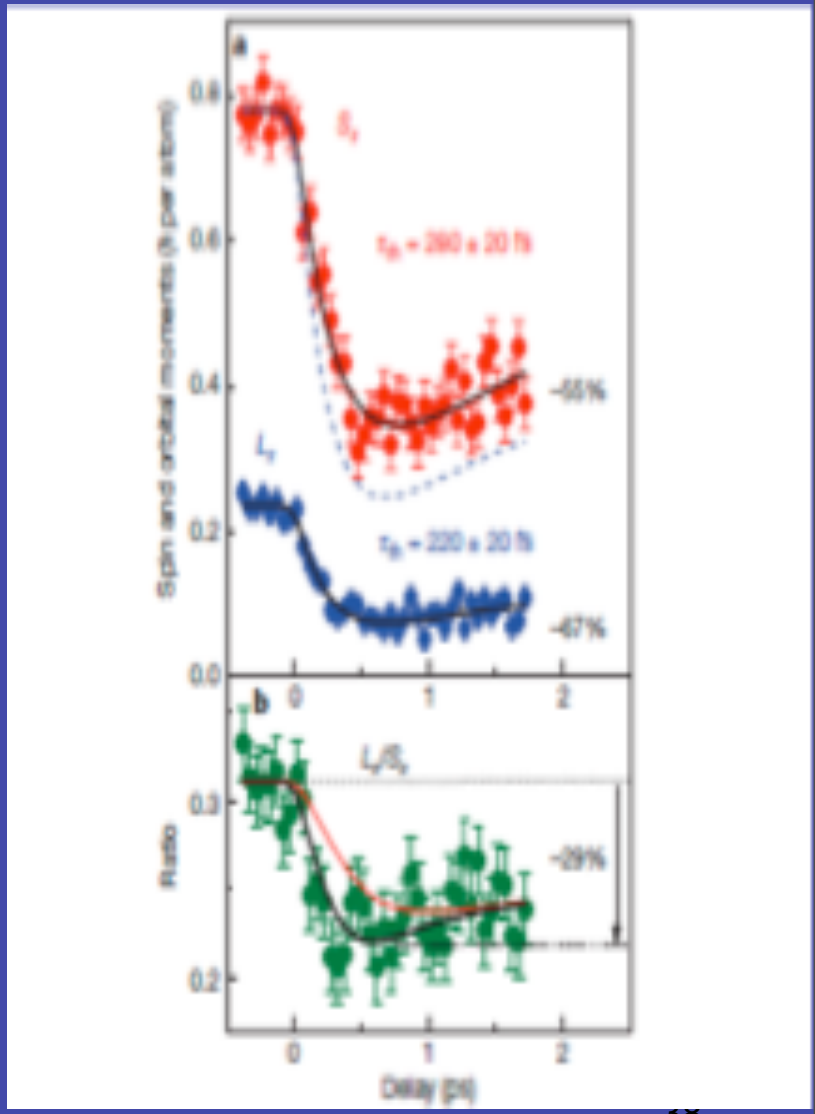

Femtosecond evolution of the magnetic spin and orbital

a, Sum rule extracted effective spin and orbital magnetic moments $S_z(t)$ and $L_z(t)$ as a function of the delay time between the laser pump and the X-ray probe. The continuous lines are fits obtained by using a 130-fs FWHM Gaussian function accounting for the time resolution of the experiment (including the X-ray probe and the fs laser pump).The blue dashed line represents the fit to $L_z(t)$ scaled to the value of $S_z(t)$ before laser excitation.

For both $L_z(t)$ and $S_z(t)$ two main temporal components are observed:

- the first→demagnetization of the film induced by the laser pulse with $\tau_{th}(L_z)$=220±20 fs and $\tau_{th}(S_z)$=280 ±20fs.

- the second component → slow remagnetization, corresponding to a cooling of the spins attributed to the spin-phonon interaction with $\tau_{s\text{-}ph}$=8±2ps

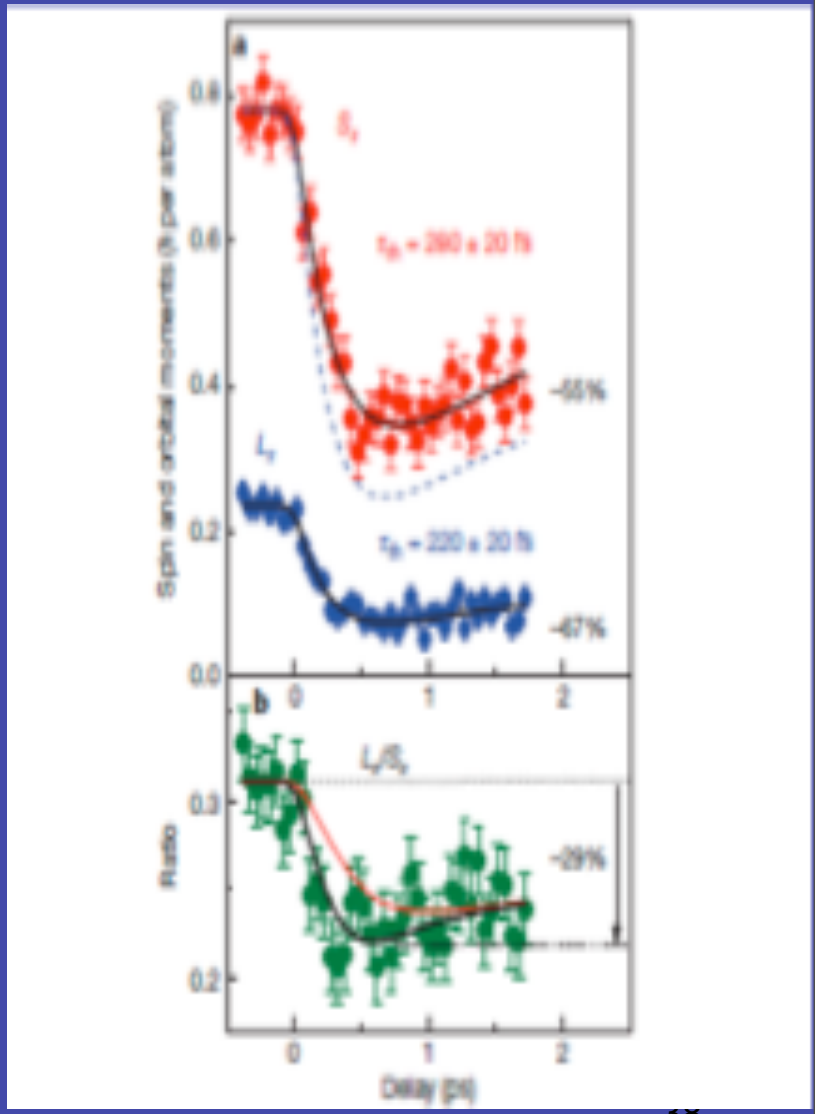

Femtosecond evolution of the magnetic spin and orbital

a, Sum rule extracted effective spin and orbital magnetic moments $S_z(t)$ and $L_z(t)$ as a function of the delay time between the laser pump and the X-ray probe. The continuous lines are fits obtained by using a 130-fs FWHM Gaussian function accounting for the time resolution of the experiment (including the X-ray probe and the fs laser pump).The blue dashed line represents the fit to $L_z(t)$ scaled to the value of $S_z(t)$ before laser excitation.

For both $L_z(t)$ and $S_z(t)$ two main temporal components are observed:

- the first→demagnetization of the film induced by the laser pulse with $\tau_{th}(L_z)$=220±20 fs and $\tau_{th}(S_z)$=280 ±20fs.

- the second component → slow remagnetization, corresponding to a cooling of the spins attributed to the spin-phonon interaction with $\tau_{s\text{-}ph}$=8±2ps

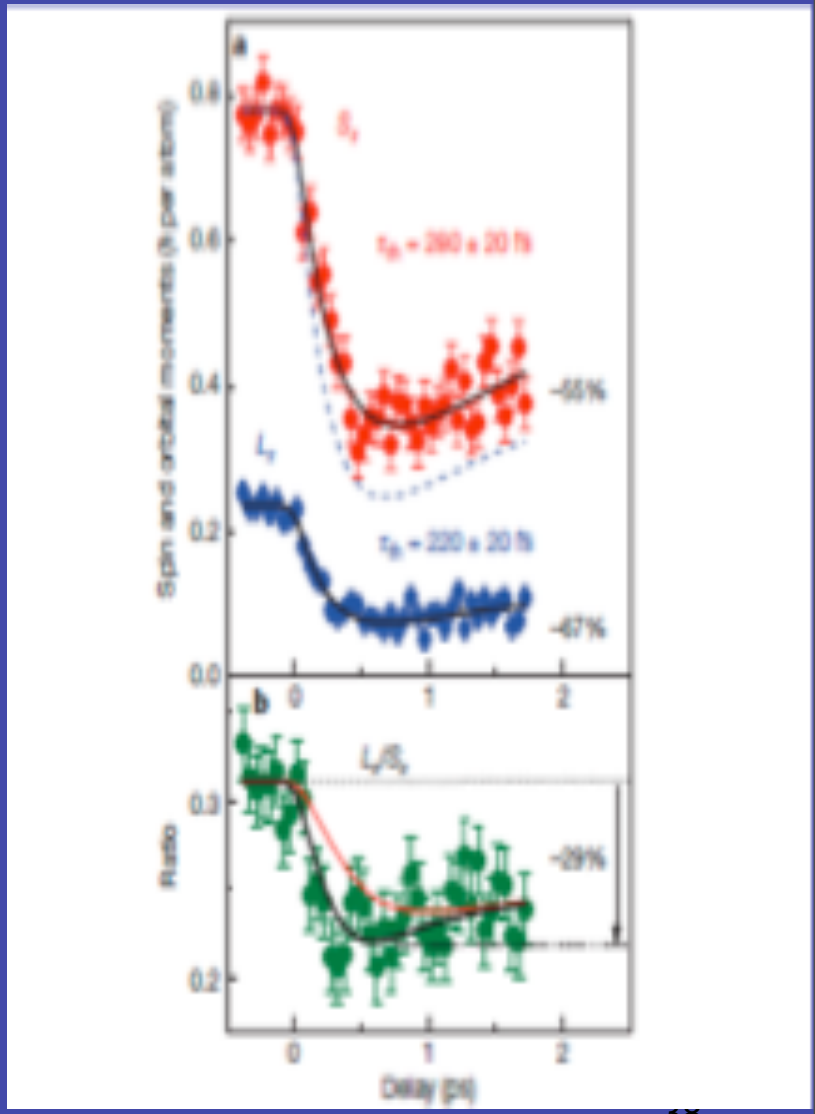

Femtosecond evolution of the magnetic spin and orbital

a, Sum rule extracted effective spin and orbital magnetic moments $S_z(t)$ and $L_z(t)$ as a function of the delay time between the laser pump and the X-ray probe. The continuous lines are fits obtained by using a 130-fs FWHM Gaussian function accounting for the time resolution of the experiment (including the X-ray probe and the fs laser pump).The blue dashed line represents the fit to $L_z(t)$ scaled to the value of $S_z(t)$ before laser excitation.

For both $L_z(t)$ and $S_z(t)$ two main temporal components are observed:

- the first→demagnetization of the film induced by the laser pulse with $\tau_{th}(L_z)$=220±20 fs and $\tau_{th}(S_z)$=280 ±20fs.

- the second component → slow remagnetization, corresponding to a cooling of the spins attributed to the spin-phonon interaction with $\tau_{s\text{-}ph}$=8±2ps

b, The ratio $(L_z/S_z)(t)$ obtained as a function of the delay time shows that the orbital magnetic moment reduces more than the effective spin magnetic moment during the ultra fast demagnetization process. The black continuous line is the ratio between the two simulations of $L_z(t)$ and $S_z(t)$, showing a relative variation of –29±5%. The red line is the ratio obtained when we take two identical values $\tau_{th}(L_z)$= τ_{th} (S_z)=260 fs. The error bars for $L_z(t)$, $S_z(t)$ and $(L_z/S_z)(t)$ are obtained from the error bars of the time resolved XMCD at the Co L_2 and Co L_3 edges.

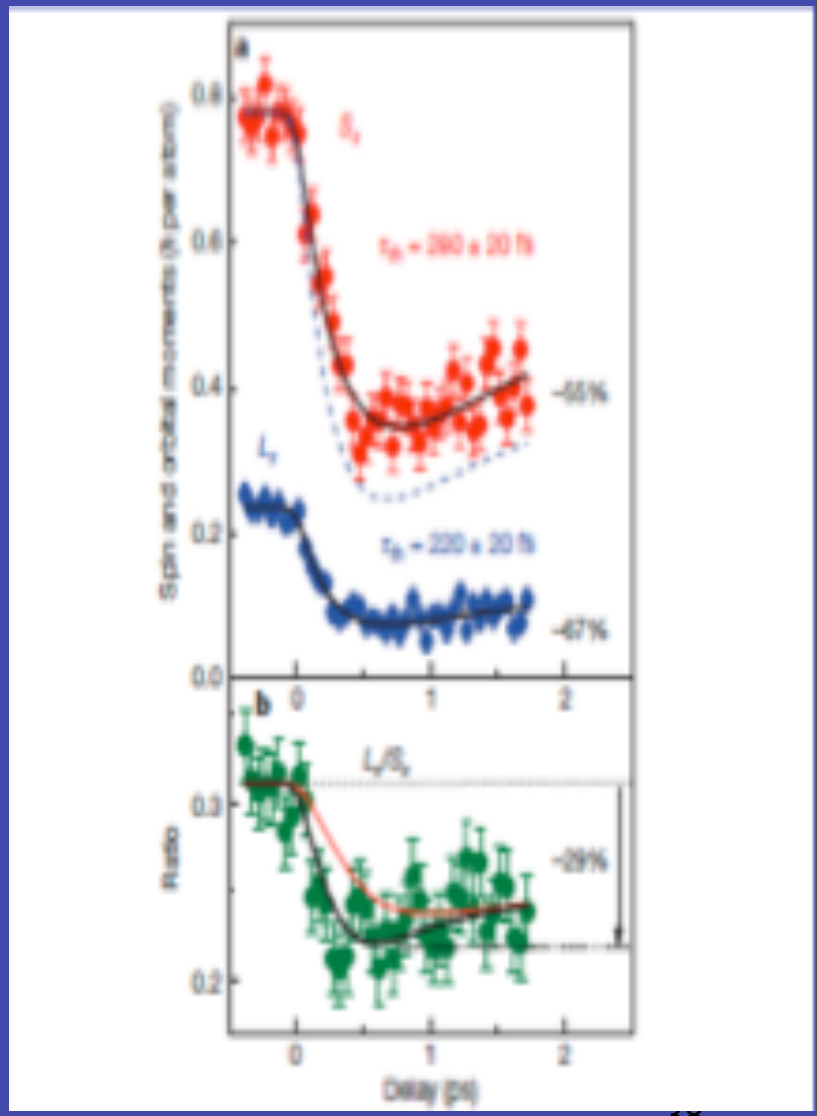

CONCLUSIONS

- These measurements enable to disentagle the spin and orbital components of the magnetic moment, revealing different dynamics for L and S
- They highlight the important role played by the spin-orbit interaction in the ultrafast laser-induced demagnetization of ferromagnetic films.
- They show that the magneto crystalline anisotropy energy is an important quantity to consider in such processes.

5.GRAPHENE

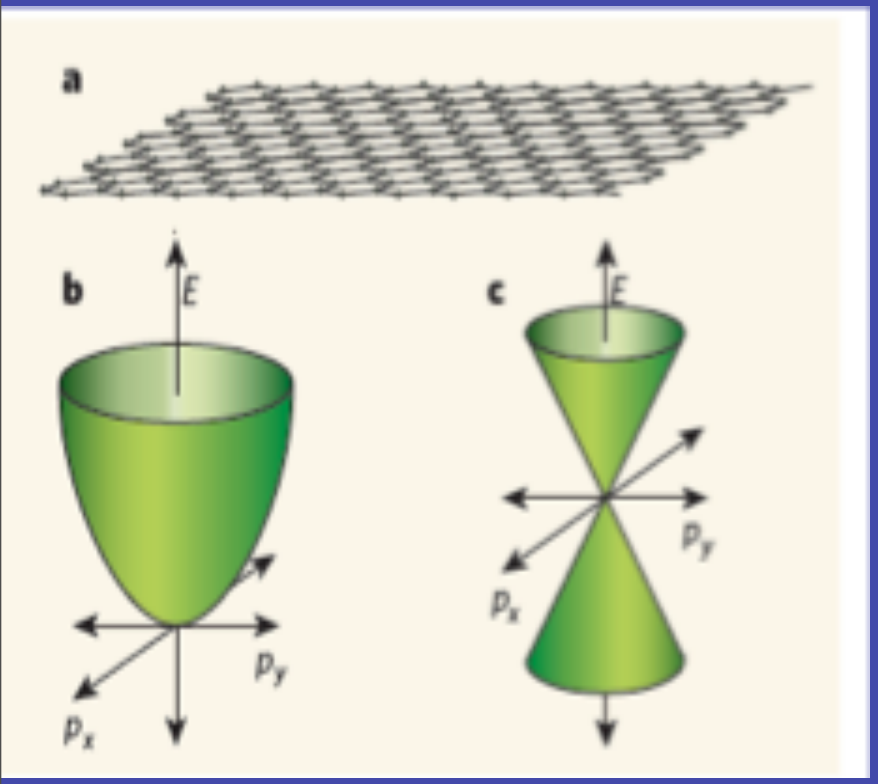

a, The honeycomb lattice pattern of graphene explains its strength and good conductivity. Each carbon atom (green dot) uses three of its outer valence electrons to form strong covalent bonds, leaving one left over that is available for conduction.

b, The quadratic, newtonian energy–momentum relation, $E=p^2/2m^*$ *(E, energy; p, momentum; m*, reduced mass) is obeyed by electrons in* a semiconductor.

c, The energy–momentum relation of electrons in graphene is quite different, $E=v|p|$ *(v is the electron velocity),* allowing them to be modelled as massless, relativistic particles according to the Dirac formulation of quantum mechanics

GRAPHENE BILAYER: TUNABLE BANDGAP

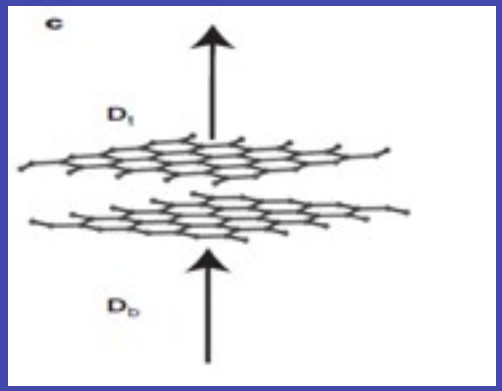

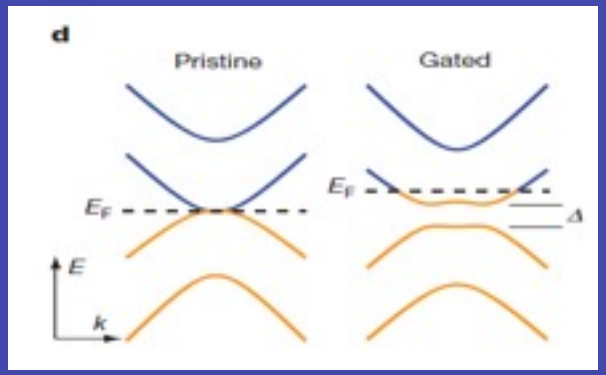

GRAPHENE BILAYER: TUNABLE BANDGAP

The electronic structure near the E_F of an AB-stacked graphene bilayer features two nearly parallel conduction bands above two nearly parallel valence bands. In the absence of gating, the lowest conduction band and highest valence band touch each other with a zero bandgap. Upon electrical gating, the top and bottom electrical displacement fields D_t and D_b (Fig. 1c) produce two effects(Fig. 1d):

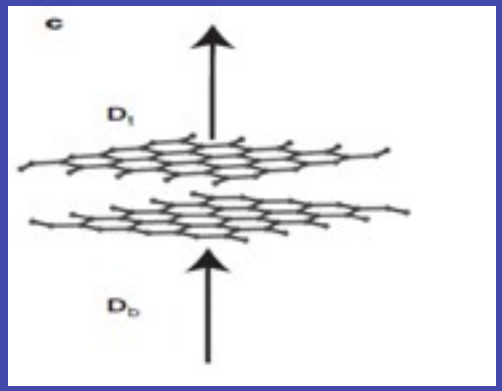

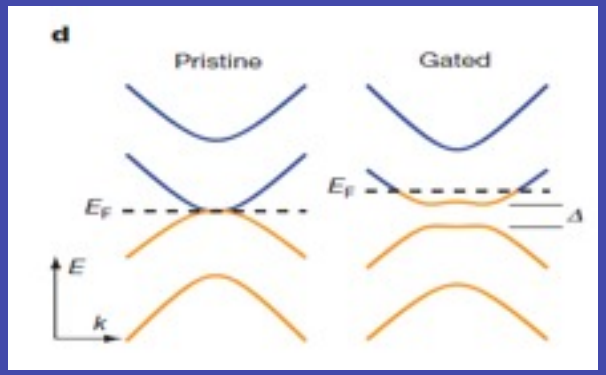

- The difference of the two, $\delta D = D_b - D_t \rightarrow$ net carrier doping(a shift of (E_F).
- The average of the two, $\check{D} = (D_b + D_t)/2$, breaks the inversion symmetry of the bilayer and generates a non-zero bandgap.

GRAPHENE BILAYER: TUNABLE BANDGAP

The electronic structure near the E_F of an AB-stacked graphene bilayer features two nearly parallel conduction bands above two nearly parallel valence bands. In the absence of gating, the lowest conduction band and highest valence band touch each other with a zero bandgap. Upon electrical gating, the top and bottom electrical displacement fields D_t and D_b (Fig. 1c) produce two effects(Fig. 1d):

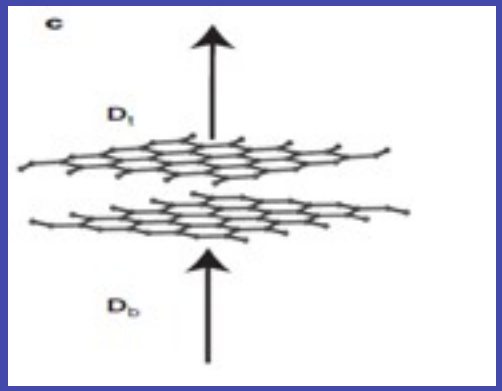

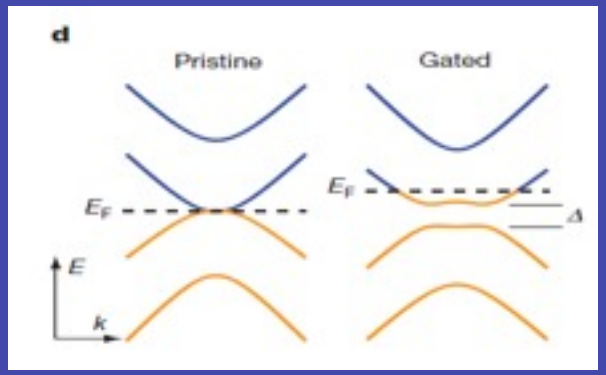

- The difference of the two, $\delta D=D_b-D_t \rightarrow$ net carrier doping(a shift of (E_F).
- The average of the two, $\check{D} =(D_b+D_t)/2$, breaks the inversion symmetry of the bilayer and generates a non-zero bandgap.

By setting δD to zero and varying $\check{D}$, one can tune the bandgap while keeping the bilayer charge neutral. Sets of D_b and D_t leading to δD=0 define the bilayer charge neutral points' (CNPs). By varying δD above or below zero, we can inject electrons or holes into the bilayer and shift the Fermi level without changing the bandgap.

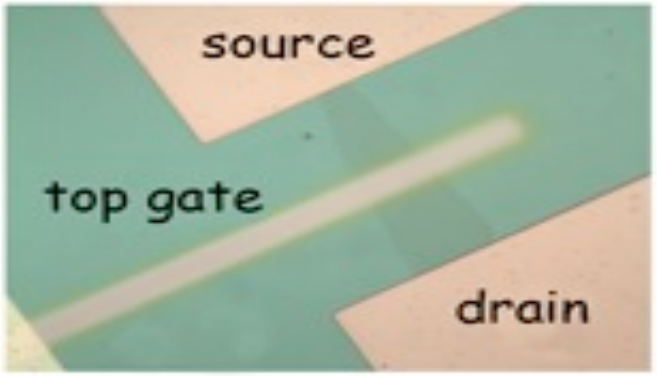

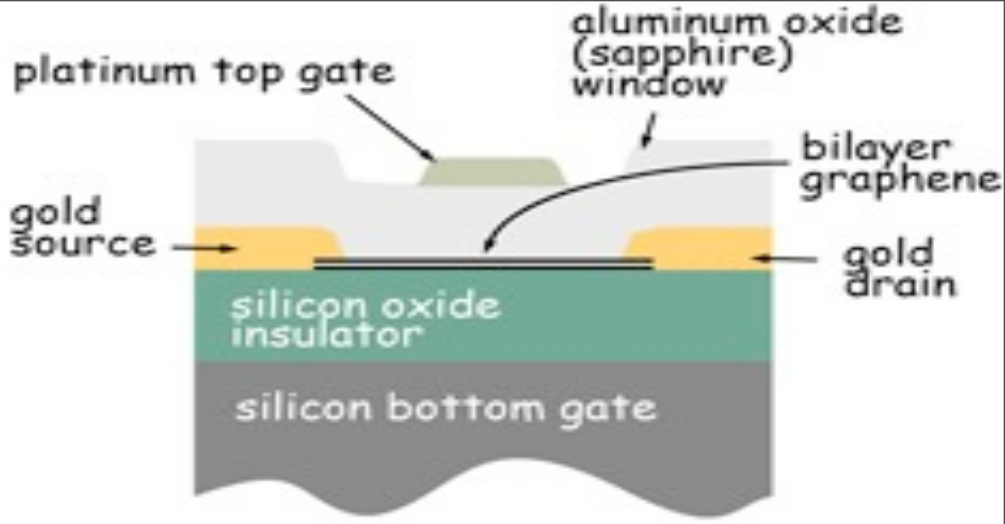

PUERTO VALLARTA

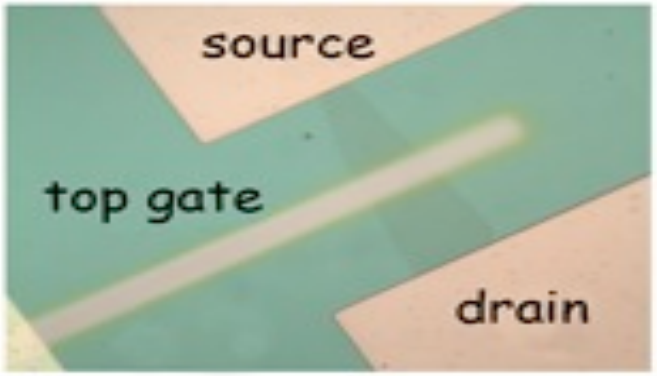

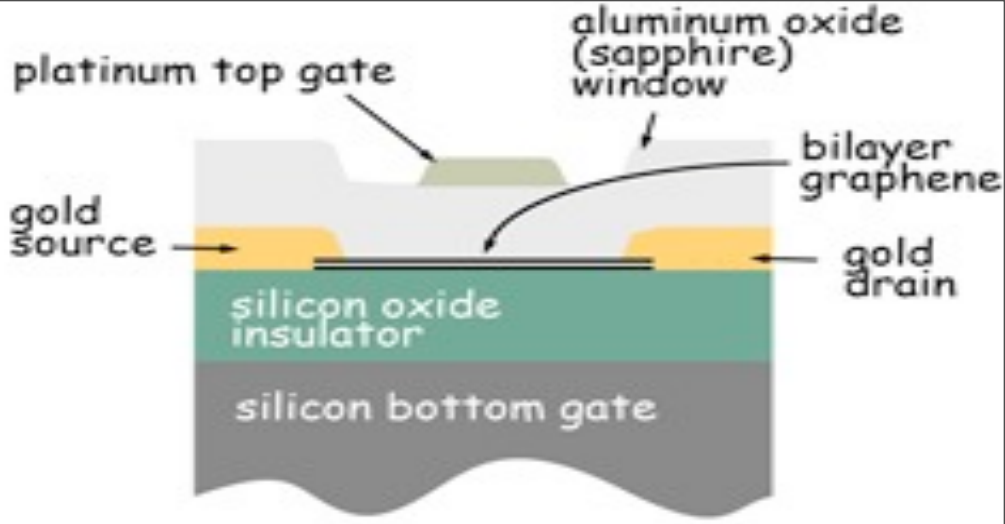

PUERTO VALLARTA

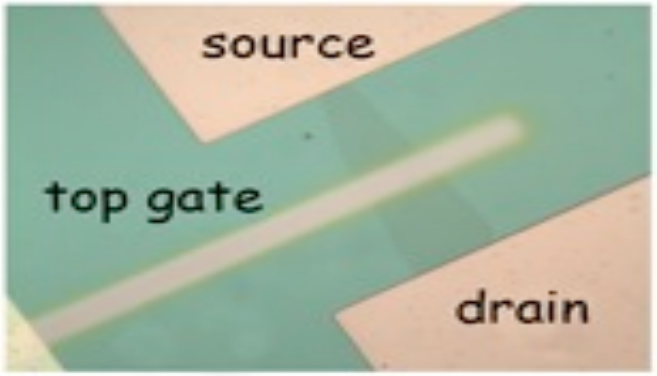

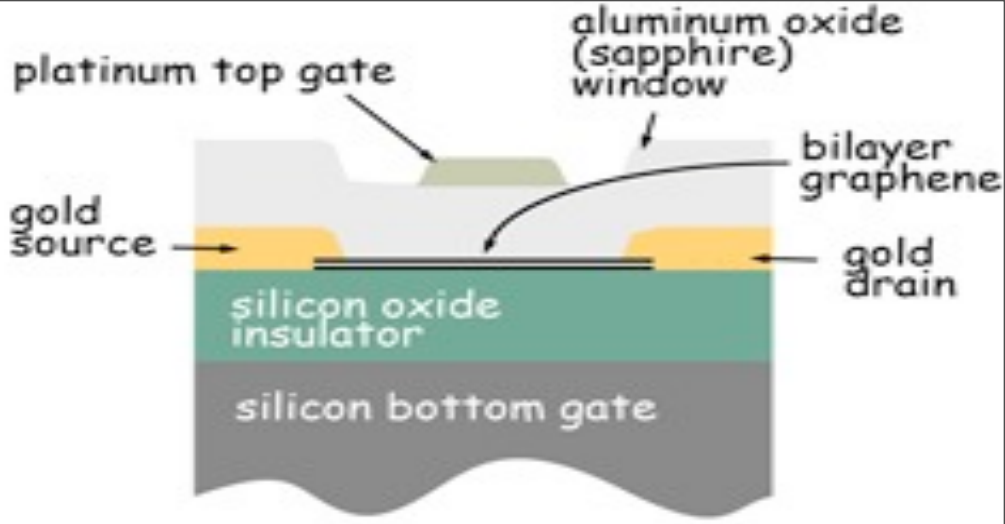

PUERTO VALLARTA

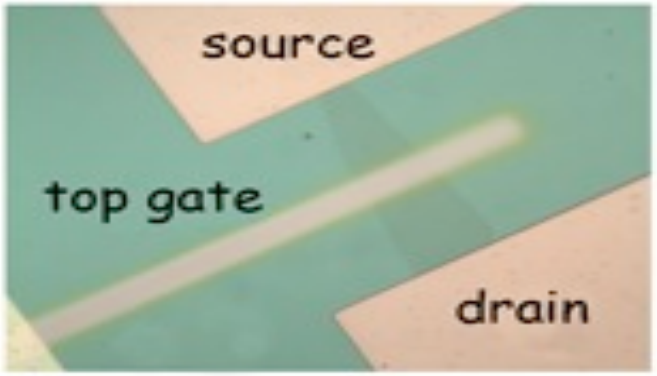

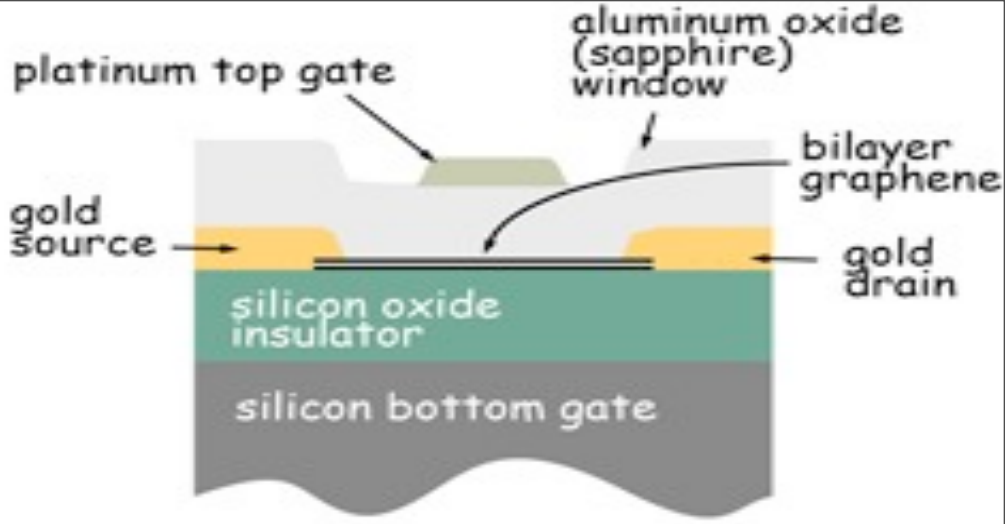

PUERTO VALLARTA

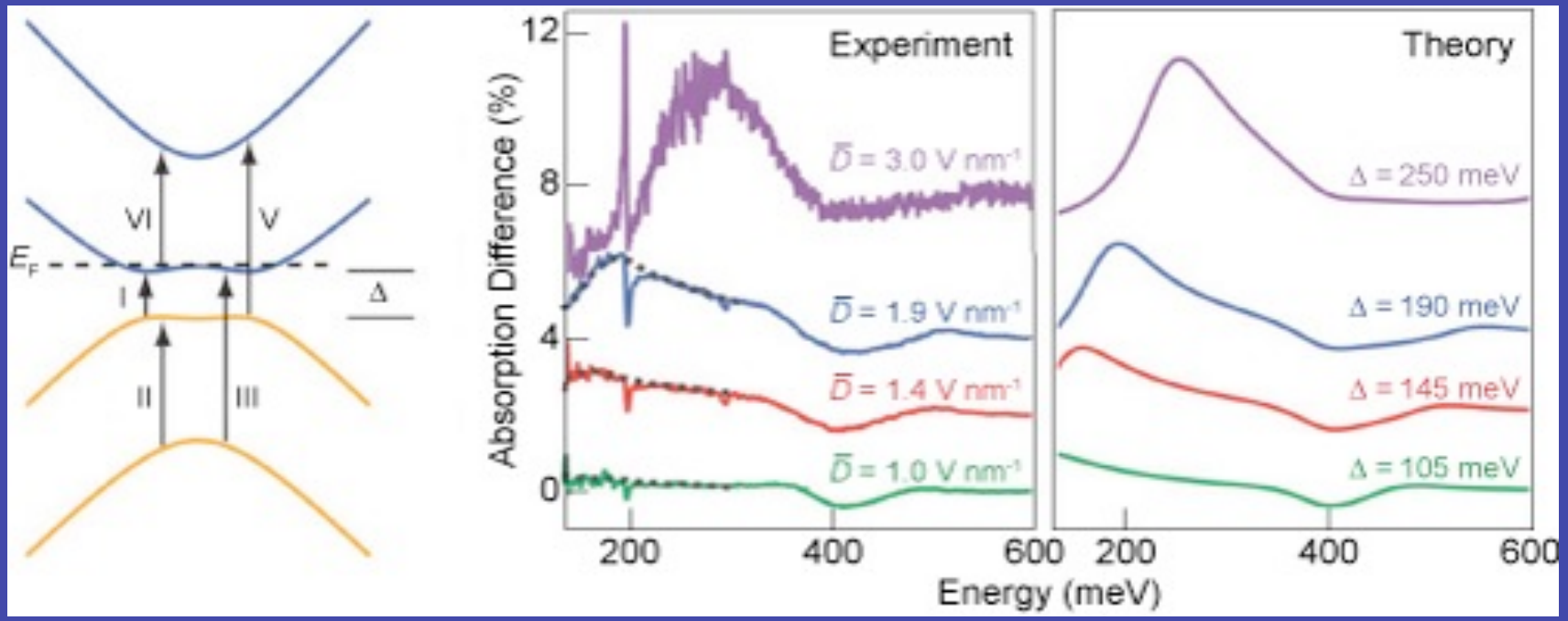

- Left: Allowed transitions between different sub-bands of a graphene bilayer.

- Center: Gate-induced absorption spectra for different applied displacement fields. Absorption peaks due to transition I are apparent (dashed black lines are guides to the eye). The sharp asymmetric resonance observed near 200 meV is due to phonon resonances with continuum electronic transitions. The broad feature around 400 meV is due to electronic transitions II, III, IV and V.

- Right: Theoretical prediction of the gate-induced absorption spectra. The fit provides an accurate determination of the gate-tunable bandgap.
- IN CONCLUSION, THE BANDGAP CAN BE PRECISELY CONTROLED FROM 0 to 250 meV

6. MATERIALS UNDER EXTREME TEMPERATURE AND PRESSURE

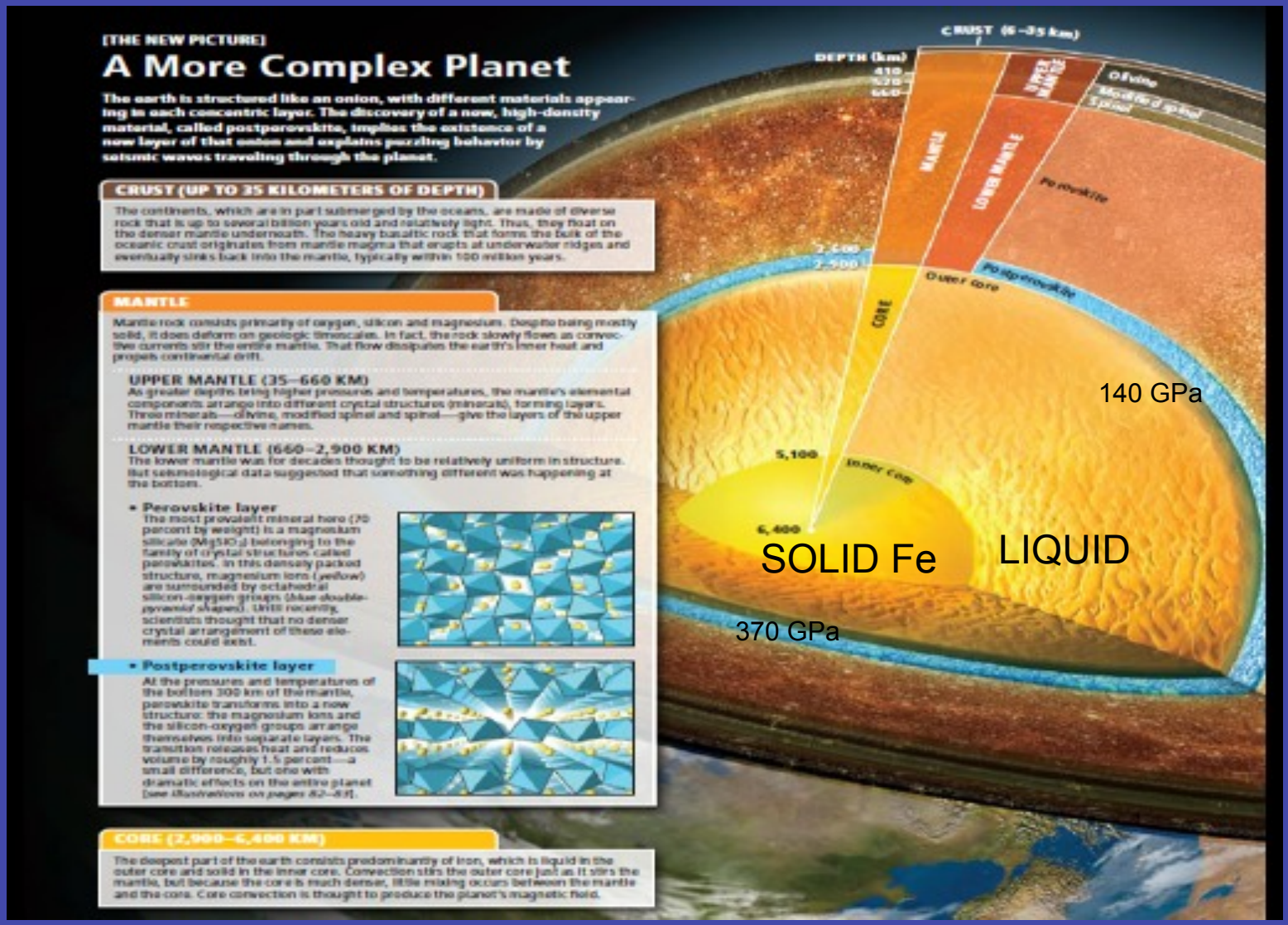

GEOPHYSICS AND MATERIALS: EXTREME CONDITIONS

- Crust 0–35 km <1 Gpa, 200–600
- Upper mantle 35–660 km 1–25 Gpa, 600–1600
- Lower mantle 660–2890km, 25–136 Gpa, 1600–4000
- Outer core 2890–5150 km, 136–330 Gpa, 4400–6100
- Inner core 5150–6360km, 330–360 Gpa, 6100K (±500K)

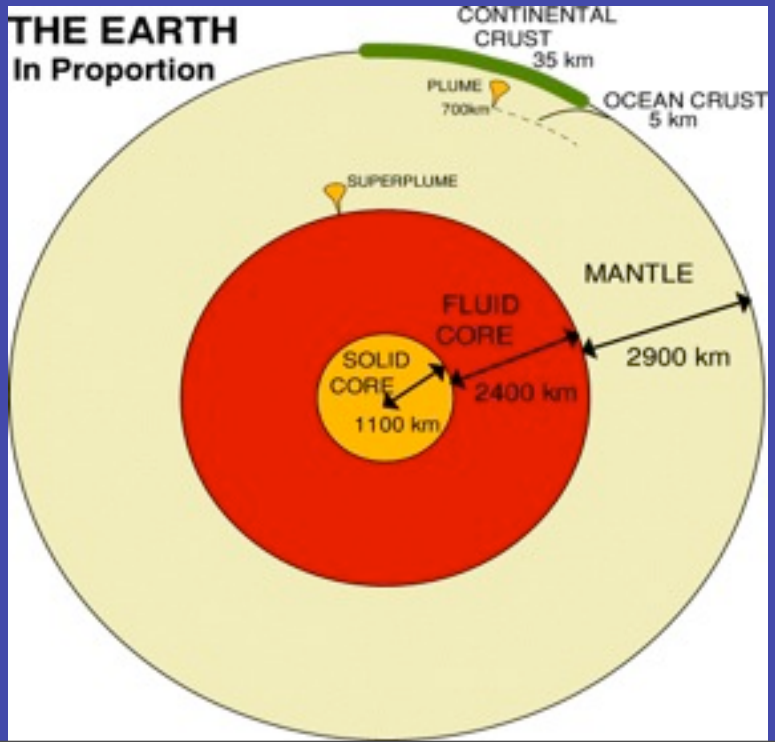

INTERFACE MANTLE-FLUID CORE
5200 K, 140 GPa

SOLID CORE: P= 360 GPa, T= 6000 K

HOW TO REPRODUCE THESE TEMPERATURES AND PRESSURES?
Diamond Anvill-Cell+Laser
X-Ray beam: few μm diameter

THE DEEP EARTH AT SYNCHROTRONS

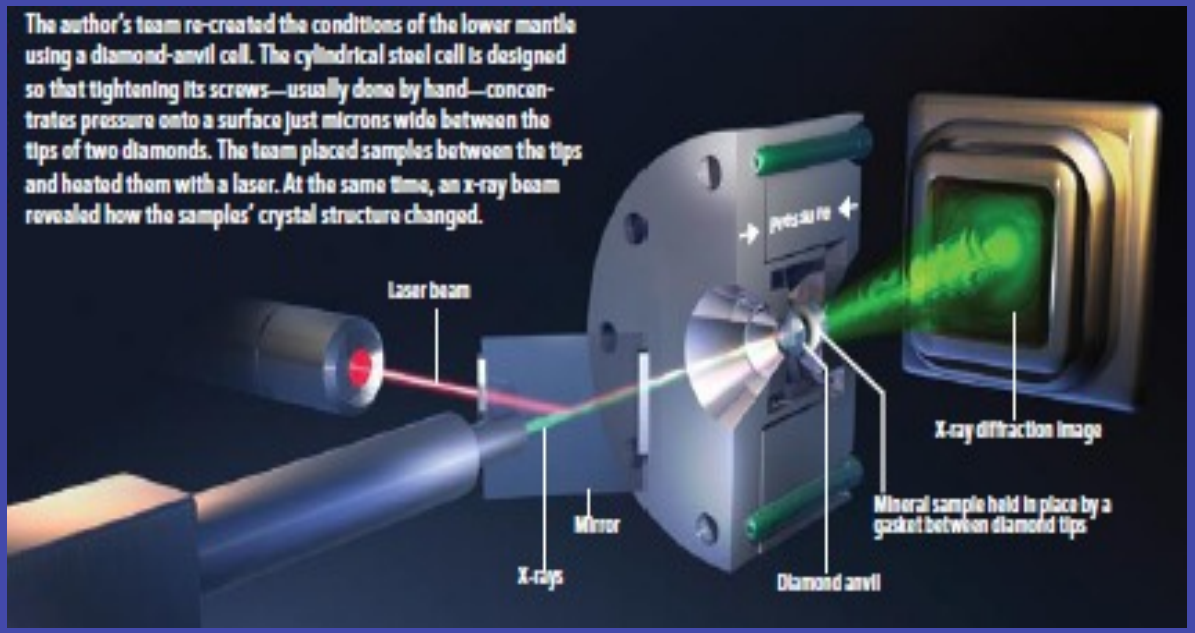

Beam size for the X-Ray: 1-2 μm
Beam size for the laser: 20 μm →to avoid T gradients

The Structure of Iron in Earth's Inner Core

Shigehiko Tateno, Kei Hirose,Yasuo Ohishi, Yoshiyuki Tatsumi SCIENCE 330, 359, 2010

Earth's solid inner core is mainly composed of iron (Fe). Because the relevant ultrahigh pressure and temperature conditions are difficult to produce experimentally, the preferred crystal structure of Fe at the inner core remains uncertain. Static compression experiments showed that the hexagonal close-packed (hcp) structure of Fe is stable up to 377 gigapascals and 5700 K(melting), corresponding to inner core conditions. The observed weak temperature dependence of the c/a axial ratio suggests that hcp Fe is elastically anisotropic at core temperatures. Preferred orientation of the hcp phase may explain previously observed inner core seismic anisotropy.

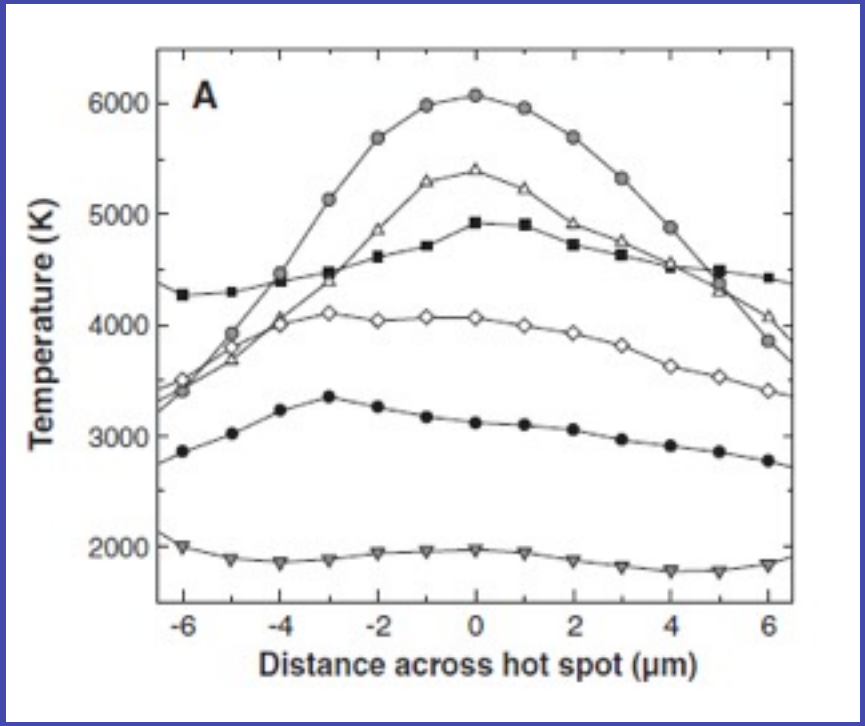

PUERTO VALLARTA

Representative XRD patterns of hcp Fe at :

(A) 332 GPa and 4820 K and (B) 356 GPa and 5520 K.

The peak positions of the bcc and fcc phases were calculated for volumes larger by 0 to 1% than that for the observed hcp phase.

hcp, hcp Fe; py, pyrite-type SiO_2 (pressure medium); C, Fe_3C

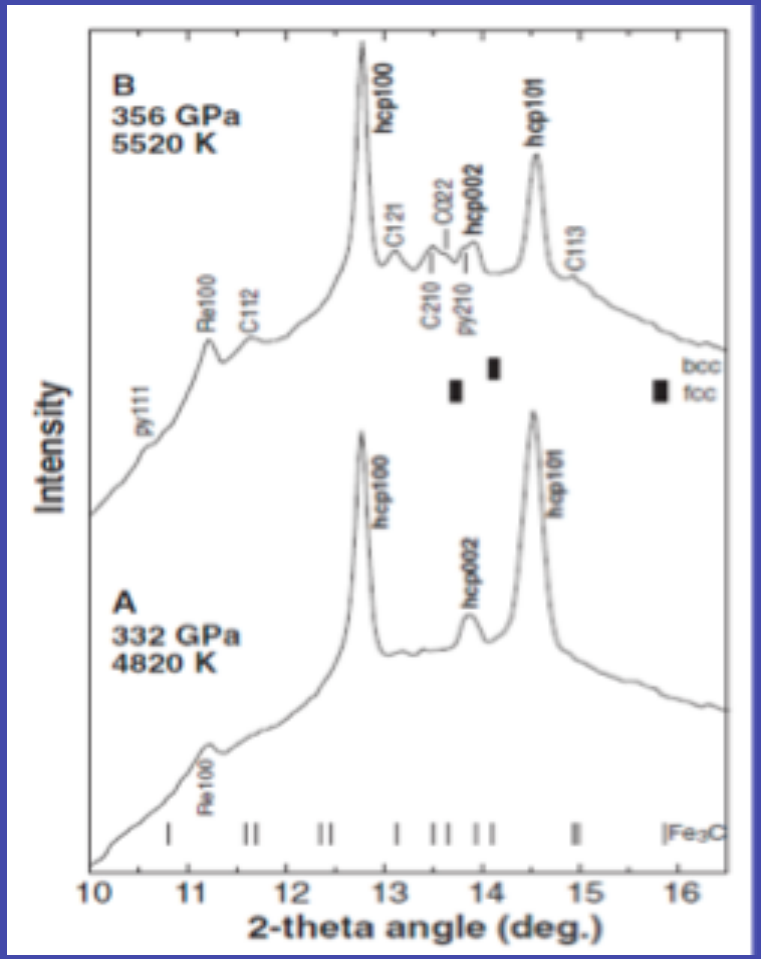

Phase diagram of Fe and the inferred temperature profile inside Earth.

Open symbols indicate the present results (different symbols indicate different runs), and solid diamonds indicate data from previous experimental work . The low-pressure solid-solid phase transition

boundaries and melting curve are from Boehler . Liq., liquid.

(Inset) Sample photograph at 335 GPa in the DAC.

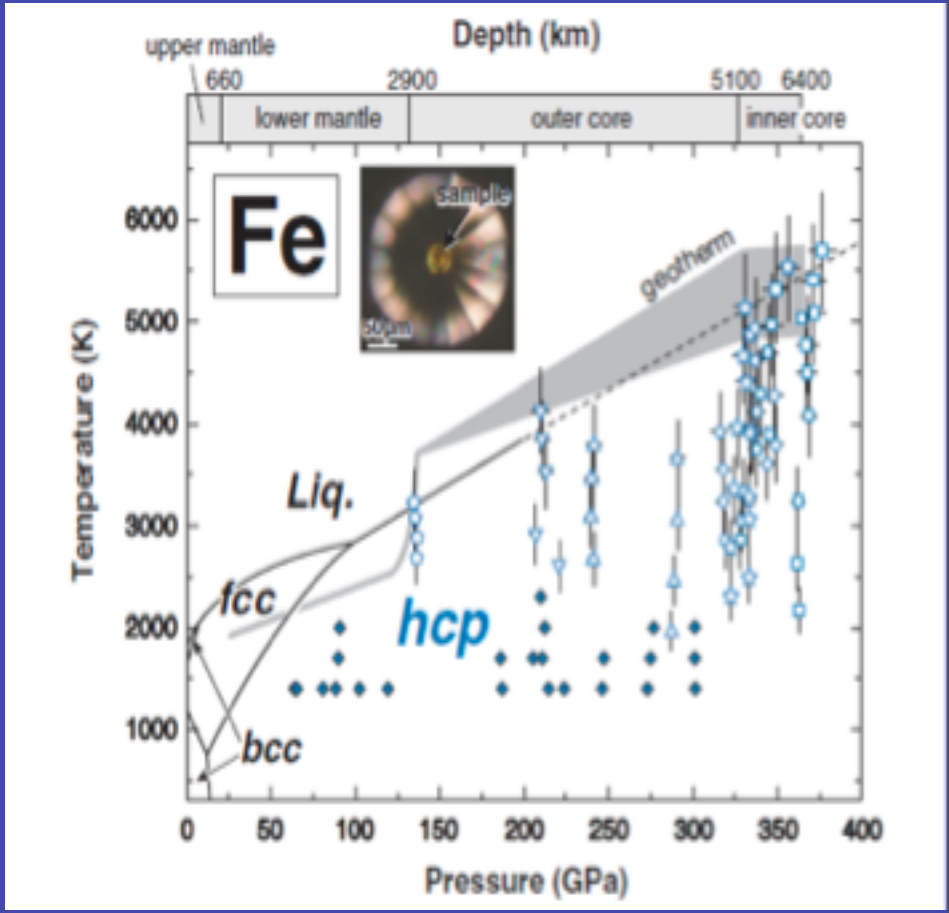

Peridotite at 5200 K and 140 GPa (SiO_2, 44.3 %; MgO, 41.6;FeO, 7.3; MnO, 0.1, TiO_2, 0.2; Al_2O_3, 2.4; CaO, 1.6; Cr_2O_3, 0.1)

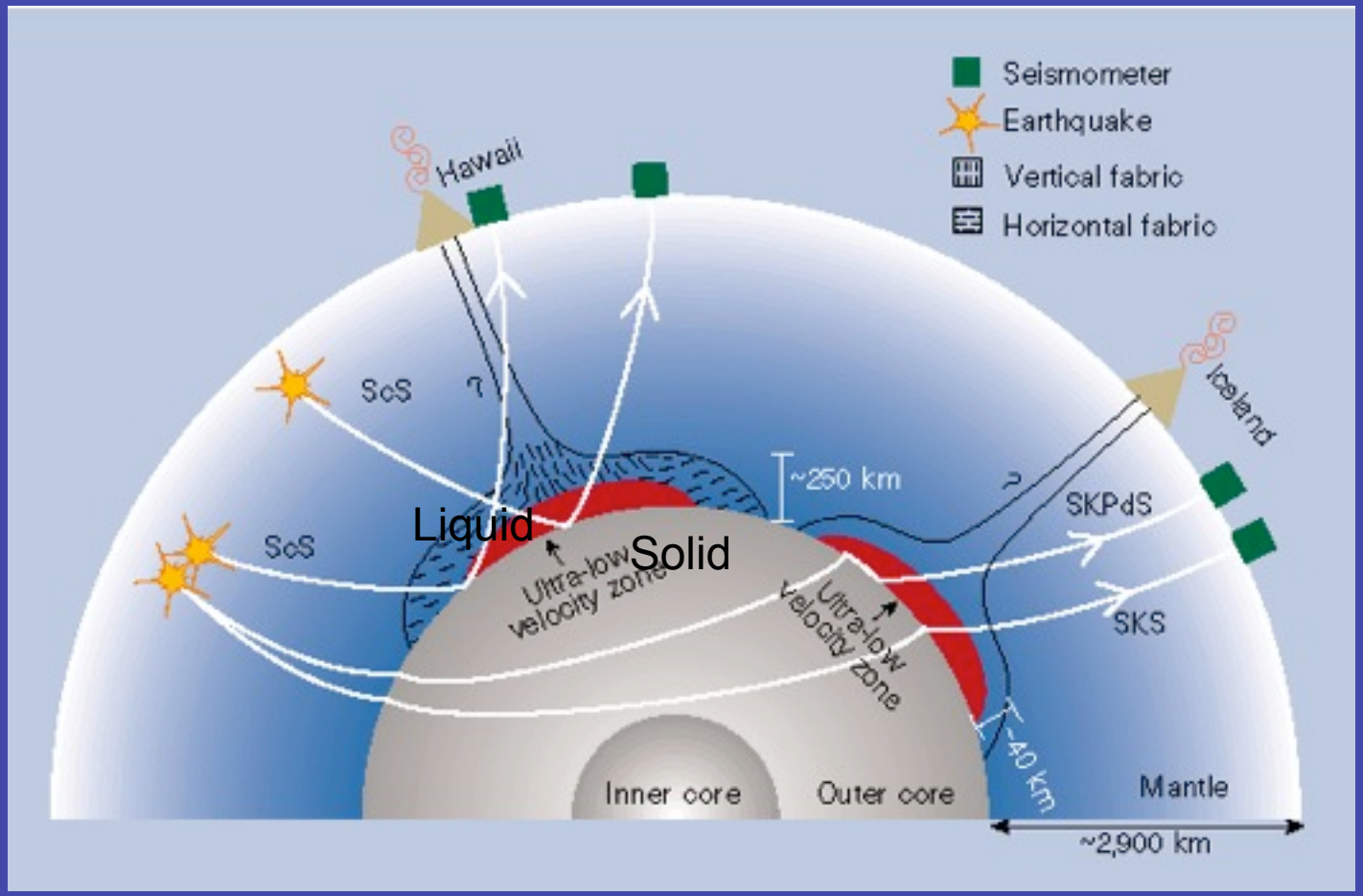

PUERTO VALLARTA

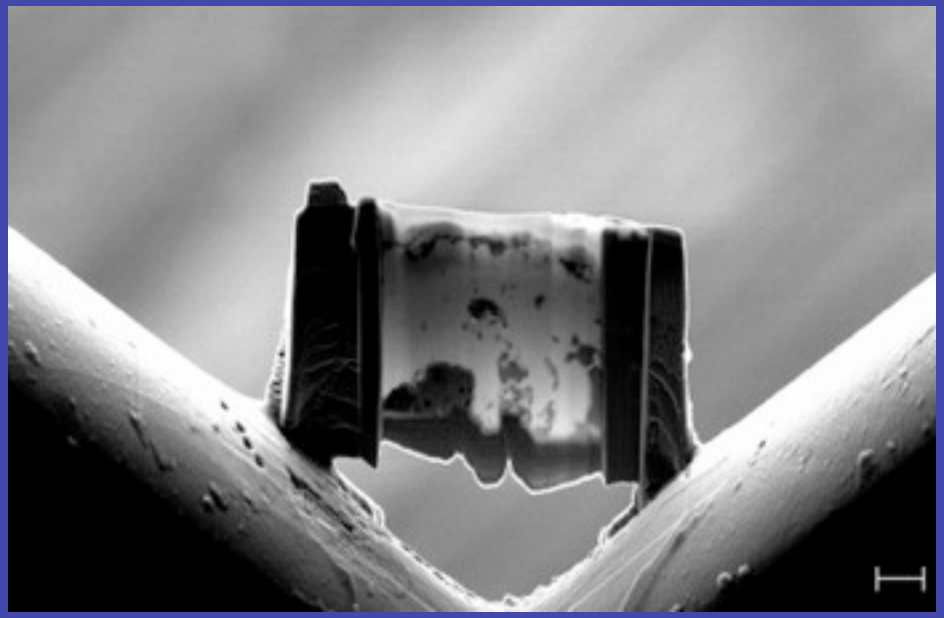

G. Fiquet, A. L. Auzende, J. Siebert, A. Corgne, H. Bureau, H. Ozawa, G. Garbarino SCIENCE 329, 1561, 2010

- Scanning electron microscopy image of a “mantle” sample after transformation, stuck on a copper grille and thinned down by a focused ion beam (FIB). It allows to detect the different synthesized minerals and liquids during these experiments: a matrix, consisting of a phase of a perovskite structure ($(Mg,Fe)SiO_3$), - the most abundant mineral in the Earth because it is the most stable in the inferior mantle), is shown in light grey. The veins and liquid pockets enriched in iron and calcium are visible (in dark grey). Scale of the horizontal bar is 2 μm. Credits: G.Fiquet.
- Hot spot: 20 μm, X-Ray beamsize: 1.7x2.3 μm at 33. 3 keV

At high temperature, pressures were measured from cell parameters of the magnesium perovskite $(Mg,Fe)SiO_3$ by using a thermal equation of state recently reported for the same KLB-1 peridotitic starting material as used in our study (18). We used in situ x-ray diffraction as primary criterion for melting) and to determine the order in which crystalline phases melt.

Diffraction patterns collected at 61 GPa after normalized reference background subtraction:subsolidus at 2715 K (bottom) and above solidus at 3750 K (top). The diffuse scattering liquid contribution is outlined by the shaded area as a guide; it does not correspond to a physical structural model of the liquid. HKL indexes are given for remaining diffraction peaks that can be assigned to magnesium silicate perovskite, observed above the solidus temperature at this pressure (top). Stars denote diffraction peaks of Ca-perovskite and ferropericlase

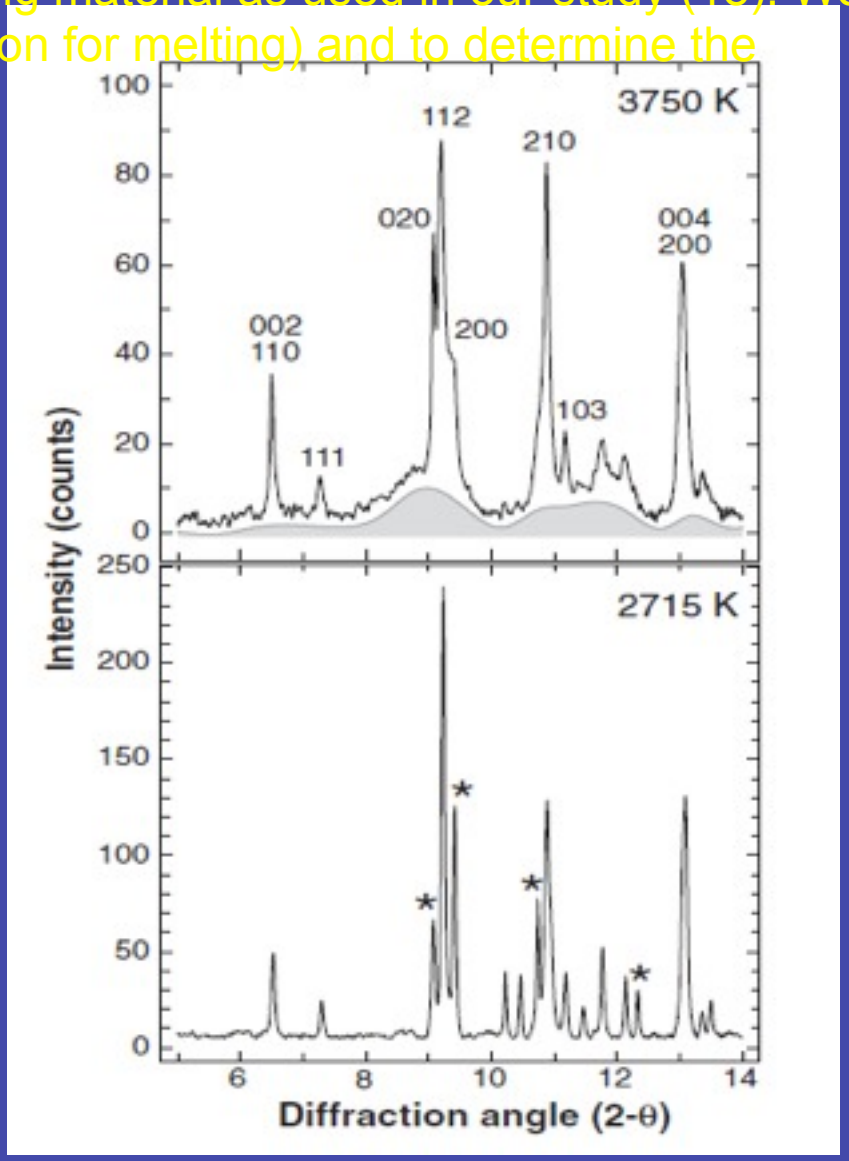

7. SUPERCOOLING

7. SUPERCOOLING

- Promoting freezing in a liquid is straightforward : you simply add suitable templates. The templates can be either ‘seeds’ of the crystalline phase that would form from the liquid, or small crystals of another material whose atomic-level surface structure in some way matches that of such seeds.

7. SUPERCOOLING

- Promoting freezing in a liquid is straightforward : you simply add suitable templates. The templates can be either ‘seeds’ of the crystalline phase that would form from the liquid, or small crystals of another material whose atomic-level surface structure in some way matches that of such seeds.

7. SUPERCOOLING

- Promoting freezing in a liquid is straightforward : you simply add suitable templates. The templates can be either ‘seeds’ of the crystalline phase that would form from the liquid, or small crystals of another material whose atomic-level surface structure in some way matches that of such seeds.

- What is more difficult to conceive of is a solid surface that inhibits freezing by acting as a template for the liquid.However, recently, Schulli, Daudin, Renaud, Vaysset, Geaymond & Pasturel [Nature 464, 1192, 2010] describe evidence suggesting that such a template is possible. Their results have wide implications not only for fundamental studies of freezing, but also for the practical control of this phase transition.

7. SUPERCOOLING

- Promoting freezing in a liquid is straightforward : you simply add suitable templates. The templates can be either ‘seeds’ of the crystalline phase that would form from the liquid, or small crystals of another material whose atomic-level surface structure in some way matches that of such seeds.

- What is more difficult to conceive of is a solid surface that inhibits freezing by acting as a template for the liquid.However, recently, Schulli, Daudin, Renaud, Vaysset, Geaymond & Pasturel [Nature 464, 1192, 2010] describe evidence suggesting that such a template is possible. Their results have wide implications not only for fundamental studies of freezing, but also for the practical control of this phase transition.

7. SUPERCOOLING

- Promoting freezing in a liquid is straightforward : you simply add suitable templates. The templates can be either ‘seeds’ of the crystalline phase that would form from the liquid, or small crystals of another material whose atomic-level surface structure in some way matches that of such seeds.

- What is more difficult to conceive of is a solid surface that inhibits freezing by acting as a template for the liquid.However, recently, Schulli, Daudin, Renaud, Vaysset, Geaymond & Pasturel [Nature 464, 1192, 2010] describe evidence suggesting that such a template is possible. Their results have wide implications not only for fundamental studies of freezing, but also for the practical control of this phase transition.

- When a liquid is cooled, there is a thermodynamically defined temperature - the freezing point, or liquidus temperature - at which it should start to crystallize. But the crystal nucleation that initiates freezing requires a driving force, and occurs only at temperatures below the ideal freezing temperature.

7. SUPERCOOLING

- Promoting freezing in a liquid is straightforward : you simply add suitable templates. The templates can be either ‘seeds’ of the crystalline phase that would form from the liquid, or small crystals of another material whose atomic-level surface structure in some way matches that of such seeds.

- What is more difficult to conceive of is a solid surface that inhibits freezing by acting as a template for the liquid.However, recently, Schulli, Daudin, Renaud, Vaysset, Geaymond & Pasturel [Nature 464, 1192, 2010] describe evidence suggesting that such a template is possible. Their results have wide implications not only for fundamental studies of freezing, but also for the practical control of this phase transition.

- When a liquid is cooled, there is a thermodynamically defined temperature - the freezing point, or liquidus temperature - at which it should start to crystallize. But the crystal nucleation that initiates freezing requires a driving force, and occurs only at temperatures below the ideal freezing temperature.

7. SUPERCOOLING

- Promoting freezing in a liquid is straightforward : you simply add suitable templates. The templates can be either ‘seeds’ of the crystalline phase that would form from the liquid, or small crystals of another material whose atomic-level surface structure in some way matches that of such seeds.

- What is more difficult to conceive of is a solid surface that inhibits freezing by acting as a template for the liquid.However, recently, Schulli, Daudin, Renaud, Vaysset, Geaymond & Pasturel [Nature 464, 1192, 2010] describe evidence suggesting that such a template is possible. Their results have wide implications not only for fundamental studies of freezing, but also for the practical control of this phase transition.

- When a liquid is cooled, there is a thermodynamically defined temperature - the freezing point, or liquidus temperature - at which it should start to crystallize. But the crystal nucleation that initiates freezing requires a driving force, and occurs only at temperatures below the ideal freezing temperature.

- The cooling of a liquid to below the ideal freezing temperature, known as supercooling is of great interest in diverse areas ranging from the control of microstructure in metallic welds and castings to the inhibition (or promotion) of ice formation necessary for the survival of living systems.

SUPERCOOLING

SUPERCOOLING

- For liquids in contact with solids, crystalline surfaces induce layering of the adjacent atoms in the liquid and may prevent or lower supercooling. This seed effect is supposed to depend on the local lateral order adopted in the last atomic layers of the liquid in contact with the crystal. Although it has been suggested that there might be a direct coupling between surface-induced lateral order and supercooling, no experimental observation of such lateral ordering at interfaces is available.

SUPERCOOLING

- For liquids in contact with solids, crystalline surfaces induce layering of the adjacent atoms in the liquid and may prevent or lower supercooling. This seed effect is supposed to depend on the local lateral order adopted in the last atomic layers of the liquid in contact with the crystal. Although it has been suggested that there might be a direct coupling between surface-induced lateral order and supercooling, no experimental observation of such lateral ordering at interfaces is available.

SUPERCOOLING

- For liquids in contact with solids, crystalline surfaces induce layering of the adjacent atoms in the liquid and may prevent or lower supercooling. This seed effect is supposed to depend on the local lateral order adopted in the last atomic layers of the liquid in contact with the crystal. Although it has been suggested that there might be a direct coupling between surface-induced lateral order and supercooling, no experimental observation of such lateral ordering at interfaces is available.

SUPERCOOLING

- For liquids in contact with solids, crystalline surfaces induce layering of the adjacent atoms in the liquid and may prevent or lower supercooling. This seed effect is supposed to depend on the local lateral order adopted in the last atomic layers of the liquid in contact with the crystal. Although it has been suggested that there might be a direct coupling between surface-induced lateral order and supercooling, no experimental observation of such lateral ordering at interfaces is available.

- In situ X-ray scattering and ab initio molecular dynamics reveal that pentagonal atomic arrangements of Au atoms at this interface [Si(111) 6x6] favour a lateral-ordering stabilization process of the liquid phase. This interface-enhanced stabilization of the liquid state shows the importance of the solid–liquid interaction for the structure of the adjacent liquid layers. Such processes are important for present and future technologies, as fluidity and crystallization play a key part in soldering and casting, as well as in processing and controlling chemical reactions for microfluidic

ADVANTAGES OF THE X-RAY

You can probe simultaneously:
- the bulk
- the surface layer (reconstruction)
- the liquid

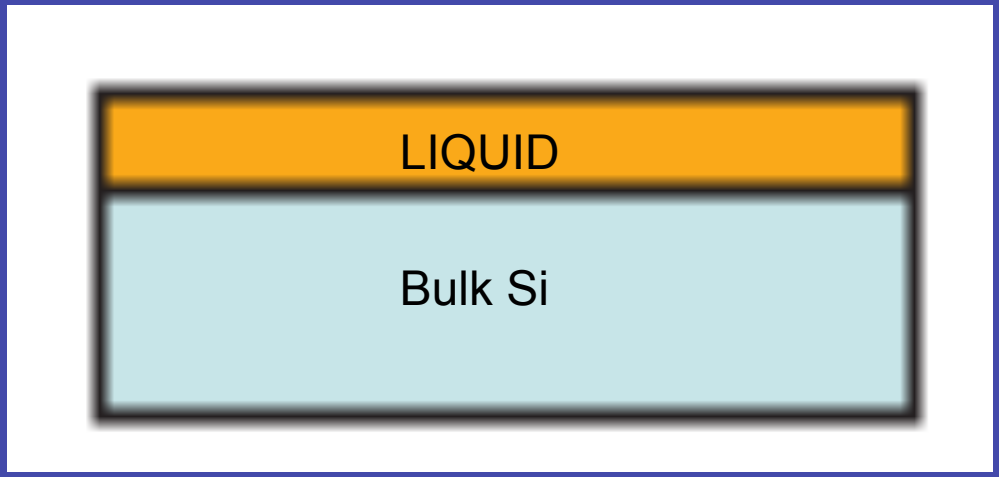

X-Ray

Surface layers

T. U. Schülli, R. Daudin, G. Renaud, A. Vaysset, O. Geaymond &A. Pastrurel Nature 464, 1174, 2010

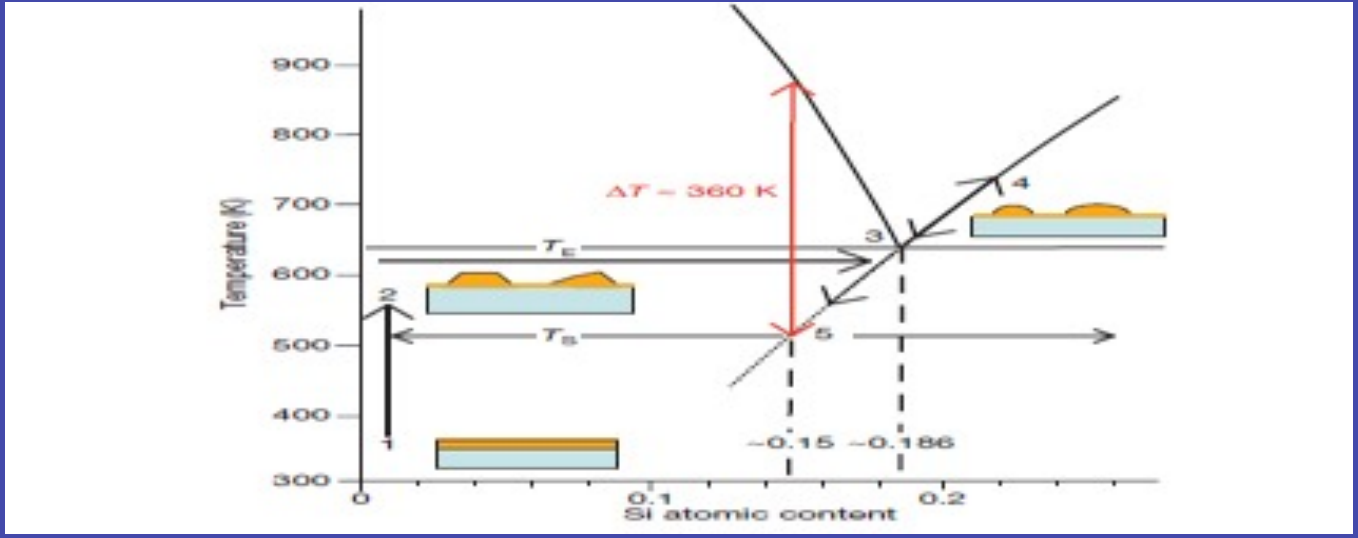

Step 1: Seven monolayers of Au are deposited at room temperature.

Step 2: On annealing they transform into crystalline Au islands.

Step 3: At T_E=636 K, melting sets in and AuSi droplets with the eutectic composition ($Au_{81.4}Si_{18.6}$) are formed.

Step 4: Heating up to 673K before cooling induces a (6x6) reconstruction, and leads to a preservation of the liquid phase down to 513K(step 5), where phase separation and solidification occur (step 5). Above T_E, on heating or cooling, the liquid composition is expected to follow the Si liquidus. Below T_E, it follows the (extrapolated; dotted line) metastable Si liquidus. The degree of supercooling (red arrow) has to be measured between this latter and the Au liquidus above T_E for the corresponding composition of ~15 at.% Si. It amounts to ~ 3 60 K because as the liquid alloy droplets cool, Si comes out of solution and redeposits on the substrate. The observed freezing point of 513 K represents a supercooling of 360 K below the liquidus of the resulting composition.

Figure 2 | Reciprocal space mapping of liquid AuSi islands on (6x6) reconstructed Si(111).

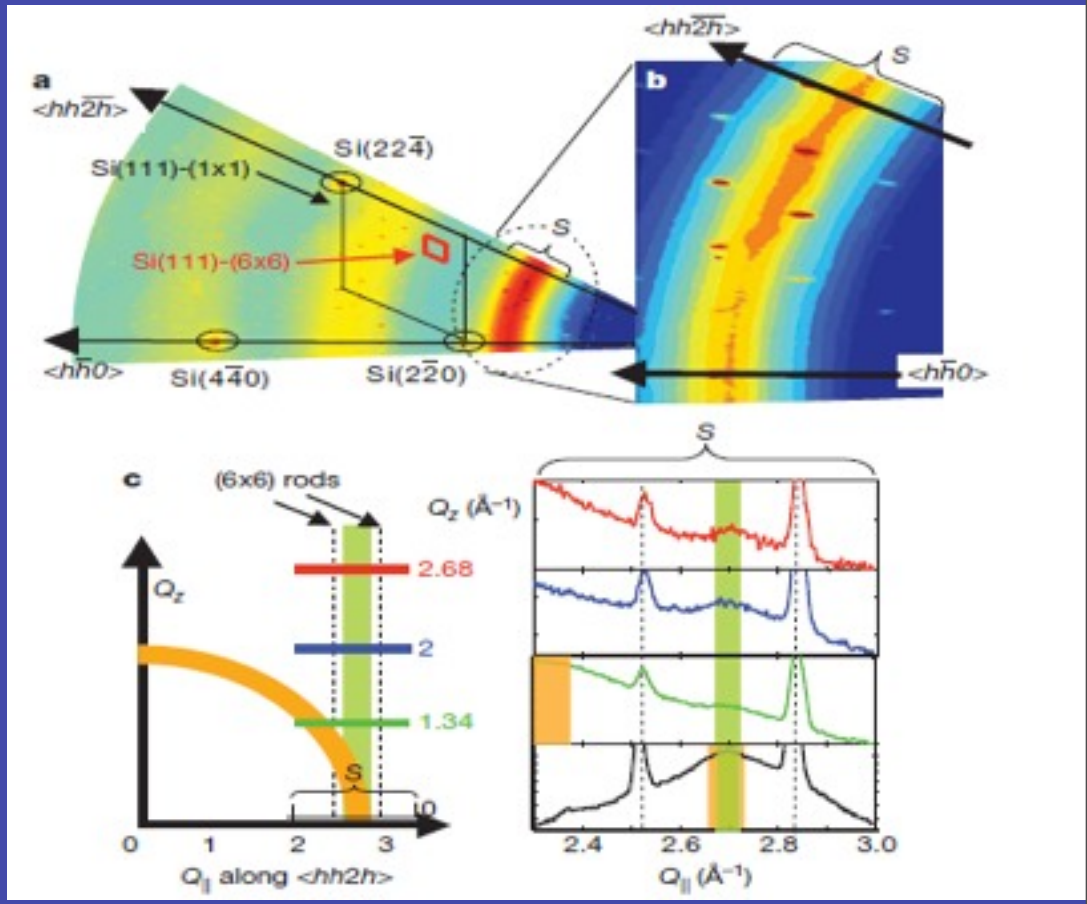

a, Reciprocal space map of the liquid in its supercooled state on a (6x6) reconstructed Si(111) surface. Blue colour corresponds to low intensity, and red to high intensity, yellow being intermediate. Three bulk Bragg peaks are visible, together with a mesh of smaller peaks arising from the (6x6) surface/interface periodic superstructure. The three diffuse rings correspond to liquid-like scattering.

b, Anisotropy of the first order maximum of the liquid structure factor: In the vicinity of strong (6x6) reconstruction peaks the signal from the liquid is enhanced, underlining morphological similarities between the crystalline surface and the adjacent liquid layers.

c, Right: scans across the first ordermaximum of the liquid structure factor in the plane (along section S marked in **a** and **b**) and parallel to it for several values of out-of-plane momentum transfer, Q_z. Left: the sketch indicates in orange the position of the first maximum of the isotropic liquid. The green rod corresponds to the intensity distribution stemming from preferential in-plane order.

Figure 3 | Evolution of the liquid structure factor during cooling and solidification.

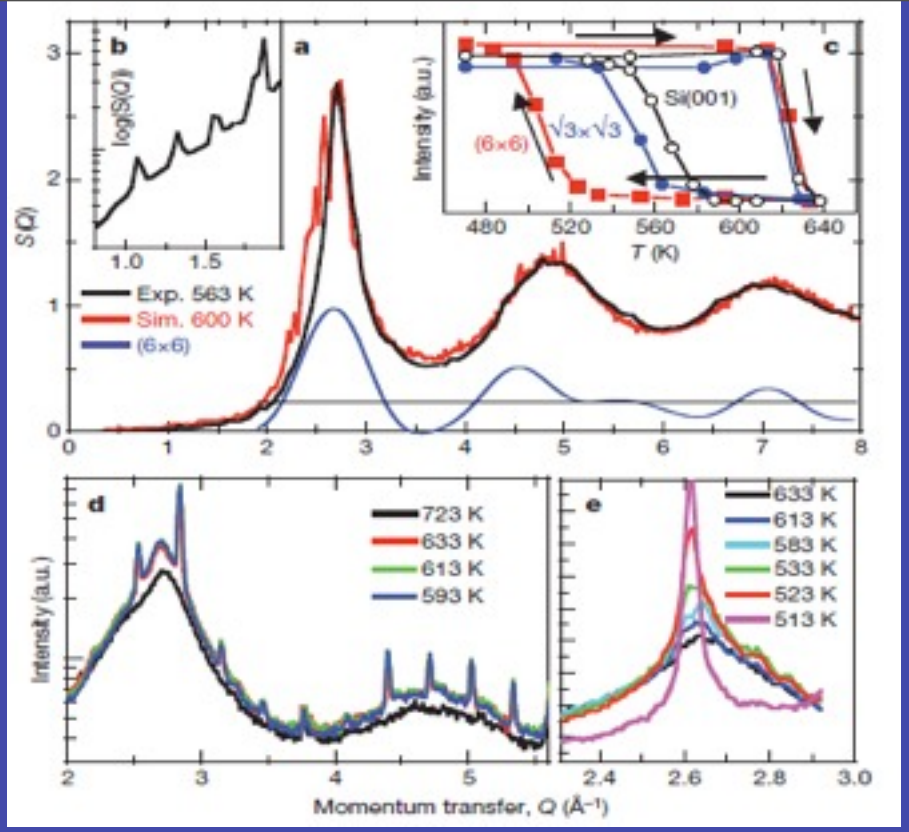

.

a, Angular average of the experimental structure factor S(Q) of liquid AuSi at 563K (black line) together with the theoretical structure factor extracted from MDS at 600K(red line). The blue line corresponds to the mean structure factor of the (6x6) reconstruction.

b, Zoom (logarithmic scale) on the low-Q spectrum of the structure factor, showing the Bragg peaks from two-dimensional crystallites floating on the surface of liquid AuSi.

c, Hysteresis loops of the integrated intensity of the Au(220) Bragg peak during the solid–liquid–solid transition of Au islands on Si(001) (black open circles), on an Si(111)-(√3x√3)R 30° reconstruction (blue filled circles) and on an Si(111)-(6x6) reconstruction (red squares).

d, Liquid structure factor (logarithmic scale) along the <110>. crystallographic direction of the Si(111) surface. The strong influence of the appearance of the (6x6) reconstruction on the structure of the liquid is visible.

e, Evolution of the first maximum of the liquid structure factor in the supercooling regime

Figure 4 | Au-induced Si(111)-(6x6) surface leading to enhanced supercooling. Unit cell (black lozenge) of the complex (6x6) reconstruction (only the Au atoms are shown) formed at T<673K after annealing temperatures T>673 K. A pentagonal cluster (see inset three-dimensional structure) present in the simulated liquid has similar topology and bond length (2.84 Å) as the surface structure (2.86 Å) smaller than in the Au f.c.c. lattice (2.90 Å). Out of 45 atoms in the unit cell, 30 are in a pentagonal environment (interconnected by blue lines).

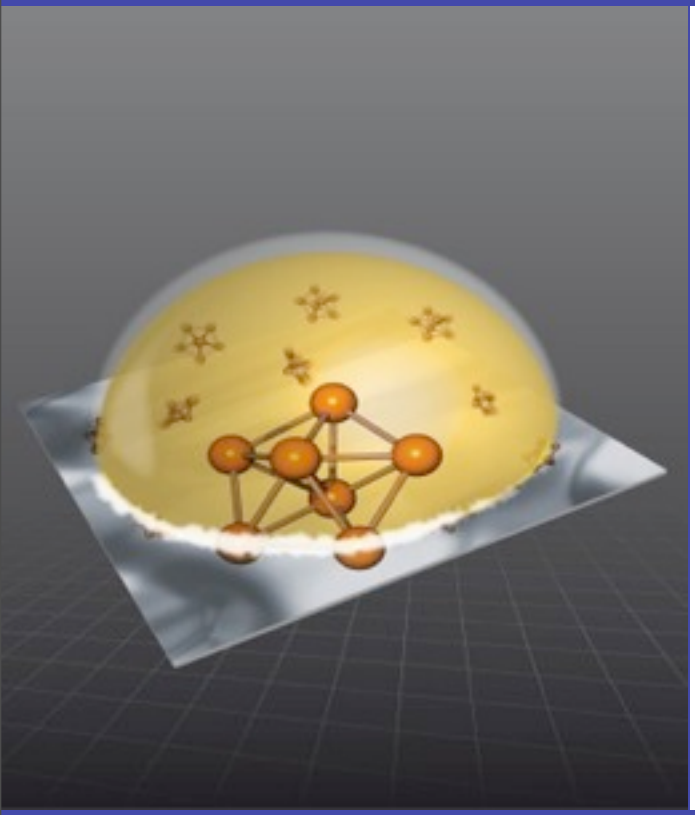

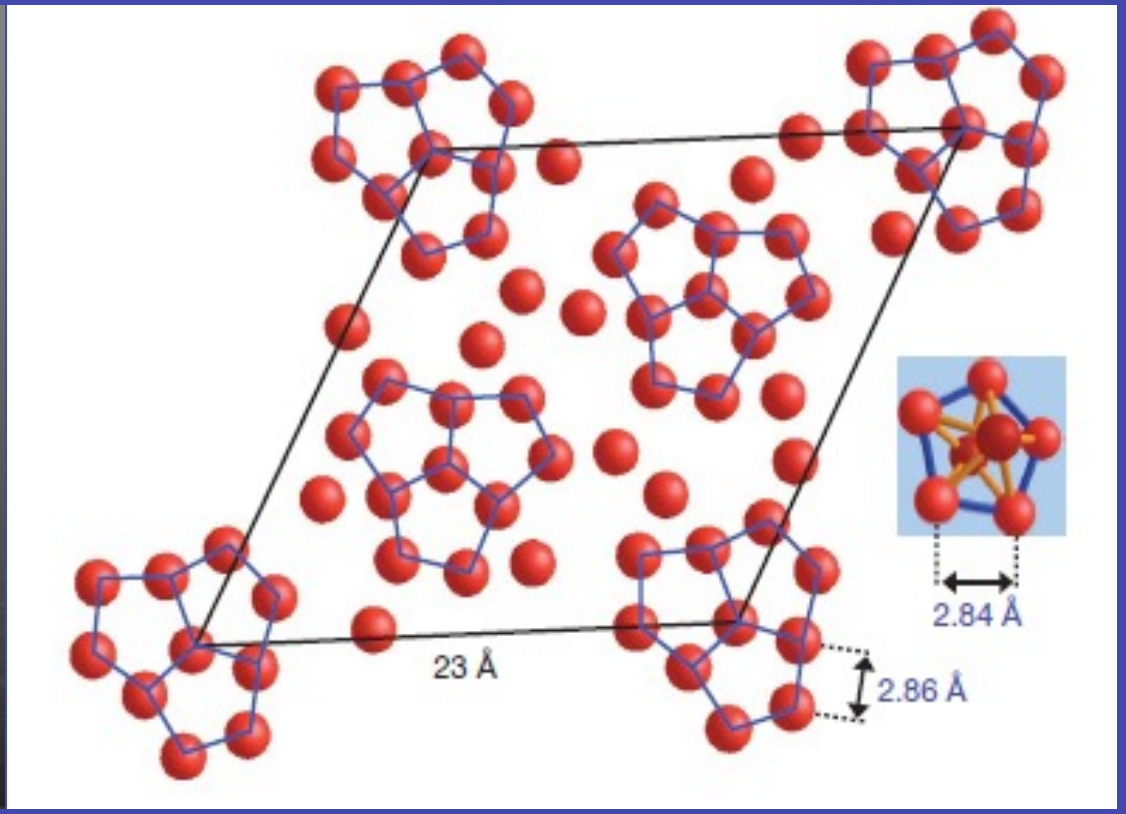

However, when the alloy droplets freeze on the 6 × 6 silicon surface, the resulting gold crystals form in random orientations. This suggests that the substrate has no orienting role in freezing; the actual site and mechanism of crystal nucleation remain undetermined.

8. Conclusions

- There are already beamlines with beam size of 100x100nm
- 30x30 are in preparation but this needs new technology, with AFM on the BL, otherwise you will never align the sample and the beam. I addition thermal noise, electrical noise, vibrations have to be tackled.

ESPCA

ESCOLA SÃO PAULO DE CIÊNCIA AVANÇADA

LNLS

THE NEW DEVELOPMENTS IN THE FIELD OF SYNCHROTRON RADIATION

The State of São Paulo would like to increase the number of foreign pos-docs. For that, it is creating "Advanced schools" on different topics. The goal is to have 100 students, during their PhD: 50% from Latin America and 50% from other parts of the world. The school will not deal with the techniques, but with the scientific domains: structural biology, 3D imaging, magnetism, nanosciences, catalysis, etc.

DATES
From January 17th till 25th 2011, followed by 2 days visiting universities in Sao Carlos, Campinas and Sao Paulo.

SUBMISSION OF APPLICATIONS
Application period from July 01st till October 15th, 2010. The acceptance of the school will be notified by e-mail on October 18th, 2010.

LOCATION
Brazilian Synchrotron Light Laboratory (LNLS)
Rua Giuseppe Máximo Scolfaro, 10.000 - Pólo II de Alta Tecnologia
Campinas - SP - Brazil

STRUCTURAL BIOLOGY
Ada Yonath (Weizmann Institute of Science, Israel)
J.A. Marquez (EMBL, Grenoble, France)
José Nelson Onuchic (USCD, USA)
Frederic Leroy (L'Oréal, Paris)
Igor Polikarpov (USP, São Paulo, Brazil)

3D X-RAY IMAGING
Franz Pfeiffer (T.U. Munich)
Paul Tafforeau (ESRF, Grenoble)
Wolgang Ludwig (CNRS, Lyon)
Jin Wang (APS, USA)

CATALYSIS
M. Salmeron (UC, Berkeley, USA)
Gemma Guilera (ALBA, Barcelona)
Daniela Zanchet (LNLS, Brazil)

MAGNETISM AND SUPERCONDUCTIVITY
Albert Fert (Orsay, France)
Sebastian Stepanow (Max Planck Institut, Germany)
S.V. Borisenko (IFW, Dresden, Germany)
S. Louie (UC, Berkeley, USA)

NANOSCIENCES
S. Louie (UC, Berkeley, USA)
D. Ugarte (Unicamp, Campinas, Brazil)
R. Paniago (UFMG, Minas Gerais, Brazil)
Galo Soler Illia (CNEA, Argentina)

ENVIRONMENT
P. Eduardo Artaxo Netto (IFUSP, São Paulo, Brazil)

ORGANIZATION
Lodging, transportation and air tickets will be covered and organized by the School

VISIT THE WEBSITE:
ESPCA.LNLS.BR

FAPESP LNLS CNPEM

11/29/10

PUERTO VALLARTA